MATERIALS FOR ADAPTIVE STRUCTURAL ACOUSTIC CONTROL

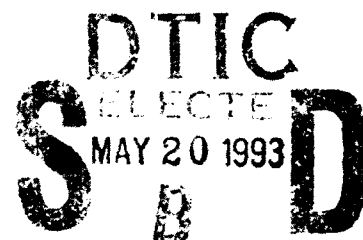Period February 1, 1992 to January 31, 1993

Annual Report

VOLUME III

OFFICE OF NAVAL RESEARCH
Contract No. N00014-92-J-1510

APPROVED FOR PUBLIC RELEASE – DISTRIBUTION UNLIMITED

Reproduction in whole or in part is permitted for any purpose
of the United States Government

L. Eric Cross

93-11220

PENNSTATE

1855

THE MATERIALS RESEARCH LABORATORY
UNIVERSITY PARK, PA

93 5 19 033

REPORT DOCUMENTATION PAGE

Form Approved
OMB No 0704-0188

1. AGENCY USE ONLY (Leave blank)	2. REPORT DATE 04/06/93	3. REPORT TYPE AND DATES COVERED ANNUAL REPORT 02/01/92 TO 01/31/93

4. TITLE AND SUBTITLE

MATERIALS FOR ADAPTIVE STRUCTURAL ACOUSTIC CONTROL

5. FUNDING NUMBERS

6. AUTHOR(S)

L. ERIC CROSS

7. PERFORMING ORGANIZATION NAME(S) AND ADDRESS(ES)

MATERIALS RESEARCH LABORATORY
THE PENNSYLVANIA STATE UNIVERSITY
UNIVERSITY PARK, PA 16802

8. PERFORMING ORGANIZATION REPORT NUMBER

N00014-92-J-1510

9. SPONSORING/MONITORING AGENCY NAME(S) AND ADDRESS(ES)

OFFICE OF NAVAL RESEARCH   DOUGLAS E. HEATON
CODE 1513:NRJ   DEPT. NAVY/ONR, RES. REP.
800 NORTH QUINCY STREET   THE OHIO STATE UNIV. RES. CTR.
ARLINGTON, VA 22217   1960 KENNY ROAD
                             COLUMBUS, OH 43210-1063

10. SPONSORING/MONITORING AGENCY REPORT NUMBER

11. SUPPLEMENTARY NOTES

12a. DISTRIBUTION/AVAILABILITY STATEMENT

12b. DISTRIBUTION CODE

13. ABSTRACT (Maximum 200 words)

SEE FOLLOWING PAGE

14. SUBJECT TERMS

15. NUMBER OF PAGES

16. PRICE CODE

17. SECURITY CLASSIFICATION OF REPORT	18. SECURITY CLASSIFICATION OF THIS PAGE	19. SECURITY CLASSIFICATION OF ABSTRACT	20. LIMITATION OF ABSTRACT

ABSTRACT

This report documents work carried out in the Materials Research Laboratory of the Pennsylvania State University over the first year of a new ONR sponsored University Research Initiative (URI) entitled "Materials for Adaptive Structural Acoustic Control." For this report the activities have been grouped under the following topic headings:

1. General Summary Papers.
2. Materials Studies.
3. Composite Sensors.
4. Actuator Studies.
5. Integration Issues
6. Processing Studies.
7. Thin Film Ferroelectrics.

In material studies important advances have been made in the understanding of the evaluation of relaxor behavior in the PLZT's and of the order disorder behavior in lead scandium tantalate:lead titanate solid solutions and of the Morphotropic Phase Boundary in this system. For both composite sensors and actuators we have continued to explore and exploit the remarkable versatility of the flextensional moonie type structure. Finite element (FEA) calculations have given a clear picture of the lower order resonant modes and permitted the evaluation of various end cap metals, cap geometries and load conditions. In actuator studies multilayer structures have been combined with flextensional moonie endcaps to yield high displacement (50 μ meter) compact structures. Electrically controlled shape memory has been demonstrated in lead zirconate stannate titanate compositions, and used for controlling a simple latching relay. Detailed study of fatigue in polarization switching compositions has highlighted the important roles of electrodes, grain size, pore structures and microcracking and demonstrated approaches to controlling these problems. For practical multilayer actuators a useful lifetime prediction can be made from acoustic emission analysis.

New modelling of 2:2 and 1:3 type piezoceramic:polymer composites has given more exact solutions for the stress distribution and good agreement with ultradilatometer measurements of local deformations. Composites with 1:3 connectivity using thin wall ceramic tubes appear to offer excellent hydrostatic sensitivity, unusual versatility for property control and the possiblity to use field biased electrostrictors in high sensitivity configurations. Processing approaches have continued to use reactive calcining and have supplied the group with the wide range of ceramics used in these studies. For lead magnesium niobate:lead

ABSTRACT *(continued)*

titanate solid solutions grain size effects in samples of commerical purity have been traced to a thin (~20 n meter) glassy layer at the grain boundary. In parallel with the ONR URI the laboratory has extensive DARPA and Industry sponsored research on ferroelectric thin films, a very short selection of most relevant papers has been included for the convenience of users.

MATERIALS FOR ADAPTIVE STRUCTURAL ACOUSTIC CONTROL

Period February 1, 1992 to January 31, 1993

Annual Report

VOLUME III

OFFICE OF NAVAL RESEARCH
Contract No. N00014-92-J-1510

APPROVED FOR PUBLIC RELEASE – DISTRIBUTION UNLIMITED

Reproduction in whole or in part is permitted for any purpose
of the United States Government

L. Eric Cross

PENNSTATE

THE MATERIALS RESEARCH LABORATORY
UNIVERSITY PARK, PA

TABLE OF CONTENTS

APPENDICES

General Summary of Papers

1. R. E. Newnham, "Memories of Arthur Von Hippel," Ferroelectrics 137, 17 (1992).

2. C. Rosen, B. V. Hiremath and R. E. Newnham, "Piezoelectricity," American Inst. of Physics, New York (1991).

3. R. E. Newnham, "Ferroelectric Sensors and Actuators Smart Electroceramics," Ferroelectric Ceramics, Editor N. Setter, Proc. of Summer School on Ferroelectrics, Ascona (1991).

4. R. E. Newnham, "Smart Electroceramics in the 1990's and Beyond," J. European Ceramic Soc. (1992).

5. V. Sundar and R. E. Newnham, "Electrostriction and Polarization," Ferroelectrics 135, 431 (1992).

Materials Studies

6. J. R. Giniewicz, A. S. Bhalla and L. E. Cross, "Identification of the Morphotropic Phase Boundary in Lead Scandium Tantalate-Lead Titanate Solid Solution System."

7. J. R. Giniewicz, A. S. Bhalla and L. E. Cross, "Variable Structure Orde ing in Lead Scandium Tantalate-Lead Titanate Materials."

8. J. R. Giniewicz, A. S. Bhalla and L. E. Cross, "Lead Scandium Tantalate:Lead Titanate Materials for Field Stabilized Pyroelectric Device Applications," Ferroelectrics Letters 14, 21 (1992).

9. A. S. Bhalla, R. Guo, L. E. Cross, G. Burns, F. H. Dacol and R. R. Neurgaonkar, "Glassy Polarization in the Ferroelectric Tungsten Bronze (BaSr) Nb_2O_6," J. Appl. Phys. 71 (11), 5591 (1992).

10. J. S. Yoon, V. S. Srikanth and A. S. Bhalla, "The Electrical Properties of Antiferroelectric Lead Zirconate-Ferroelectric Lead Zinc Niobate Ceramics with Lanthanum," Proc. ISAF 1992, Greenville, South Carolina, pp. 556.

11. E. F. Alberta, D. J. Taylor, A. S. Bhalla and T. Takenaka, "The DC Field Dependence of the Piezoelectric, Elastic and Dielectric Constants for a Lead Zirconate Based Ceramic," Proc. ISAF 1992, Greenville, South Carolina, pp. 560.

12. W. Cao and L. Eric Cross, "The Ratio of Rhombohedral and Tetragonal Phases at the Morphotropic Phase Boundary in Lead Zirconate Titanate," Japan Journal of Applied Physics 31 (Pt. 1, No. 5A), 1399 (1992).

13. C. A. Randall, M. G. Matsko, W. Cao and A. S. Bhalla, "A Transmission Electron Microscope Investigation of the R3m - R3c Phase Transition in Pb(ZrTi)O_3 Ceramics," Solid State Comm. 85 (3), 193 (1993).

14. Shaoping Li, Chi Yeun Huang, A. S. Bhalla and L. E. Cross, "90° Domain Reversal in Pb(Zr_xTi_{1-x})O_3 Ceramics," Proc. ISAF 1992, Greenville, South Carolina.

15. Shaoping Li, Jyh Sheen, Q. M. Zhang, Sei-Joo Jang, A. S. Bhalla and L. E. Cross, "Quasi Lumped Parameter Method for Microwave Measurements of Dielectric Dispersion in Ferroelectric Ceramics," Proc. ISAF 1992, Greenville, South Carolina.

16. H. Wang, Q. M. Zhang, L. E. Cross and A. O. Sykes, "Piezoelectric Dielectric and Elastic Properties of Poly (Vinylidene Fluoride/Trifluorethylene)."

17. H. Wang, Q. M. Zhang, L. E. Cross and A. O. Sykes, "Clamping Effect on Piezoelectric Properties of Poly (Vinylidene Fluoride/Trifluoroethylene) Copolymers."

Composite Sensors

18. Ki-Young Oh, Yutaka Saito, Atsushi Furuta and Kenji Uchino, "Piezoelectricity in the Field Induced Ferroelectric Phase of Lead Zirconate Based Antiferroelectrics," J. Amer. Ceram. Soc. 75 (4), 795 (1992).

Composite Sensors *(continued)*

19. R. E. Newnham, Q. C. Xu, K. Onitsuka and S. Yoshikawa, "A New Type of Flextensional Transducer," Proc. 3rd Int. Mtg. on Transducers for Sonics and Ultrasonics (May 1992).

20. C. A. Randall, D. V. Miller, J. H. Adair and A. S. Bhalla, "Processing of Electroceramic-Polymer Composites Using the Electrorheological Effect," J. Mat. Res. 8 (4), 1 (1993).

21. C. A. Randall, S. Miyazaki, K. L. More, A. S. Bhalla and R. E. Newnham, "Structural-Property Relations in Dielectrophoretically Assembled $BaTiO_3$ Nanocomposites," Materials Letters 15, 26 (1992).

22. C. A. Randall, S. F. Wang, D. Laubscher, J. P. Dougherty and W. Huebner, "Structure Property Relations in Core-Shell $BaTiO_3$:LiF Ceramics," J. Mat. Res. (in press).

23. C. A. Randall, G. A. Rossetti and W. Cao, "Spacial Variations of Polarization in Ferroelectrics and Related Materials."

24. Jayu Chen, Qi Chang Xu, M. Blaszkiewicz, R. Meyer, Jr. and R. E. Newnham, "Lead Zirconate Titanate Films on Nickel-Titanium Shape Memory Alloys: SMARTIES," J. Amer. Ceram. Soc. 75 (10), 2891 (1992).

Actuator Studies

25. D. Damjanovic and R. E. Newnham, "Electrostrictive and Piezoelectric Materials for Actuator Applications," J. Intell. Mat. Syst. and Struct. 3, 190 (1992).

26. Y. Sugawara, K. Onitsuka, S. Yoshikawa, Q. C. Xu, R. E. Newnham and K. Uchino, "Metal-Ceramic Composite Actuators," J. Amer. Ceram. Soc. 75 (4), 996 (1992).

27. Q. C. Xu, A. Dogan, J. Tressler, S. Yoshikawa and R. E. Newnham, "Ceramic-Metal Composite Actuators," Ferroelectrics Special Issue.

28. K. Uchino, "Piezoelectric Ceramics in Smart Actuators and Systems," Proc. 1st European Conference on Smart Structures and Materials.

29. A. Furuta, Ki-Young Oh and K. Uchino, "Shape Memory Ceramics and Their Application to Latching Relays," Sensors and Materials 3 (4), 205 (1992).

30. K. Uchino and A. Furuta, "Destruction Mechanisms in Multilayer Ceramic Actuators," Proc. ISAF 1992, Greenville, South Carolina, pp. 195.

31. Q. Jiang, Wenwu Cao and L. E. Cross, "Electric Fatigue Initiated by Surface Contamination in High Polarization Ceramics," Proc. ISAF 1992, Greenville, South Carolina, pp. 107.

32. Q. Jiang, Wenwu Cao and L. E. Cross, "Electric Fatigue in PLZT Ceramics."

Integration Issues

33. Wenwu Cao, Q. M. Zhang and L. E. Cross, "Theoretical Study on the Static Performance of Piezoelectric Ceramic-Polymer Composite with 1-3 Connectivity," J. Appl. Phys. 72 (12), 5814 (1992).

34. Q. M. Zhang, Wenwu Cao, H. Wang and L. E. Cross, "Characterization of the Performance of 1-3 Type Piezocomposites for Low Frequency Applications," J. Appl. Phys. 73 (3), 1403 (1993).

35. Q. M. Zhang, Wenwu Cao, H. Wang and L. E. Cross, "Strain Profile and Piezoelectric Performance of Piezocomposites with 2-2 and 1-3 Connectivities," Proc. ISAF 1992, Greenville, South Carolina, pp. 252.

36. Q. M. Zhang, H. Wang and L. E. Cross, "Piezoelectric Tubes and 1-3 Type Tubular Composites as Tunable Actuators and Sensors."

37. Q. M. Zhang, H. Wang and L. E. Cross, "Piezoelectric Tubes and Tubular Composites for Actuator and Sensor Applications."

Processing Studies

38. Thomas R. Shrout and Scott L. Swartz, "Processing of Ferroelectric and Related Materials: A Review."

39. G. A. Rossetti, D. J. Watson, R. E. Newnham and J. H. Adair, "Kinetics of the Hydrothermal Crystallization of the Perovskite Lead Titanate," J. Crystal Growth 116, 251 (1992).

40. A. V. Prasadarao, U. Selvaraj, S. Komarneni and A. S. Bhalla, "Sol-Gel Synthesis of $Ln_2(Ln = La, Nd) Ti_2O_7$," J. Mat. Res. 7 (10), 2859 (1992).

41. A. V. Prasadarao, U. Selvaraj, S. Komarneni and A. S. Bhalla, "Sol Gel Synthesis of Strontium Pyroniobate and Calcium Pyroniobate," J. Amer. Ceram. Soc. 75 (10), 2697 (1992).

42. A. V. Prasadarao, U. Selvaraj, S. Komarneni and A. S. Bhalla, "Fabrication of $La_2Ti_2O_7$ Thin Films by A Sol-Gel Technique," Ferroelectrics Letters 14, 65 (1992).

43. S. F. Wang, U. Kumar, W. Huebner, P. Marsh, H. Kankel and C. G. Oakley, "Grain Size Effects on the Induced Piezoelectric Properties of 0.9 PMN-0.1PT Ceramic," Proc. ISAF 1992, Greenville, South Carolina, pp. 148.

44. C. A. Randall, A. D. Hilton, D. J. Barber and T. R. Shrout, "Extrinsic Contributions to the Grain Size Dependence of Relaxor Ferroelectric $Pb(Mg_{1/3}Nb_{2/3})O_3:PbTiO_3$ Ceramics," J. Mat. Res. 8 (4) (1993).

45. B. V. Hiremath, R. E. Newnham and L. E. Cross, "Barrier Layer Capacitor Using Barium Bismuth Plumbate and Barium Plumbate," J. Amer. Ceram. Soc. 75 (11), 2953 (1992).

46. U. Kumar, S. F. Wang, S. Varanasi and J. P. Dougherty, "Grain Size Effects on the Dielectric Properties of Strontium Barium Titanate," Proc. ISAF 1992, Greenville, South Carolina, pp. 55.

4

Processing Studies (continued)

47. U. Kumar, S. F. Wang and J. P. Dougherty, "Preparation of Dense Ultra-Fine Grain Barium Titanate-Based Ceramics," Proc. ISAF 1992, Greenville, South Carolina, pp. 70.

Thin Film Ferroelectrics

48. J. Chen, K. R. Udayakumar, K. G. Brooks and L. E. Cross, "Dielectric Behavior of Ferroelectric Thin Films at High Frequencies," Proc. ISAF 1992, Greenville, South Carolina, pp. 182.

49. K. Uchino, N-Y. Lee, T. Toba, N. Usuki, H. Aburatani and Y. Ito, "Changes in the Crystal Structure of RF-Magnetron Sputtered $BaTiO_3$ Thin Films," J. Chem. Soc. Japan 100 (9), 1091 (1992).

50. R. E. Newnham, K. R. Udayakumar and S. Trolier-McKinstry, "Size Effects in Ferroelectric Thin Films," *Chemical Processing of Advanced Materials*, Edited by Larry L. Hench and Jon K. West, John Wiley and Sons, Inc. (1992).

51. S. Trolier-McKinstry, H. Hu, S. B. Krupanidhi, P. Chindaudom, K. Vedam and R. E. Newnham, "Spectroscopic Ellipsometry Studies on Ion Beam Sputter Deposited $Pb(Zr, Ti)O_3$ Films on Sapphire and Pt-Coated Silicon Substrates."

ACTUATOR STUDIES
(continued)

APPENDIX 28

Piezoelectric ceramics in smart actuators and systems

KENJI UCHINO
Materials Research Laboratory, The Pennsylvania State University
University Park, PA 16802-4801, USA

ABSTRACT: In these several years piezoelectric and electro-strictive actuators have become very popular for micro-positioning in optical and precision machinery fields. Aiming at wide commercialization of these actuators, many investigations have been made in the improvement of ceramic materials for actuators, designs of the devices and control and systemization of the actuators. This paper reviews recent applications of piezoelectric/ electrostrictive ceramics from a viewpoint of "smart" actuators and systems.

1. INTRODUCTION

"Smartness" in the words of "smart" materials and structures is defined by three functions of "sensing," "actuating," and "active control" of environmental conditions with some intelligence. Dental braces made rom shape memory alloys and electrochromic grass windows are often cited in the literatures as smart materials. This paper reviews recent applications of piezoelectric/ electrostrictive and their related ceramics from a viewpoint of "smart" actuators and systems.[1]

2. ACTUATOR MATERIALS

A passively smart materials is exemplified by the lead magnesium niobate (PMN) based ceramic, which can exhibit a large electrostriction $(\Delta l/l \sim 10^{-3})$ witnout any hysteresis and aging effect during an electric field cycle (Fig. 1).[2] A composite actuator structure called "moonie" has been developed to amplify the small displacement induced in a multilayer piezoelectric device (Fig. 2). Passive damper application is another smart usage of piezoelectrics, where mechanical noise vibration is radically suppressed by the converted electric energy dissipation through Joule heat when a suitable resistance is connected to the piezoelectric plate.[3] Piezoelectric: carbon black: polymer composites are promising useful designs for practical use.
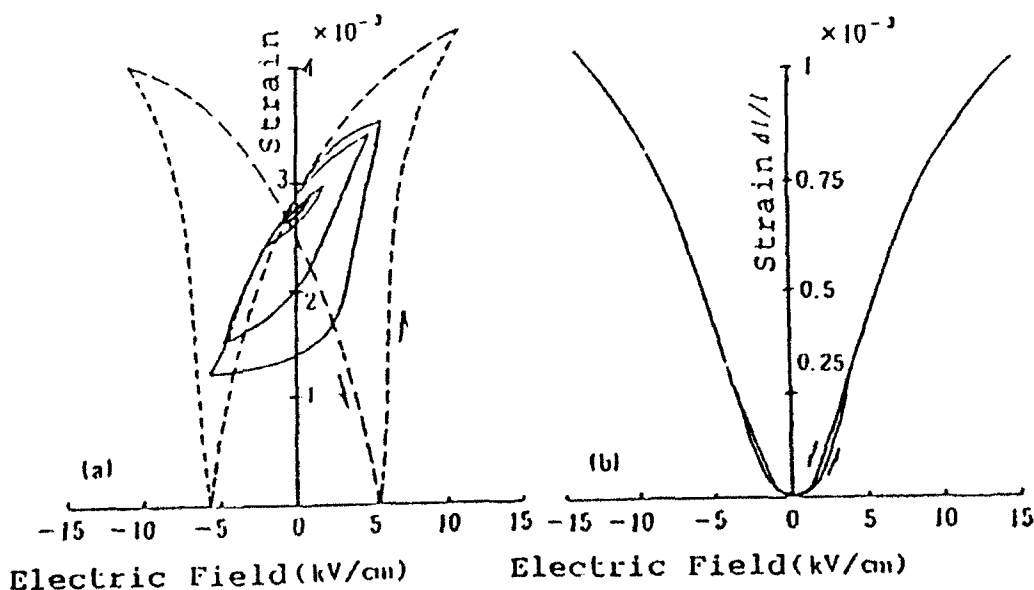

Figure 1 Electric field induced strain in a piezoelectric lead lanthanum zirconate titanate (PLZT) (a); and in an electrostrictive lead magnesium niobate(PMN) based ceramic (b).

An actively smart material is exemplified by the video tape head positioner made from a lead zirconate titanate (PZT) bimorph with sensor and actuator-divided electrodes.[4]

Monomorphs and shape memory ceramics belong to very smart materials. A monomorph device made of a semiconductive piezoelectric plate generates the Schottky barrier when metal electrodes are coated on the faces, providing non-uniform distribution of the electric field even in a compositionally uniform ceramic (Fig. 3). A superimposed effect of piezo-electricity and semiconductivity leads to a bending deformation in a total ceramic plate.[5] The strains associated with phase transitions such as an antiferroelectric-to-ferroelectric transition in lead zirconate stanate-based ceramics reach up to 0.4%, which is much larger than that expected in electrostrictors (Fig. 4). Moreover, this field-induced transition exhibits a shape memory effect in appropriate compositions, and such ceramics are useful for the applications to latching relay and a mechanical clamper.[6]
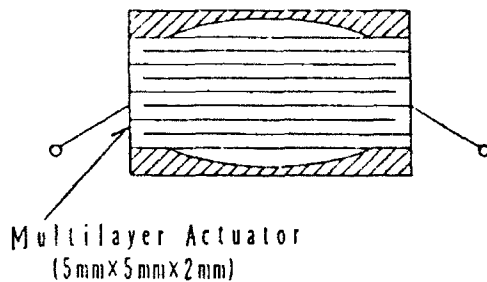
Figure 2 Structure of a composite
actuator "moonie."

Figure 3 Electron energy band (Schottky
barrier) models in monomorph
devices (n-type semiconductor).

(a)

$x=0.60, y=0.055$

(b)

$x=0.70, y=0.045$

Figure 4 Longitudinal induced strains of
$Pb_{0.99}Nb_{0.02}((Zr_xSn_{1-x})_{1-y}Ti_y)_{0.98}O_3$
at room temperature.

A photostrictive actuator is the best example of intelligent materials including sensing, actuating and drive/control functions in a unique material.[7] In certain ferroelectrics a phenomenon by which a constant electromotive force is generated with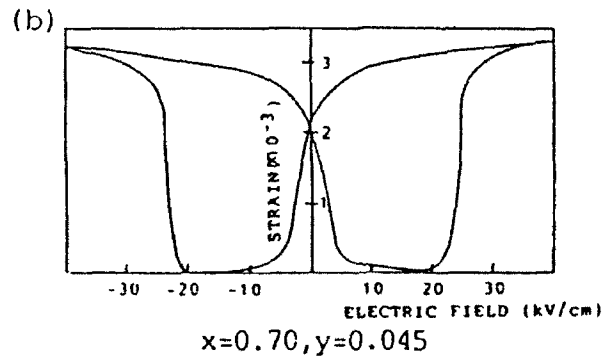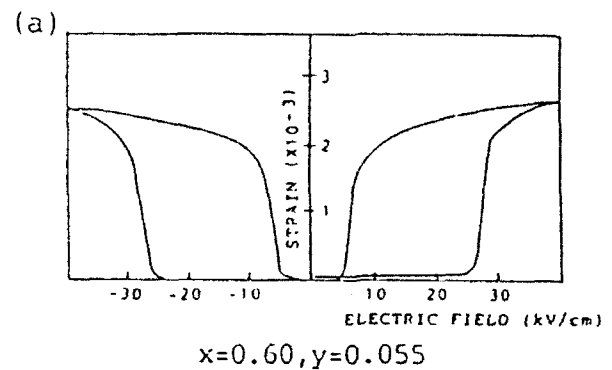 exposure of light has been observed. A photostrictive effect is expected as a result of the coupling of the photovoltaic and inverse piezoelectric effects. A remote control miniature walking robot, which is activated with illumination, is currently being fabricated (Fig. 5). Two photostrictive PLZT bimorphs were combined together and each plate exhibits a minute photo-induced displacement on the order of 150μm. Alternative illumination causes a slow moving of the ceramic device.

3. ACTUATOR SYSTEMS

Pulse voltage drive of piezoelectric actuators is only one-way control without a feedback system, but very important for improving the response of ceramic actuators.[8] Figure 6 shows transient vibrations of a bimorph excited after a pseudo-step voltage applied. The rise time is varied around the resonant period. It is concluded that overshoot or ringing of the tip displacement is completely suppressed when the rise time is precisely adjusted to the resonance period of the piezo-device.

A flight actuator consisting of a pulse-driven piezoelectric element and a steel ball is a very suggestive mechanism, even if it would not be denoted as a smart system. A 2mm steel ball can be hit up to 20mm by a 5μm displacement induced in a multilayer actuator with quick response.
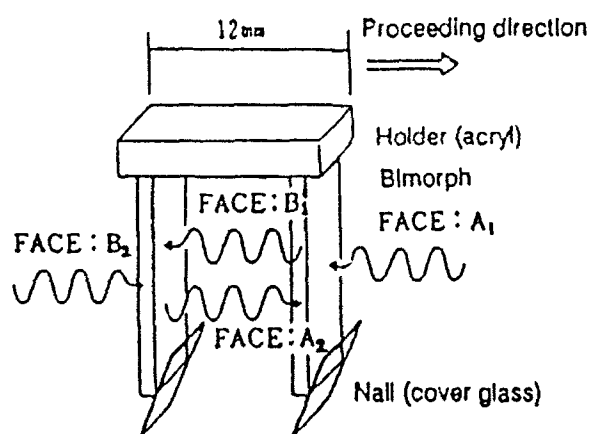

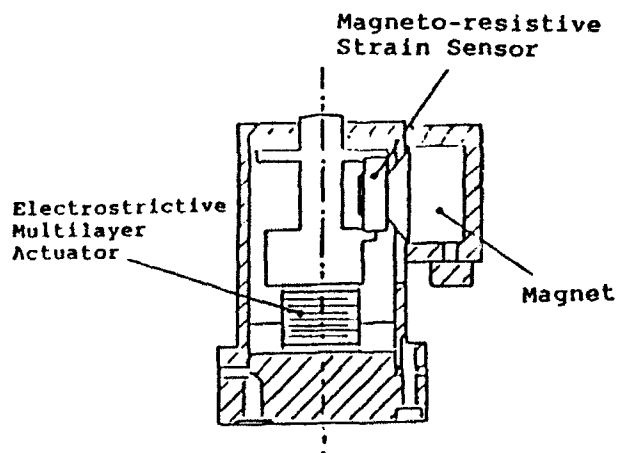Figure 5 Photo-driven miniature walking device.

Figure 7 Micro displacement actuator with a magneto - resistive strain sensor.
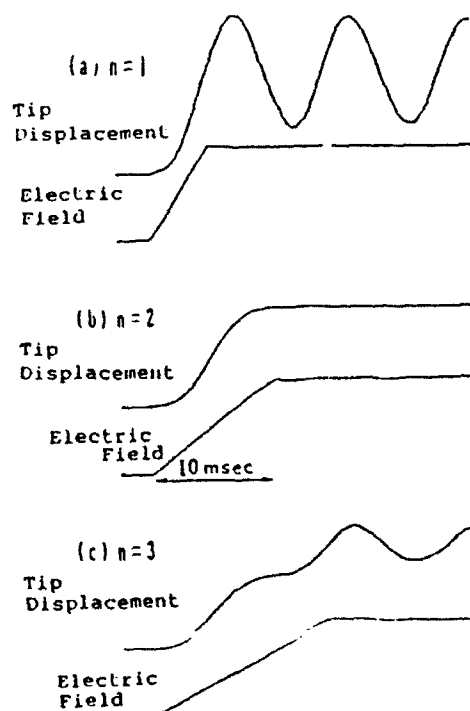

Figure 6 Transient vibration of a bimorph excited after a pseudo - step voltage applied. n is a time scale in the unit of a half of the resonance period.
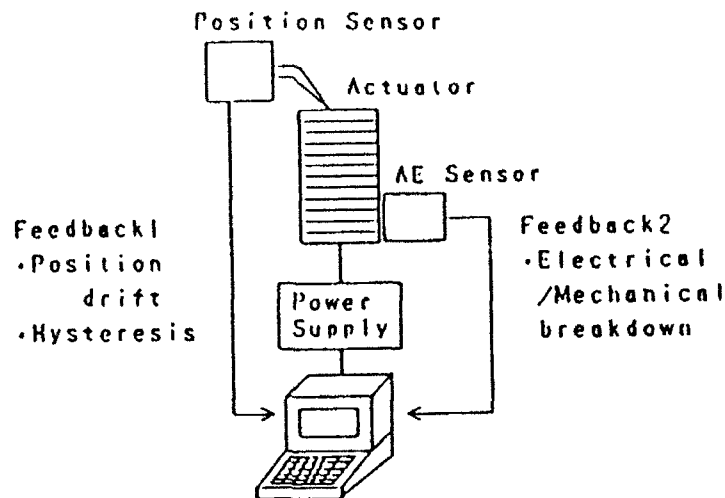
Position Sensor

Actuator

AE Sensor

Feedback1
•Position
     drift
•Hysteresis

Power
Supply

Feedback2
•Electrical
/Mechanical
breakdown

Figure 8   Very smart actuator system with a reliability test function as well as
           a position sensor.

A **smart system** is typically exemplified by a precision lathe machine. A
micro displacement actuator has been manufactured using an electrostrictive
multilayer actuator, a magneto-resistive strain sensor and an adaptive control
circuitry (Fig. 7). The feedback control has suppressed the position deviation of
the cutting edge when pushing stress is produced during cutting process. The
cutting accuracy in less than ±0.01μm is now available.

A **very smart system** contains a reliability test system, which can stop an
actuator system safely without causing any serious damages on to the work, e.g. in
a lather machine. Acoustic emission measurement of a piezo-actuator under a
cyclic electric field is a good candidate for estimating the life time of the
actuators.[9]

4. CONCLUSION

The bright future of piezoelectric/electrostrictive actuators has been
initiated and even greater commercial participation in their continued growth and
application is anticipated.

REFERENCES

1. K. Uchino, Piezoelectric / Electrostrictive Actuators, Morikita Pub. Co.,
   Japan (1986)
2. L.E.Cross, S.J.Jang, R.E.Newnham, S.Nomura and K.Uchino, Ferroelectrics
   23, 187 (1980)
3. K. Uchino and T.Ishii, J.Ceram. Soc. Jpn. 96, 863 (1988)
4. A.Ohgoshi and S.Nishigaki, Ceramic Data Book '81, Industrial Products
   Tech. Assoc., Japan, p.35 (1981)
5. K.Uchino, M.Yoshizaki, K.Kasai, H.Yamamura, N.Sakai and H.Asakura, Jpn.
   J. Appl. Phys. 26, 1046 (1987)
6. K.Uchino, Proc. MRS Int'l. Mtg. on Adv. Mats. 9,489 (1989)
7. M.Tanimura and K.Uchino ,Sensors and Mater. 1, 47 (1988)
8. S.Sugiyama and K.Uchino, Proc. 6th IEEE int'l Symp. Appl. Ferroelectrics,
   p.637 (1986)
9. T.Hirose and K.Uchino, Ferroelectrics 87, 295 (1988)

APPENDIX 29

Shape Memory Ceramics and
Their Application to Latching Relays

Atsushi Furuta, Ki-Young Oh and Kenji Uchino

Department of Physics, Sophia University,
7-1 Kioi-cho, Chiyoda-ku, Tokyo 102

Basic characteristics of shape memory unimorphs have been measured in detail, and a new latching relay has been fabricated using the shape memory unimorph. This new relay has a very simple structure with compact size and light weight, as compared with the conventional electromagnetic type. The relay is turned ON at 350 V and turned OFF at -50 V with a short-pulse electric field. The response time is about 13 ms under an input electric energy of 7 mJ. The relay can be kept in an ON state for more than a day without applying any electric field.

1. Introduction

The shape memory effect is not only characteristic of certain metal alloys, but is also observed in ceramics. Figure 1 shows the transverse strains induced in the ceramic plates of $Pb_{0.99}Nb_{0.02}[(Zr_{0.6}Sn_{0.4})_{1-y}Ti_y]_{0.98}O_3$ (PNZST) under an applied electric field.[1-3] These strain curves can be classified into three patterns with changing Ti mole fraction.

The ceramic of Type I ($y = 0.060$) is originally antiferroelectric, but can be changed to ferroelectric by applying an electric field, and large strains are generated during the phase transition. It is worth noting that the magnitude of strain is three to four times as large as that of the conventional piezoelectrics. When the electric field is decreased, the phase of the ceramic is changed back to the initial antiferroelectric and the strain recovers. The square-type hysteresis of the strain curve is applicable to digital displacement transducers.

205
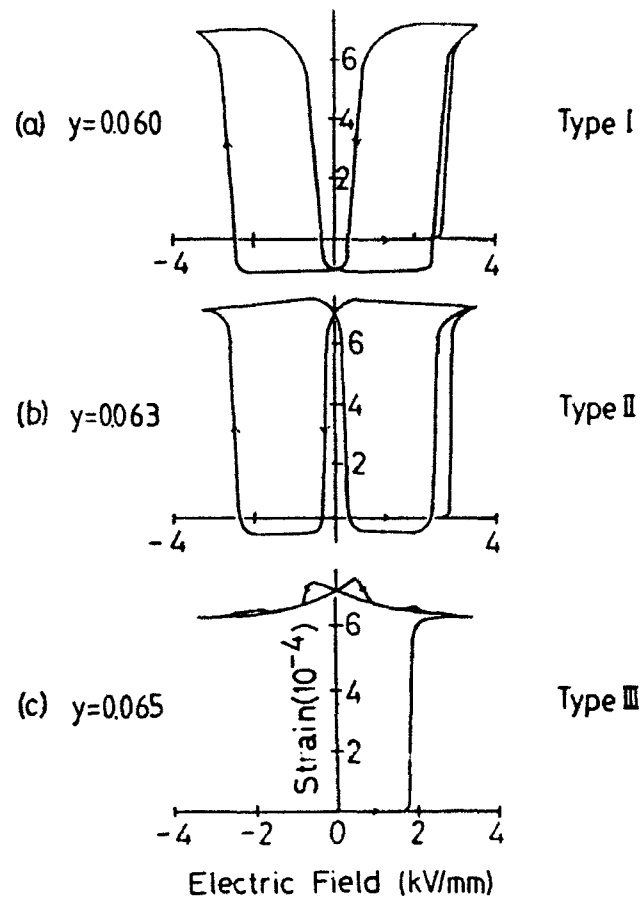
Fig. 1. Transversely induced strains in the $Pb_{0.97}Nb_{0.02}[(Zr_{0.6}Sn_{0.4})_{1-y}Ti_y]_{0.98}O_3$ ceramics at room temperature: (a) $y = 0.06$, (b) $y = 0.063$, (c) $y = 0.065$.

In the case of Type II ($y = 0.063$), once the ceramic changes from antiferroelectric to ferroelectric, the phase is maintained even when the electric field goes down to zero, and the deformation is memorized. To obtain the initial antiferroelectric state, a small reverse bias field should be applied to the sample.

On the contrary, the ceramic of Type III ($y = 0.065$) cannot recover the antiferroelectric state during the electric field cycle after the ferroelectric phase is induced. Thermal annealing up to 50°C is required to recover the initial state.

The strain characteristics of Type II and Type III are denoted as the shape memory effect. In particular, since the PNZST of Type II can be controlled easily by applying electric field, it is the most useful from a practical point of view. This kind of shape memory ceramic requires only a pulse electric field to obtain a permanent displacement, leading to electric energy savings as compared with conventional piezoelectrics, which require continuous application of field.

A latching relay, which will not change its original ON or OFF state without an intentional electric signal even when an accidental electricity shutdown occurs, is one of the best application candidates of the shape memory devices.

This paper describes trial manufacturing of a latching relay using shape memory ceramics, following basic characteristics of a shape memory unimorph as the drive source of the relay.

2. Sample Preparation and Experiments

The PNZST family ceramics of $Pb_{0.99}Nb_{0.02}[(Zr_{0.6}Sn_{0.4})_{1-y}Ti_y]_{0.98}O_3$ were prepared by the conventional sintering process. After mixing and drying the reagent-grade PbO, Nb_2O_5, ZrO_2, SnO_2 and TiO_2 raw materials, the powders were calcined at 850°C for 10 h and sintered at 1270°C for 2 h. The samples of 10 mm diameter and 0.2 mm thickness were used for basic strain measurements after being silver-electroded. The samples of 22 mm × 7 mm area and 0.2 mm thickness were used for fabricating unimorphs. Figure 2 shows the structure of the unimorph, which is composed of two ceramic plates, A and B, bonded together with adhesive. Plate A is coated with silver electrode. When an electric field is applied to plate A,
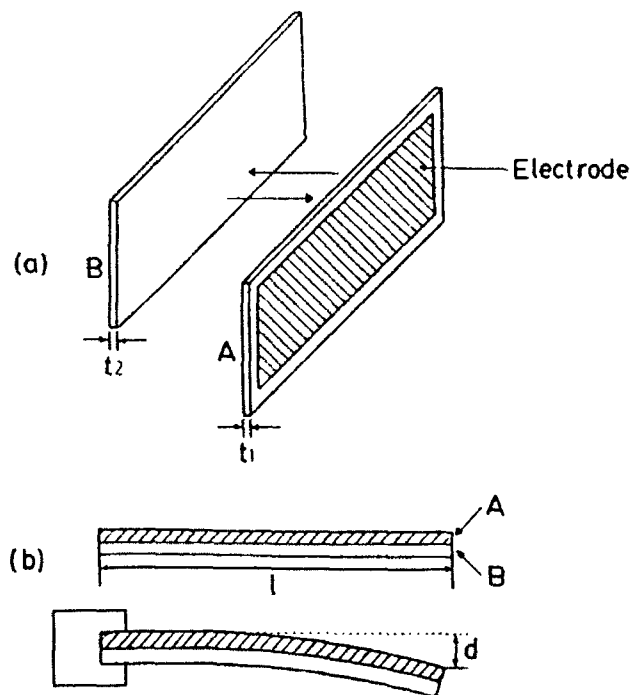
Fig. 2. Structure of a unimorph device.

the expansive strain is induced only in plate A, not in plate B; then finally the unimorph generates bending motion.

For measuring induced strains in single-plate samples, a contact-type strain sensor (Millitron, No. 1202) was used. For the tip displacement of the unimorph, d in Fig. 2, and load characteristics in the induced displacement, a noncontact-type displacement sensor (Kaman, KD-2300) was used.

3. Results

3.1 Characteristics of the shape memory unimorph

Figure 3 shows induced strains of the single-plate-type samples of $Pb_{0.99}Nb_{0.02}[(Zr_{0.6}Sn_{0.4})_{1-y}Ti_y]_{0.98}O_3$ ($y = 0.0625 - 0.0645$). Some results have been reported in ref. 4. The PNZST in the above composition range exhibits the shape memory effect. Figure 4 shows the tip displacements of the unimorph. It is

a) y=0.0625

d) y=0.0640

b) y=0.0630

e) y=0.0645

c) y=0.0635
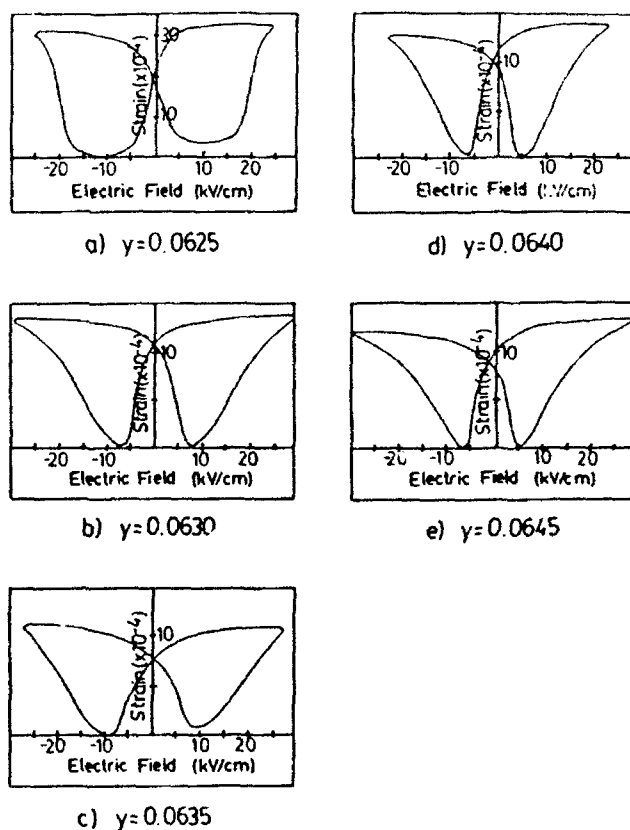
Fig. 3. Strain-vs-field characteristics in the single-plate-type samples of PNZST for various Ti mole fractions.
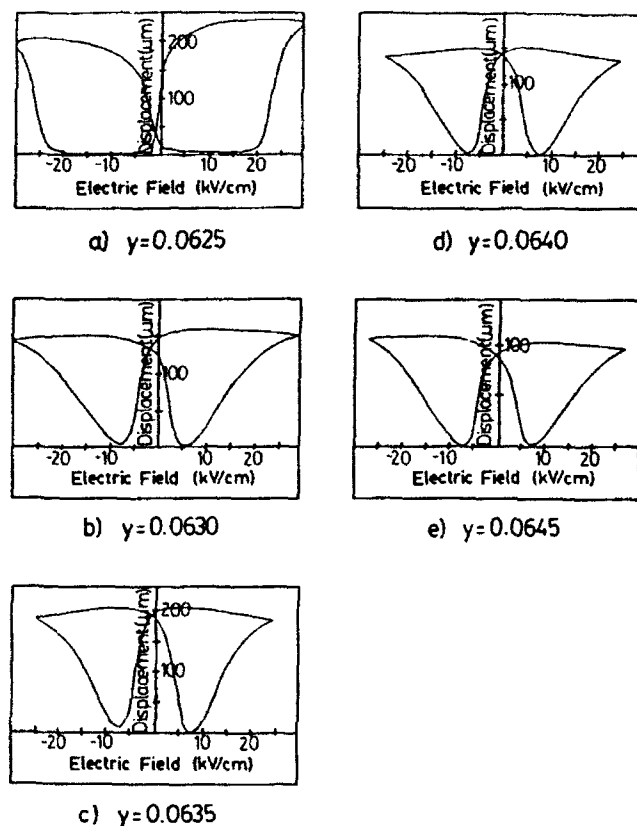
Fig. 4. Displacement-vs-field characteristics of the unimorphs of PNZST for various Ti mole fractions.

noteworthy that the sample with $y = 0.0625$, exhibiting the shape memory effect in the single plate, does not exhibit the shape memory characteristic in the unimorph design. Figure 5 shows the time dependence of the tip displacement of the uni-morphs ($y = 0.0625$ and $y = 0.0630$). The recovery in the $y = 0.0625$ sample to the antiferroelectric phase is probably attributable to compressive stress generated during the bending process.

Figure 6 shows the temperature dependence of the unimorph bending measured in $y = 0.0630$. At $0°C$, once the ferroelectric phase is induced, the ceramic will not recover antiferroelectricity under applied reverse bias electric field. On the other hand, at $40°C$ the electric field required to cause the phase transition becomes great and the unimorph loses the shape memory effect. To realize a complete shape memory phenomenon, the temperature should be controlled between $10°C$ to $30°C$ for this composition. A similar characteristic change is also observed when the Ti mole fraction is changed from $y = 0.060$ to $y = 0.065$.

Figure 7 shows the dynamical response of the unimorph ($y = 0.0630$). In the
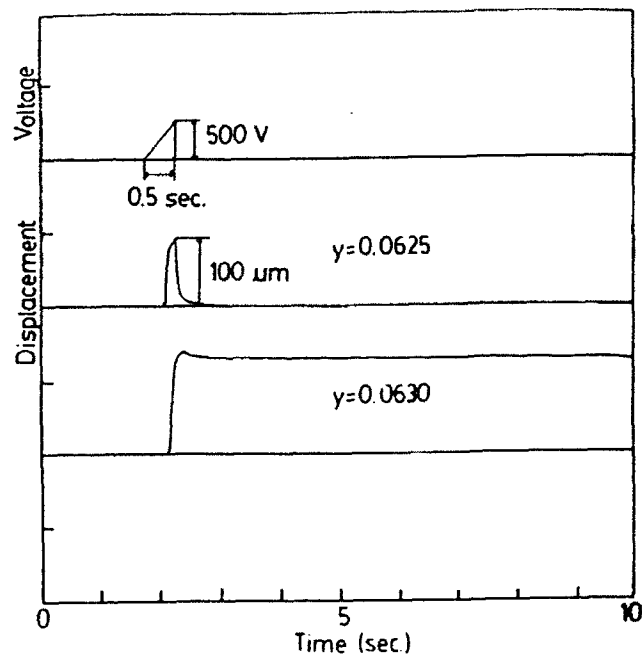
Fig. 5. Time dependence of the tip displacement change in the unimorphs.

case of the conventional piezoelectric, a continuous application of the electric field is required to maintain a constant displacement; meanwhile, the shape memory ceramic can be driven by a pulse electric field. When the unimorph is driven by a triangular pulse with a rise time of 3.0 ms (Fig. 7(a)), overshoots and ringing of the tip displacement are observed. It is important to note that the phase transition arises quickly enough to generate the following resonant vibration. When the rise time of the electric field is adjusted to 4.7 ms (Fig. 7(b)), which is the sum of the mechanical resonant period (2.2 ms) and the lag time, to cause phase transition (2.5 ms), the ringing can be suppressed completely. Too slow a rise time of 6.0 ms (Fig. 7(c)) again causes the ringing vibrations. Overshoots and ringing of the unimorph element would cause chattering in the latching relay and the response would become very slow. Therefore, an electric field with the rise time corresponding to the mechanical resonant period is required.

To operate the mechanical snap-action switch element, at least 20 gf of the generative force is necessary for the unimorph as well as 50 μm of the displacement. The relationship between the tip displacement and the load for the unimorph was measured using metal weights applied to the tip position (Fig. 8). Generative force of more than 50 gf can be practically induced both at the maximum and zero field. The magnitude of the maximum generative force of the shape memory unimorph, which is estimated from the intercept on the horizontal axis, is about 90 gf, which is
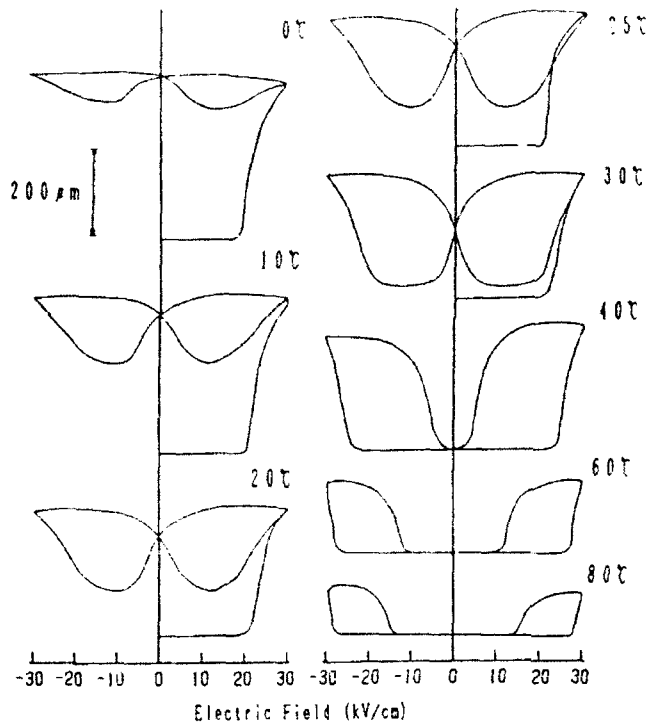
Fig. 6. Temperature dependence of the tip displacement in the unimorph with $y = 0.063$.

twice as large as that of the conventional piezoelectric bimorph. This is probably due to the strain bias caused by the spontaneous strain change from the antiferroelectric to the ferroelectric phase.

3.2 Characteristics of the latching relay

We have fabricated a new latching relay using the shape memory unimorph. Figure 9 shows the structure of the latching relay, which is composed essent ally of a mechanical snap-action switch and a driving unimorph device. The snap-action switch is easily driven by a 50 μm displacement, having mechanically bistable states. The size of the relay is very compact, $20 \times 10 \times 10$ mm^3, as compared to a conventional electromagnetic type ($20 \times 26 \times 34$ mm^3). Figure 10 shows the basic ON/OFF function of the new relay. The relay is turned ON at about 350 V and turned OFF at -50 V. The voltage required for switching can be lowered by using multimorph structures. Dynamical response of the newly developed latching relay is shown in Fig. 11(a). The response of the conventional electromagnetic latching relay is also shown in Fig. 11(b) for comparison with the new relay. A pulse electric field with the mechanical resonant period of the shape memory unimorph is applied

212
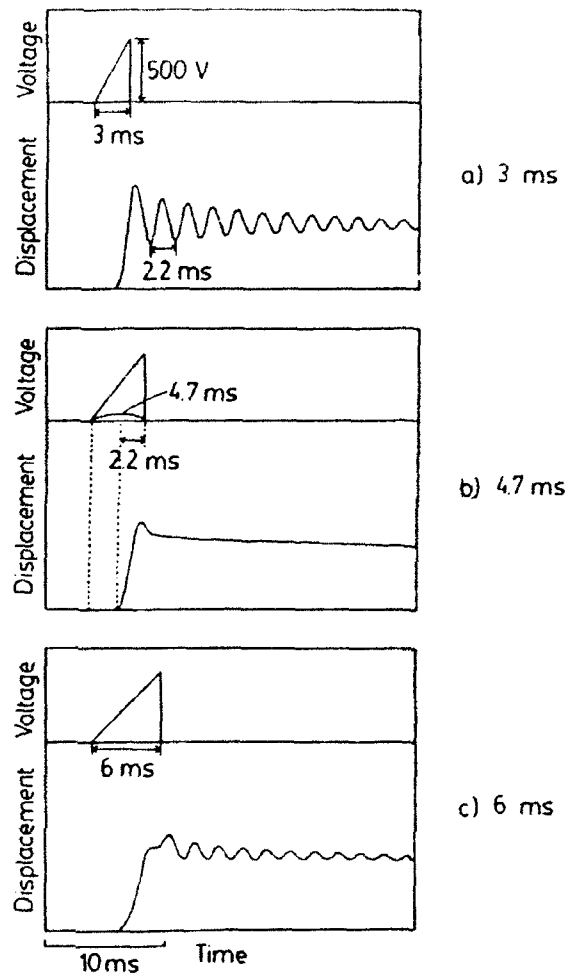
Fig. 7. Dynamical response of the tip displacement of the shape memory unimorph with $y = 0.063$ under various drive pulse conditions.

so as to suppress the ringing at the tip of the unimorph. Chattering was still observed, probably due to an additional mechanical soft leaf spring at the snap-action switch. The rise time of the new relay is 1.8 ms, which is much shorter than that of the electromagnetic relay (8.5 ms), although the former needs 13 ms to stabilize the ON state, which is slightly longer than the 9 ms of the latter relay; this suggests a potential capability of much faster response if the whole mechanical setup were adjusted to optimize conditions. The newly developed latching relay can be kept in the ON state for more than a day without applying any electric power. The drive power required to turn it ON is about 7 mJ. This energy requirement can be reduced by collecting electric energy in the discharging process. A camera strobe makes a suitable
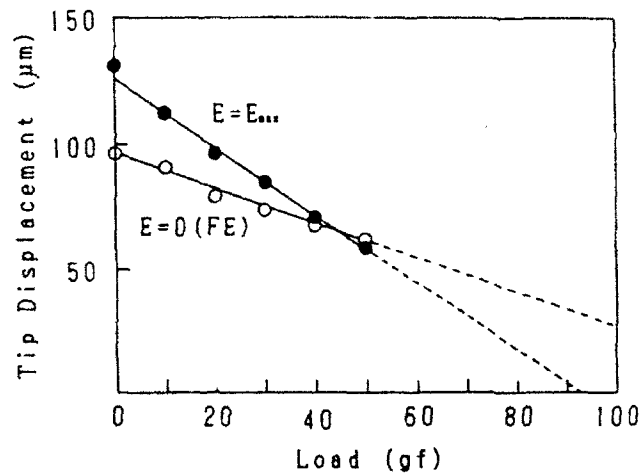
Fig. 8. Tip displacement of the shape memory unimorph ($y = 0.063$) as a function of the external load.
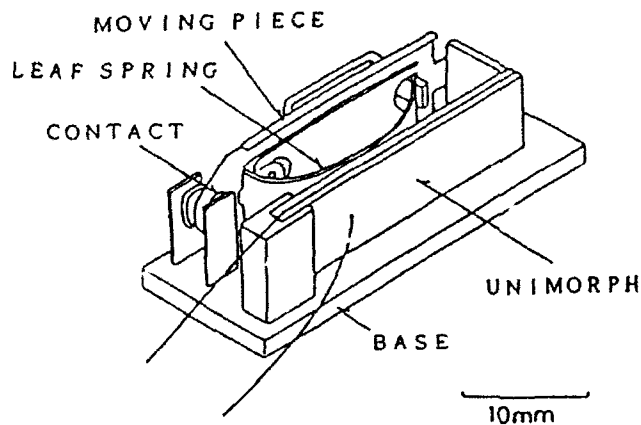
Fig. 9. Structure of the latching relay using the shape memory ceramic.

high-voltage supply for driving the relay, because the relay can be switched only by a short-pulse field of several ms.

4. Conclusions

a) Shape memory ceramic unimorphs have been fabricated as actuator elements. The unimorph shape memory effect can be observed at room temperature for the samples with Ti mole fraction $y = 0.0630$ to $y = 0.0645$ in the

214
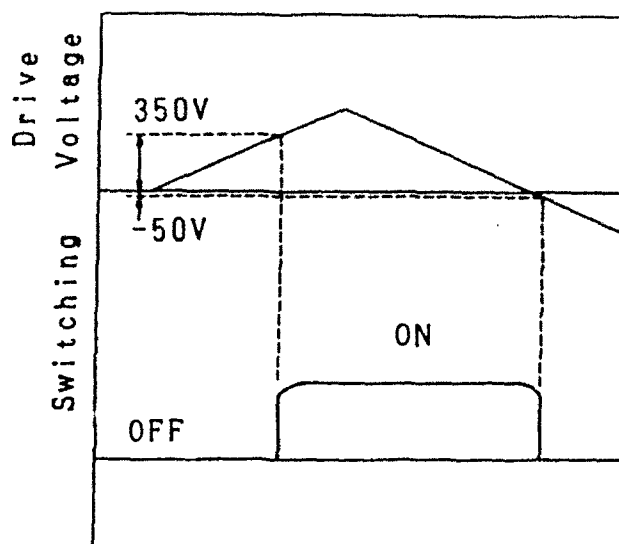
Fig. 10. Basic ON/OFF function of the latching relay using the shape memory ceramic.
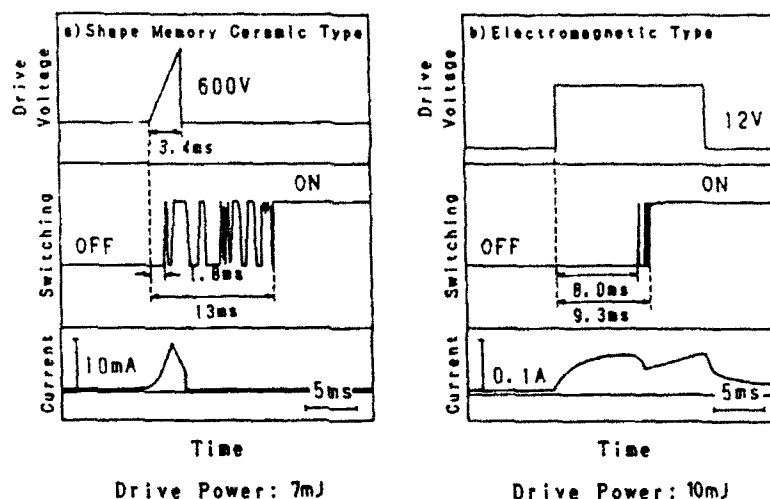
Fig. 11. Dynamical response of the latching relays: (a) shape memory ceramic type, (b) electromagnetic coil type.

$Pb_{0.99}Nb_{0.02}[(Zr_{0.6}Sn_{0.4})_{1-y}Ti_y]_{0.98}O_3$ family.

b)   Mechanical vibration overshoots and ringings at the tip of the unimorph can be completely suppressed by applying an electric field with rise time equal to the sum of the mechanical resonant period and the lag time to cause the phase transition.

c) A compact, lightweight latching relay using a shape memory ceramic ($y = 0.063$) has been fabricated and found to have a quick response compared with the conventional electromagnetic type. The relay is driven simply by applying pulse electric field, and is maintained in the ON state without application of any electric field; this reduces the electric power requirement significantly.

References

1 D. Berlincourt, H. H. Kruger and B. Jaffe: J. Phys. Chem. Solids 25 (1964) 675.
2 K. Uchino: Jpn. J. Appl. Phys. 24 Suppl. 24-2 (1985) 460.
3 K. Uchino: MRS Int'l. Mtg. on Adv. Mater. 9 (1989) 489.
4 K. Y. Oh, A. Furuta and K. Uchino: J. Ceram. Soc. Jpn. 98 [8] (1990) 905.

APPENDIX 30

Destruction Mechanism of Multilayer Ceramic Actuators

Kenji Uchino
Materials Research Laboratory
The Pennsylvania State University
University Park, PA 16802 USA

and

Atsushi Furuta
Tokyo Research Laboratory
Tokin Corporation
Shiboguchi, Takatsu-ku
Kawasaki 213, Japan

Destruction mechanism in multilayer ceramic actuators has been investigated under cyclic electric fields. Crack propagation has been observed dynamically using CCD microscopy, and the accompanying characteristics of the induced displacement and acoustic emission were measured simultaneously. The piezoelectric $Pb(Ni_{1/3} Nb_{2/3}) O_3$ - $PbTiO_3$ and the phase-transition-related actuator material (antiferroelectric) $PbZrO_3$ - $PbSnO_3$ - $PbTiO_3$ exhibit a remarkable difference in the destruction manner probably due to the strain induction mechanism. The effect of layer thickness on the destruction process has also been studied.

Introduction

In these several years piezoelectric/electrostrictive ceramic actuators have become very popular for micro-positioning in optical and precision machinery fields and active vibration suppression in mechanical structures.[1] The expanding number of applications of ceramic actuators has made the endurance of the devices very important.

This paper describes the destruction mechanism of multilayer-type ceramic actuators observed by optical microscopy, induced displacement and acoustic emission measurements, and proposes a safety system which can stop the actuator before its troublesome sudden complete collapse.

Experiments

Multilayer model actuators were prepared by tape casting method. The samples simulating the interdigital electrode configuration [Fig. 1(a)] used in this experiment have only one internal ceramic layer with a thickness of 100 μm, 200 μm or 300 μm, as shown in Fig. 1(b).

The piezoelectric $Pb(Ni_{1/3}Nb_{2/3})_{0.6} Ti_{0.4}O_3$ (PNNT) and the phase-transition-related actuator material $Pb_{0.99}Nb_{0.02}[(Zr_{0.7}Sn_{0.3})_{0.955}Ti_{0.045}]_{0.98}O_3$ (PNZST) were prepared, and the average grain size of the device was roughly the same (~ 5 μm), independent of the composition and the layer thickness. The PNZST is initially antiferroelectric, but changes into ferroelectric under an applied electric field.[2] Rather isotropic expansive strains are associated with this phase transition, and the magnitude of the strain ($\sim 1.5 \times 10^{-3}$) is twice larger than that of the piezoelectric PNNT. The longitudinally and transversely induced strains in the piezoelectric PNNT are 0.8×10^{-3} and -0.3×10^{-3}, respectively, with opposite sign.[3]

Note that the multilayer model actuator used in this experiment exhibits an exaggeratedly large internal stress concentrated around the electrode edge so as to accelerate the failure of multilayer actuators.

Figure 2 show the measuring system composed of a CCD microscope (Toshiba, IK-C40), a displacement sensor (Millitron, Nr. 1301) and an acoustic emission sensor (NF Circuit Design Block, AE-905). The sample was driven by a triangular electric field of $E_{max} = 2$-4 kV/mm at 0.1 Hz.

Results

Crack Propagation: Crack generation and propagation resulting from the internal stress was observed and recorded dynamically using a CCD microscope and a VCR. Figures 3(a) and 3(b) show typical crack propagation processes observed for the PNNT and PNZST samples (200 μm in layer thickness). The crack initiates at the internal electrode edge in the PNNT sample and propagates to another electrode obliquely, also outward of the electrode and along the ceramic-metal electrode interface. On the contrary, the crack starts between the pair electrodes slightly inside the electrode edge in the PNZST, then propagates along the center area, finally branching around the electrode edge. It is noteworthy that the crack opens wide under the electric field and closes at zero field.

This difference is probably due to the difference in internal stress distribution. The sign of the longitudinally - or transversely-induced strain is opposite in the piezoelectrics, while in antiferroelectrics undergoing a phase change, rather isotropic expansive strains are induced in both directions. Therefore, the internal stress distribution in antiferroelectrics differs from that of piezoelectrics.

Similar crack propagation processes were observed in the different layer-thickness samples, however, significant differences were recognized in the fracture toughness. Figures 4(a) and 4(b) plot the layer thickness dependence of the critical deformation cycles required for the initial crack generation and of the crack propagation speed per drive cycle (measured in PNZST). A dramatic improvement in the fracture toughness is obtained in the thinner layer sample, even though the driving electric field is the same of all samples. The reason is not clear, but it may be related to the ratio between the grain size and the layer thickness.

Displacement Changes during Failure: The destruction of the device brings a change in the induced displacement. Figures 5(a) and 5(b) show the variation of the induced displacement during the crack propagation process for the model actuators of PNNT and PNZST, respectively, with a layer thickness of 200 μm. The displacement is enhanced remarkably at the initial stage, this can probably be attributed to the bending deformation associated with the crack opening and closing process. Further increase in the number of deformation cycles leads to a decrease in the magnitude of the displacement. The effective electric field in the ceramics decreases because the narrow air gap is associated with complete crack formation.

Variation of Acoustic Emission: Acoustic emission (AE) events were counted during the destruction process of the PNZST sample with a layer thickness of 200 mm (Fig. 6). The AE count increases remarkably after the crack initiation, reaching a maximum at 60 cycles, where the crack propagation speed is maximum, and the largest displacement is observed. Later, the AE count leveled off after the crack was completed.
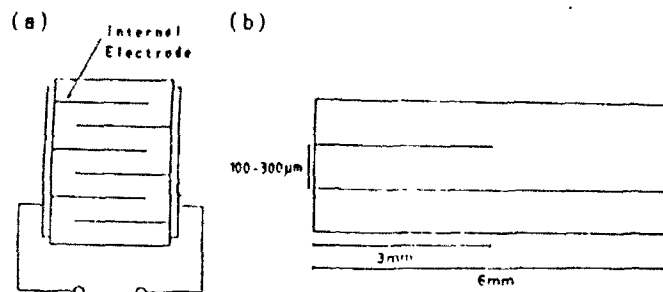
Fig. 1   Structure of (a) conventional multilayer actuator with an interdigital electrode, and (b) electrode configuration of a model actuator used in this study.
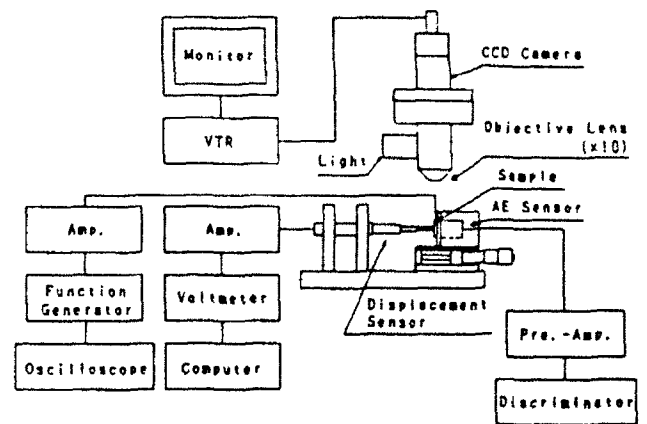
Fig. 2   Measuring system for the crack propagation experiments.
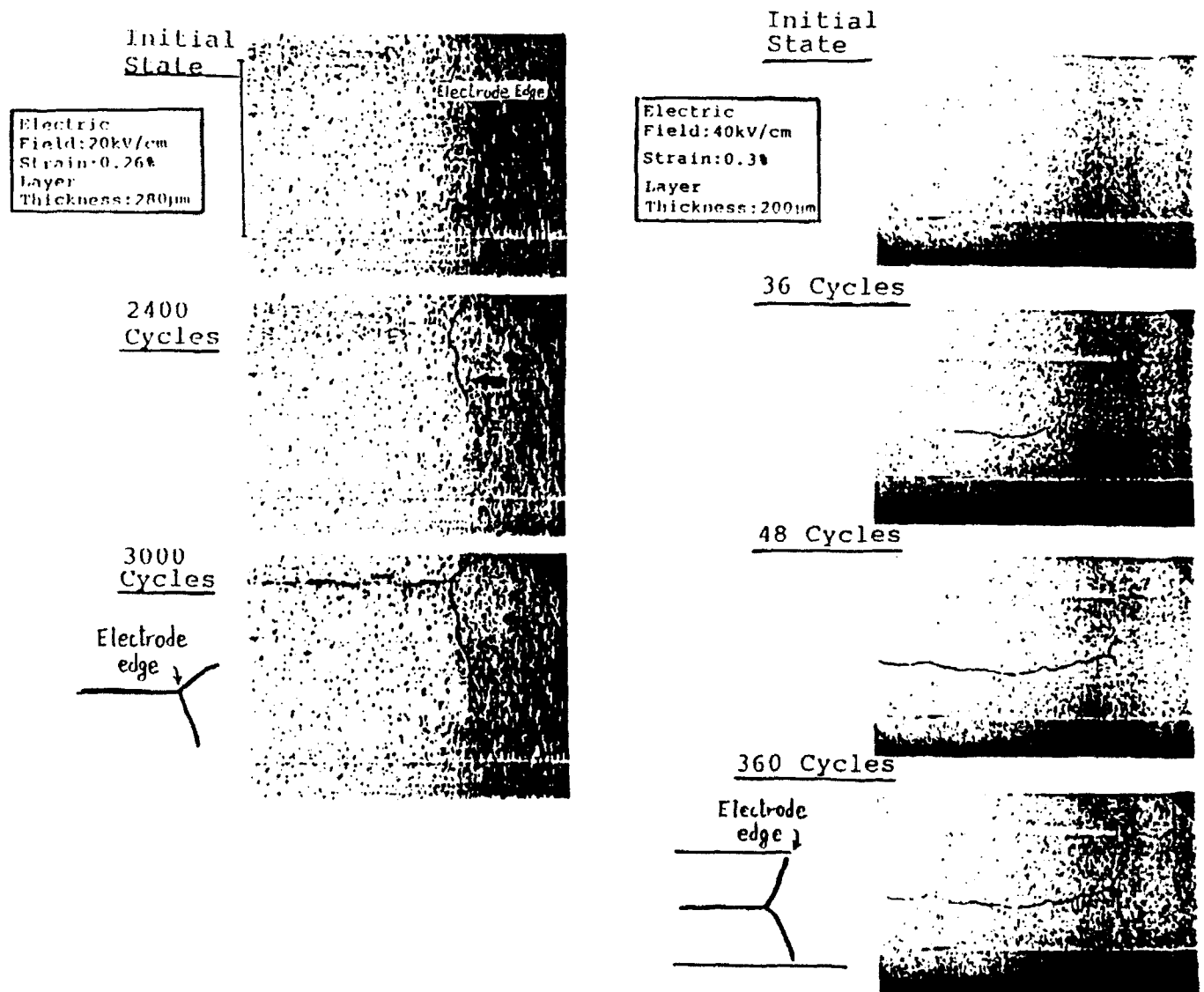
Fig. 3   Crack generation and propagation process in the multilayer model actuator.
          (a) Piezoelectric PNNT, and (b) antiferroelectric PNZST.

196
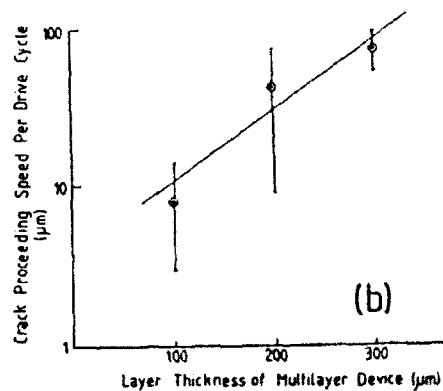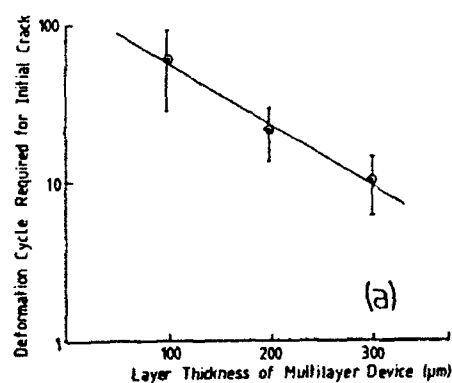
Fig. 4   Layer thickness dependence of the critical deformation cycle required for the initial crack generation (a), and of the crack propagation speed per drive cycle (b).
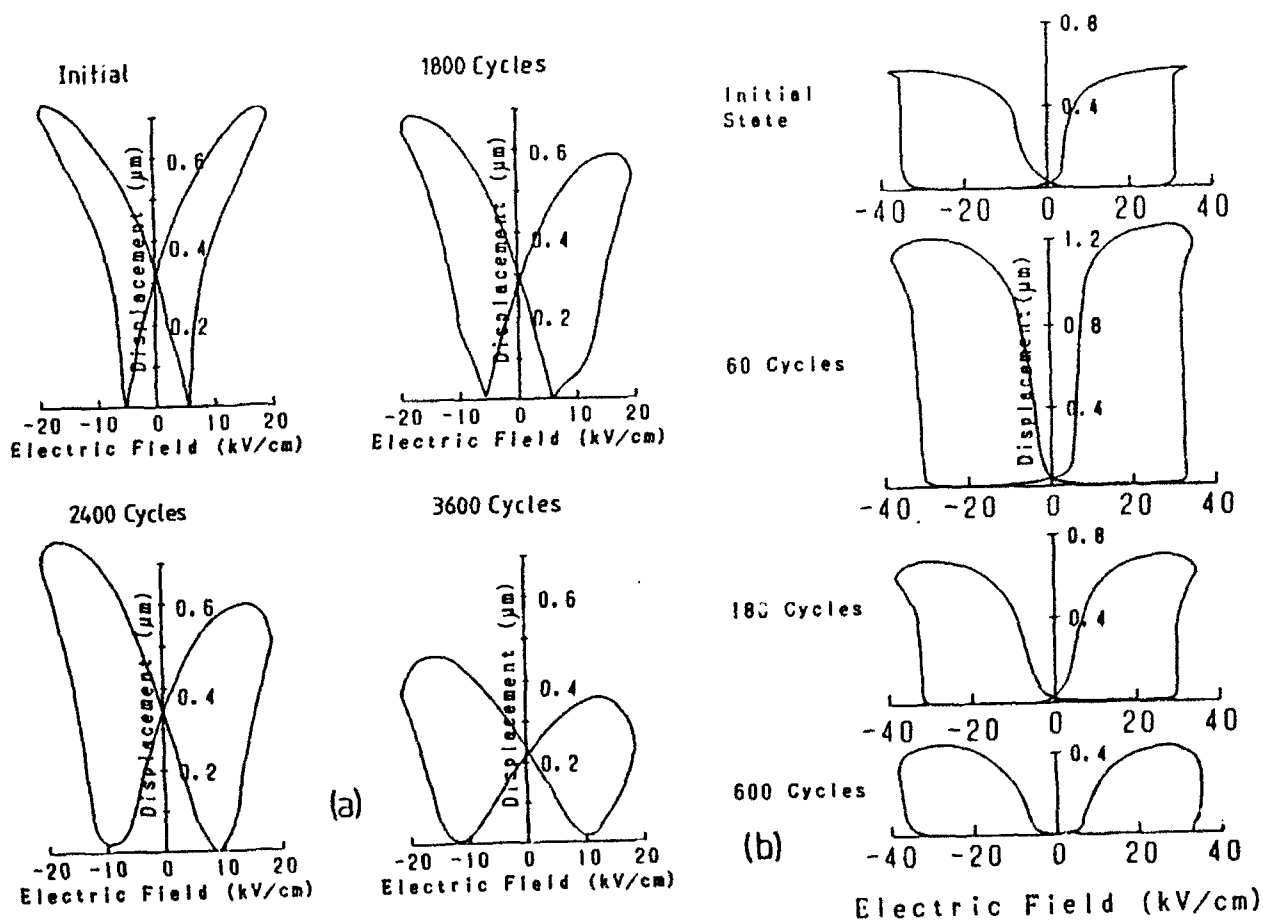
Fig. 5   Variation of the displacement during the destruction. (a) PNNT and (b) PNZST.
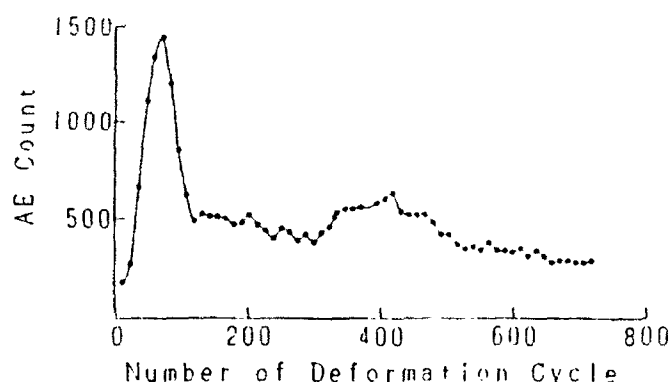
Fig. 6   Changes in acoustic emission count during the fracture process measured in a model actuator of PNZST.
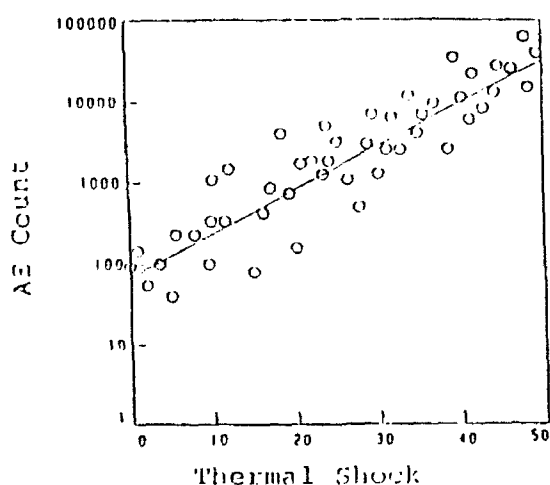
Fig. 7   AE count change monitored in a 200-layers sample of PNNT with aging time. The accelerated aging was performed by a thermal shock treatment
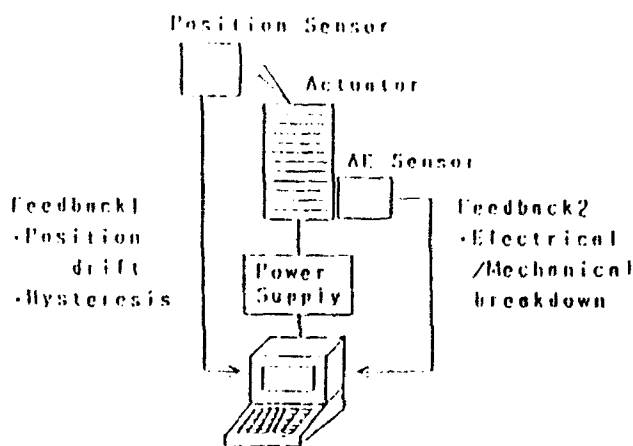
Fig. 8   Very smart actuator system with a reliability test function as well as position sensor.

The AE count change was also monitored for a 200-layers sample of PNNT ($10 \times 10 \times 20$ mm^3) with aging time [4] An accelerated aging test was performed by a rapid-heat treatment up to 100°C in a second. Figure 7 shows that the AE count increases by three orders of magnitude at the final failure of the device in comparison with the virgin state. The monotonous increase of AE may be attributed to successive accumulation of cracks generated in the actuator device.

Summary and Discussions

The crack generation and propagation in multilayer ceramic actuators was observed dynamically during cyclical electric fields. In piezoelectrics, the crack initiated near the edge of the internal electrode and propagated basically in three directions: two cracks moved toward the outside electrostrictively inactive region forming an angle of 100° with each other, while the third moved along the ceramic-electrode interface. This behavior can be explained theoretically based on finite element calculations.[5]

On the contrary, in antiferroelectrics, the crack begins slightly inside the edge of the internal electrode and propagates along the center area between the pair electrodes. Later crack branches are generated around the electrode edge. Theoretical calculations are now in progress.

In both cases the apparent displacement becomes slightly larger than that of the virgin state, and the AE count increases drastically associated with the crack propagation.

Finally we propose a very smart actuator system containing a safety feedback function (Fig. 8), which can stop an actuator drive safely without causing any serious damages on to the work, e.g. in a precision lathe machine. The AE might be one of good predictors for actuator failure. A certain level of the AE count will indicate a timing to replace the ceramic actuator.

References

[1]   K. Uchino, Piezoelectric/Electrostrictive Actuators. Tokyo: Morikita Publ. Co., 1986.

[2]   K. Uchino, "Shape Memory Ceramics," in Proceedings MRS Int'l Mtg. on Advanced Materials, vol. 9, pp. 489, 1989.

[3]   Tokin Technical Catalogue, Multilayer Piezoelectric Actuator Series. Tokin Corp., 1986.

[4]   T. Hirose and K. Uchino, "Acoustic Emission in Ceramic Actuators," Ferroelectrics, vol. 87, pp. 295, 1988.

[5]   S. Takahashi, A. Ochi, . Yonezawa, T. Yano, T. Hamatsuki and I. Fukui, "Internal Electrode Piezoelectric Ceramic Actuator," Jpn. J. Appl. Phys., vol. 22, Suppl. 22-2, pp. 157, 1983.

APPENDIX 31

ELECTRIC FATIGUE INITIATED BY SURFACE CONTAMINATION IN HIGH POLARIZATION CERAMICS

Qiyue Jiang, Wenwu Cao and L. E. Cross
Materials Research Laboratory
The Pennsylvania State University
University Park, PA 16802

ABSTRACT

Recently electric fatigue phenomenon in high polarization ceramics has attracted more and more attention because of the development of high strain actuators and ferroelectric memory devices. We report a study on fatigue behaviors of hot pressed PLZT with composition 7/68/32 under different surface conditions. It is found that the fatigue occurred at a few thousand of cycles is mainly caused by contaminated surface instead of intrinsic structure deterioration. For the same gold electrodes, samples with conventionally cleaned surface showed significant fatigue within 10^5 switching cycles while samples with surfaces cleaned by an improved procedure did not fatigue even after 10^8 switching cycles. The mechanism of fatigue introduced by surface contamination is explained by interface degradation between ceramic and electrode.

INTRODUCTION

Many applications of high polarization ceramics, such as high strain actuators and ferroelectric memory devices, involve repeated reversals of the polarization. One critical limitation on the performances of these devices is the fatigue associated with repeated electrical cycling.

In 1953, McQuarrie [1] first reported the time dependence of the P-E hysteresis loop in a BaTiO$_3$ ceramic. He found that after several weeks of switching at 60 Hz, the square shaped hysteresis loop was changed to a distinct propeller shape with some obvious decrease in both the maximum polarization and the remnant polarization. Merz and Anderson [2] studied fatigue behavior in a single BaTiO$_3$ crystal, a gradual reduction of polarization after a few million switching cycles was observed and the fatigue behavior was related to the patterns of the electric field (sine wave or pulse train wave). The ambient atmosphere was also reported to affect on the switching stability of BaTiO$_3$ single crystal [3]. A more detailed study of fatigue was carried out by Stewart and Cosentino on La or Bi doped PZT ceramics [4], they showed that the polarization decreased rapidly and was reduced to half of its original value after 5×10^6 switching cycles. They concluded that the patterns of electric field, the types of electrodes, and the ambient conditions had no significant effects on the fatigue behavior. Fraser and Maldonado [5] also studied the same La doped PZT ceramics and reported significant effects of the electrodes. They found that when indium was used as electrode material instead of gold or silver, there was still 85% of the original remnant polarization left after 10^9 switching cycles, but fatigue occurred much faster when using lead, aluminum, gallium, silver and gold as electrode material. Carl [6] observed significant degradation in the La or Mn doped PbTiO$_3$ ceramics, after only a few thousand switching cycles the polarization dropped to 30% of its original value together with some increase of the coercive field, and some cracks were also observed on the surfaces of the samples under SEM.

Despite the fact that the fatigue effect is the major factor which prevents some potential applications of ferroelectrics, only a limited number of papers have been published on this subject. In addition, these published results by different investigators are often in contradiction, and there are no satisfactory explanations for these discrepancies. Therefore a systematic study on this subject is needed in order to understand the origin and mechanism of fatigue behavior. We report here the first part of an extensive study of the fatigue behavior on La doped lead zirconate titanate(PLZT) ceramic system. The reason for choosing PLZT ceramic system is because its relatively low coercive field, large polarization and square shaped hysteresis loop. Moreover, hot pressed PLZT ceramics are transparent, therefore have potential applications in non-volatile memory, electro-optical, and electrostrictive devices. In this paper, the focus will be on the effect of surface contamination on the fatigue behavior. We believe that different surface conditions was one of the main reasons for the inconsistencies of those reported experimental results.

EXPERIMENT PROCEDURES

Lanthanum doped lead zirconate titanate ceramic specimens were fabricated from mixed oxides by hot pressing technique. The composition used in this study is Pb$_{0.93}$La$_{0.07}$(Zr$_{0.68}$Ti$_{0.32}$)$_{0.9825}$O$_3$. Conventionally, this formula is simplified to a form 7/68/32 according to the mole ratio of La/Zr/Ti. The average grain size is about 5μm. At room temperature 7/68/32 is in rhombohedral phase. Samples were first cut into platelets with the areas of about 10 mm^2 and thicknesses in the range of 150-300μm, then annealed at 600 °C for 1 hour to release the mechanical stress generated during cutting and grinding processes.

In conventional cleaning procedure, organic solvents (alcohol or acetone) were used to rinse the samples and then the samples were dried in air at room temperature. An improved cleaning method used in our experiments is described as follows: first the samples are cleaned by conventional procedure, then they are further cleaned ultrasonically in solvent, and finally the samples are heated in a furnace for 1 hour at 500-600°C. Gold electrodes were sputtered onto the sample surfaces.

The properties studied here are the remnant polarization P$_r$, the maximum polarization P$_m$, coercive field E$_c$, and the dielectric constant in depoled state. High voltage sine wave AC field was used to switch the polarization, and the hysteresis loops were measured though a conventional Sawyer-Tower circuit and a Nicolet 214 digital oscilloscope.

RESULTS AND DISCUSSION

Fatigue in PLZT Specimens Cleaned by Conventional Procedure

Fig.1 shows a typical result obtained at 10 Hz from a specimen cleaned by conventional procedure. One can see that the fatigue started at about 10^3 switching cycles, and proceeded very rapidly between 10^5 - 10^6 cycles. The polarization P$_r$ dropped to a value below 30% of the initial values after 10^6 switching cycles. The changes of the saturated polarization which was not show here have similar behavior as that of the remnant polarization P$_r$. Fig.2(a) and 2(b) are typical hysteresis loops before and after the fatigue test. The coercive field E$_c$ also increased with switching cycles. We found that the polarization decrease is always accompanied by the increase of the coercive field E$_c$, which is consistent with the results obtained by other researchers [4][5][7]. Measurements made at the frequencies of 100 Hz and 200 Hz did not show apparent difference.

Fatigue in PLZT Specimens Cleaned by Improved Procedure

Fig.3 shows the changes of the polarization and coercive field with switching cycles for samples cleaned by improved procedure. The experiment was carried out at a frequency of 100 Hz. No fatigue was observed even after 10^8 switching cycles. We can see this more clearly from the two hysteresis loops in Fig.4, which were recorded at 10^3 and 2×10^8 switching cycles, respectively. We can conclude from these experimental results that the fatigue shown in Fig.1 is purely extrinsic, i.e., caused by dirty surfaces. The actual lifetime of PLZT 7/68/32 ceramics with average grain size 5 μm is much longer than that shown in Fig.1. For improperly cleaned samples, the organic contaminants are trapped at the ceramic-electrode interfaces. During switching, a large electric field(15-40 kv/cm) was continuously applied on the sample, the trapped contaminates will cause large field concentrations resulting a failure of the electrode bonding.
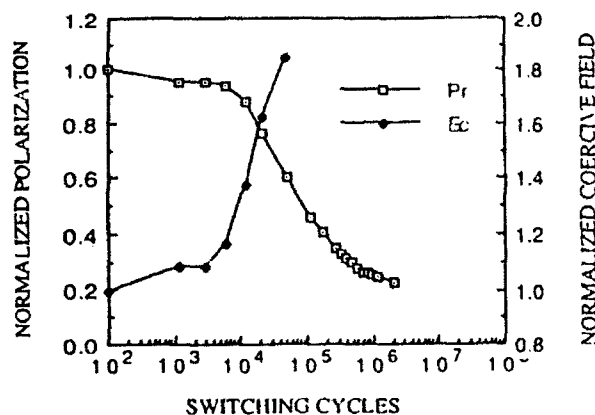
Fig.1 The changes of the normalized remnant polarization P_r and coercive field E_c with switching cycles for a conventionally cleaned PLZT 7/68/32 specimen.
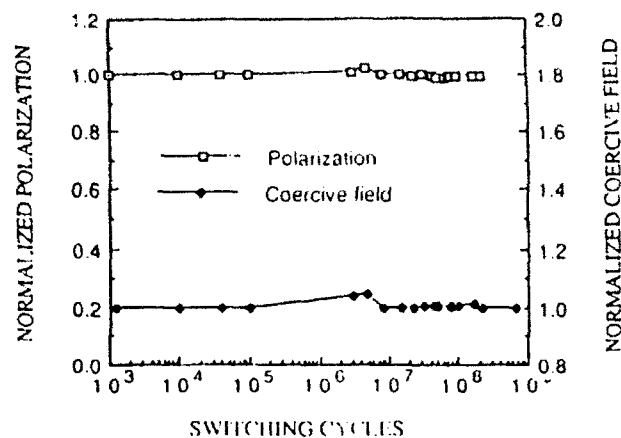

Fig.3 The normalized polarization and coercive field as functions of the switching cycles for a specimen cleaned by the improved procedure.
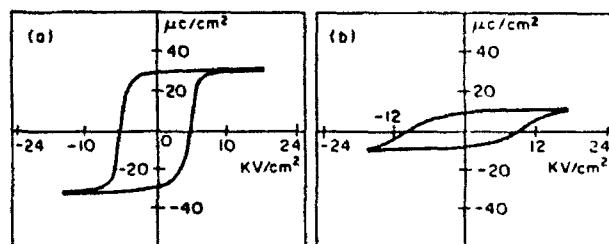

Fig.2 Typical hysteresis loops at 10^3 (a) and 3×10^6 (b) switching cycles for a conventionally cleaned PLZT 7/68/32 sample at a frequency of 10 Hz.
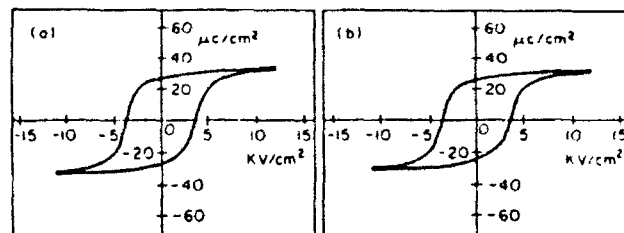

Fig.4 Typical hysteresis loops of a sample cleaned by improved procedure at a frequency of 100 Hz. (a) at 10^3 switching cycles, and (b) at $2*10^8$ cycles.

Although these experimental results may not be used as a proof to discredit the validity of other previous explanations on fatigue in terms of internal domain behavior, we can at least conclude that the fatigue in fine grain hot pressed PLZT 7/68/32 is caused by the improper ceramic-electrode interface, may be eliminated through an improved cleaning procedure described above. This finding is encouraging for many prospective applications of ferroelectrics.

Fatigue Originated from Surface Contamination

A. Deterioration of Ceramic-Electrode Interface under High AC Field

In fatigue experiments the possible sources of contaminants are: abrasive residue from grinding process; residue of solvents(water, alcohol or acetone); water in the air; residue of the bonding glue from cutting process; skin grease from finger touch. Without further cleaning these contaminants are left on the surfaces of specimens, and being sandwiched between the sample surface and the electrode, producing a poor interface contact. The effects of solvents and skin grease were further examined in the following experiments. First, the samples were etched by H_3PO_4 acid to remove the abrasive residues and skin grease, then the following surface treatments were given to three different samples:

a) sample 1 was washed by water and acetone, then rubbed both surfaces by fingers;

b) sample 2 was washed by water and acetone, then let it dry in the air;

c) sample 3 was washed by water and acetone, then heat treated in a furnace at 500 °C for 1 hour (free from contamination).

Fig.5 shows the results from the fatigue tests on these samples using a 100 Hz sine wave AC field. The remnant polarization of sample 3 did not decrease at all after 10^8 switching cycles, only E_c increased slightly. The P_r of sample 2 fatigued to 85% of its initial

value after 10^8 switching cycles and E_c increased about 18%. Sample 1 was the worst among the three samples, its P_r reduced to 30% of the initial value, and E_c increased 50% after only 2×10^6 cycles. Since the three samples only differ in surface treatments, these discrepancies in fatigue results can only be explained in terms of the different degree of surface contamination.

Although the experiments clearly indicate that the fatigue is initialized at the interface between the surface and electrode. The reactions of organic contaminants under high AC field at the interface are very complicated. A few possible explanations for what might have happened at the interface are: [8][9] 1) electrochemical reaction, such as ionization of contaminants, reduction of the chemical composition near the sample surface, 2) corona, high voltage can ionize water and organics, causing partial discharge which leads to a time related continuous degradation of the dielectric property; 3) contact deterioration effect, residue of solvents and skin grease prohibit a direct contact of the metal electrode with the sample surface, resulting a poor contact. When a poor contact occurs, a large field is applied to the contaminant layer which has much smaller dielectric constant than the sample, causing electrochemical reaction, resulting in a partial failure of the contact.

The electrode surface of a fatigued sample (which was cleaned by conventional method) was examined under SEM, and many regions were found where the electrode has been separated from the ceramic as shown in Fig.6. We believe from our experimental observations that the explanation 3) above may be the most appropriate one.

B. The nature of the fatigue by surface contamination

In order to find the nature and degree of damage produced during fatigue, different heat treatments were given to a fatigued sample. Table 1 listed the remnant polarization P_r and the coercive field E_c measured after the fatigued sample went through a heat treatment at 300 °C for 3 hours. Only partial recovery of P_r was

Fig.6 SEM photograph taken from the electroded surface of a fatigued sample.
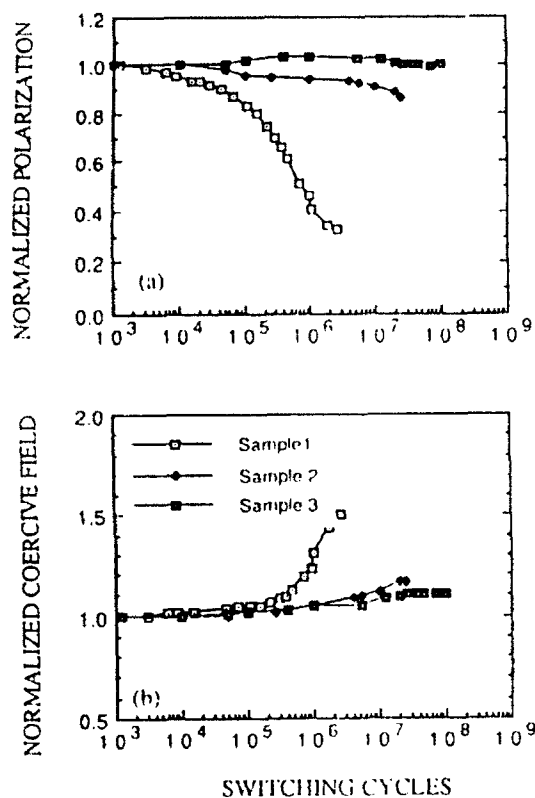
SWITCHING CYCLES

Fig.5 The normalized remnant polarization (a) and coercive field (b) as functions of switching cycles. Sample 1 was contaminated by solvent and skin grease; sample 2 was contaminated by solvent; sample 3 was cleaned by the improved procedure.

Table 4.1 Comparison of the remnant polarization (P_r) and the coercive field (E_c) for a PLZT 7/68/32 sample under different treatments

	P_r ($\mu c/cm^2$)	E_c (kv/cm)
Before fatigue	27.0	5.0
After fatigue	6.0	6.8
After 300°C heating	19.2	10.4
After 600 °C heating	22.4	7.3
After removal of 30μm	22.5	7.2

achieved and E_c became even larger. The sample then experienced further heat treatment at 600 °C for 1 hour, further improvements were observed as shown in Table 1. However, the P_r and E_c still could not recover to their initial values, which means that part of the damage in the fatigued sample is permanent. In order to investigate the depth of the damage from surface initiated fatigue, the sample was then ground off a 15 μm thick layer from each surface and re-electroded. The measured results (table 1) show no further improvement, which indicates that the damage has propagated to the interior of the sample.

Previously, fatigue in ferroelectrics was explained as due to the stabilization of domain walls [1][4][10]. Fatigue caused by domain pinning usually can be recovered by heating the samples to paraelectric phase[4][10]. In our experiments, total recovery did not occur even after the fatigued sample has been heated to as high as 600
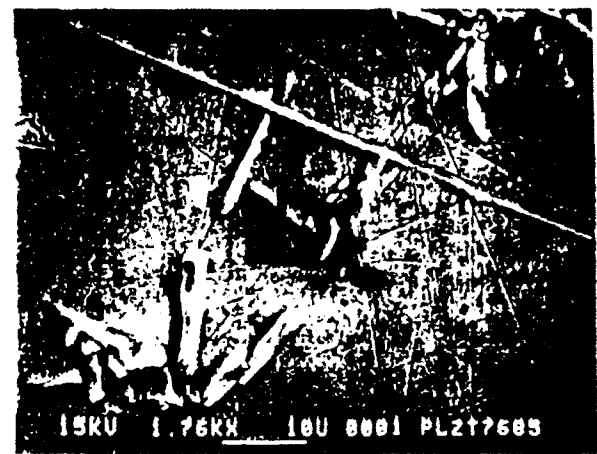
°C which is 470 °C higher than the dielectric maximum temperature. Therefore, the fatigue we have observed could not be due to the domain wall pinning, instead, we believe that the intergranular microcracking is responsible for the non-recoverable fatigue initiated by surface contamination. Scanning Electron Microscopy was performed on a fatigued sample(Fig.7 a) and non-fatigued sample(Fig.7 b) with ground surfaces. The samples were etched using H_3PO_4 acid to remove gold electrodes. On the micrographs in Fig.7, we can see some of the grinding damages and etch-pits for the non-fatigued sample, while for the fatigued sample we see a lot of grains without grinding damages and etch-pits. This means that a whole layer over these grains was pulled out during etching, which indicates that the bonding between grains was weakened during fatigue test. In addition, some cracks around grain boundaries are clearly visible, but no large cracks were observed either on the surfaces or on the cross section of the fatigued sample.

Fig.8 is an optical micrograph which was taken from a fatigued sample after the electrode being carefully removed. Many regions in the original transparent sample become opaque, which indicates that the nonuniform damage in the fatigued sample. This non-uniform damage is due to the partial failure of the electrode caused by the trapped contaminates.

SUMMARY AND CONCLUSIONS

A systematic study has been carried out on the influence of surface conditions on the fatigue behavior of hot pressed PLZT 7/68/32 ceramics with an average grain size of 5μm. It is found that the observed fatigue which occurred within 10^5 switching cycles is actually caused by surface contamination. These surface contaminates cause deterioration of the contact between the ferroelectric ceramic and the electrode, resulting an inhomogeneous field distribution in the specimen. Microcrackings are generated at the grain boundaries due to high electric field concentration. As a result, the applied field then will be concentrated across those cracks parallel to the electrode, which effectively raise the coercive field and lower the polarization. The conventional cleaning method is proved to be inappropriate for specimens used under high AC field. This surface contamination initiated fatigue can be eliminated though an improved surface cleaning procedure. Our results show that the ferroelectric properties of PLZT 7/68/32, such as the polarization and the coercive field, can be preserved for more than 10^8 switching cycles if the surface contaminates are removed.

Contrary to some reported results [4][10]. We found that part of the fatigue damages are permanent and are throughout the entire sample. The fatigued properties i.e., the reduced polarization and the increased coercive field can be partially recovered though heat treatment, however, a complete recovery is not possible.

It should be pointed out that the results obtained here are applicable only for small grain ceramics, the fatigue mechanism in large grain systems is different [11].

109
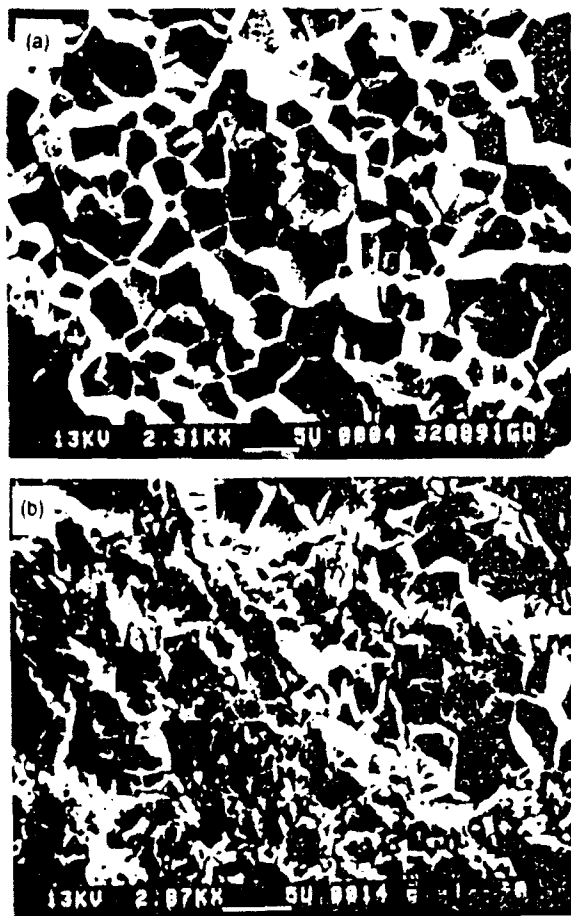
Fig.7 SEM photograph taken from a non-fatigued sample
(a) and fatigued sample (b) after chemical etching.
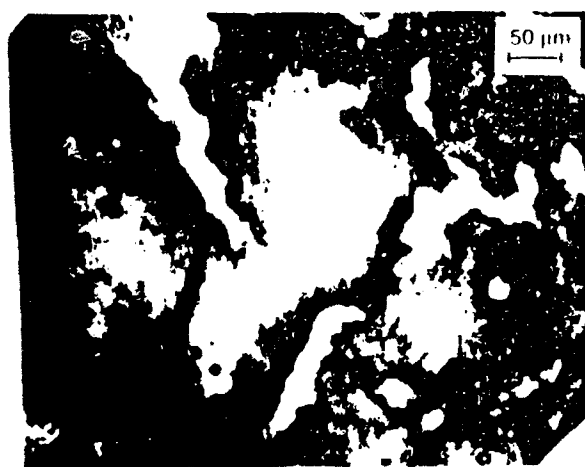
Fig.8 Transmission optical micrograph taken from
a fatigued sample.

REFERENCES

[1] Malcolm McQuarrie "Time Effects in the Hysteresis Loop of Polycrystalline Barium Titanate", J. Appl. Phys., 24, pp. 1334-1335, 1953

[2] W. J. Merz and J. R. Anderson "Ferroelectric Storage Device", Bell Lab. Record, 33, pp. 335-342, 1955

[3] J. R. Anderson, G. W. Brady, W. J. Merz and J. P. Remeika "Effects of Ambient Atmosphere on the Stability of Barium Titanate", J. Appl. Phys., 26, pp. 1387-1388, 1955

[4] W. C. Stewart and L. S. Cosentino "Some Optical and Electrical Switching Characteristics of a Lead Zirconate Titanate Ferroelectric Ceramics", Ferroelectrics, 1, pp. 149-167, 1970

[5] D. B. Fraser and J. R. Maldonado "Improved Aging and Switching of Lead Zirconate-Lead Titanate Ceramics with Indium Electrodes", J. Appl. Phys., 41, pp. 2172-2176, 1970

[6] K. Carl "Ferroelectric Properties and Fatigue Effects of Modified PbTiO$_3$ Ceramics", Ferroelectrics, 9, pp. 23-32, 1975

[7] W. R. Salaneck "Some Fatigue Effects in 8/65/35 PLZT Fine Grained Ferroelectric Ceramics", Ferroelectrics, 4, pp. 97-101, 1972.

[8] Carl J. Tautscher, pp. 4-5 in Contamination Effects on Electronic Products, Marcel Dekker, INC., New York, Basel Hong Kong, 1991.

[9] K. L. Mittal, Morton Antler, "Effect of Surface Contamination on Electric Contact Performance", pp. 179-182 in Treatise on Clean Surface Technology, Vol 1, Edited by K.L.Mittal. Plenum Press, New York and London, 1987.

[10] Ennio Fatuzzio and W. J. Merz, pp. 102-104 in Ferroelectricity, North-Holland Publishing Company, INC New York, 1967.

[11] Hun-Taeg Chung, Byoung-Chul Shin, and Ho-Gi Kim. "Grain Size Dependence of Electrically Induced Microcracking in Ferroelectric Ceramics", J. Am. Ceram. Soc., 72(2), pp. 327-329, 1989.

APPENDIX 32

ELECTRIC FATIGUE IN PLZT CERAMICS

Qiyue Jiang, Wenwu Cao and L.E. Cross

Materials Research Laboratory

The Pennsylvania State University

ABSTRACT

Electric fatigue is a major obstacle for some potential applications of ferroelectric materials based on the reversals of spontaneous polarization, such as memory devices and high strain actuators. Our studies on fine grained hot pressed lead zirconate titanate with lanthanum dopant (PLZT 7/68/32) show that fast fatigue is actually caused by contaminated surfaces instead of intrinsic structure deterioration or the change of domain states. All the specimens with conventionally cleaned surfaces show significant fatigue after 10^5 switching cycles, but specimens cleaned with a new cleaning procedure did not fatigue even after more than 10^8 switching cycles. This type of fatigue is found to be due to generated microcracking at the ceramic-electrode interface.

Key words: Fatigue, Ferroelectric, PLZT, Domain switching, Microcracking.

I. INTRODUCTION

Many applications of ferroelectric materials, such as some piezoelectric, electro-optical and electrostrictive devices, involve repeated reversals of polarization. One critical limitation on the performance of these devices is fatigue associated with repeated electrical cycling. Fatigue in ferroelectrics mainly refers to the degradation of ferroelectric properties upon repeated reversals of polarization, which appears in the hysteresis loop in the form of a decrease in remnant polarization (P_r) or saturated polarization (P_m) and is often accompanied by an increase of the coercive field (E_c).

In 1953, Mcquarrie[1] first reported the time dependence of the P-E hysteresis loop in a $BaTiO_3$ ceramic. He found that after several weeks of switching at 60 Hz, the square shaped hysteresis loop was changed to a distinct propeller shape with a noticeable decrease in both the maximum polarization and the remnant polarization. Merz and Anderson[2] studied fatigue behavior in a $BaTiO_3$ single crystal. A gradual reduction of the polarization after a few million switching cycles was observed and the fatigue behavior was related to the wave patterns of the electric field (sine wave or pulse train wave). The ambient atmosphere was also reported to have an effect on the switching stability of $BaTiO_3$ single crystal.[3] A loss of squareness of the hysteresis loop was observed when the crystal was switched in vacuum, N_2, H_2, or He gases. However, the deteriorated hysteresis loop could restore its original shape under AC cycling in O_2, or in dry air.

Fatigue experiments were also carried out on other ferroelectrics in the 1960's. Taylor[4] studied fatigue phenomena in 24 compositions of niobium-doped $Pb(Zr,Sn,Ti)O_3$ ceramics and discovered that the fatigue rate depended on the composition. Contrary to ref. 2, he found little difference in fatigue behavior when the AC electric field pattern was changed from a sine wave to a pulse train wave. A more detailed study of fatigue in La or Bi doped PZT ceramics was carried out by Stewart and Cosentino.[5] They showed that the polarization decreased rapidly, the remnant polarization was reduced to half of its original value after 5×10^6 switching cycles. They concluded that the patterns of

electric field, the types of electrodes, and the ambient conditions had no significant effects on the fatigue behavior. Stewart and Cosentino[5] also reported an interesting result: when a fatigued sample was heated above the paraelectric-ferroelectric phase transition temperature Tc, the properties could be restored. Contrary to Stewart and Cosentino, Fraser and Maldonado[6] also studied the same La doped PZT ceramics and reported significant effects of electrodes. They found that when indium was used as the electrode material instead of gold or silver, there was still 85% of the original remnant polarization left after 10^9 switching cycles, but fatigue occurred much faster when using lead, aluminum, gallium, silver and gold as electrode materials. Carl[7] observed significant degradation in the La or Mn doped $PbTiO_3$ ceramics, after only a few thousand switching cycles the polarization dropped to 30% of its original value together with some increase of the coercive field, and some cracks were also observed under SEM on surfaces of the samples.

Although the fatigue phenomena in ferroelectrics have been studied for over thirty years, its origin is still not clear. Some possible causes of fatigue under high AC field are: (1) the gradual reorientation of domains into a more stable, i.e. minimum energy configuration;[1] [8] (2) injection of charge carriers into the ferroelectrics which provide pinning for domain wall movement;[9] (3) structural inhomogeneity which produces traps for domain walls, reducing domain wall mobility;[10] (4) the appearance of microcracking caused by the large change of strain during switching.[7][11]

Despite the fact that fatigue effect is the key factor which prevents some potential applications of ferroelectrics, very few conclusive results have been published. In addition, those published results by different investigators are often in contradiction, and there are no explanations for these discrepancies. Therefore, a systematic study on this subject is needed in order to understand the origin and mechanism of fatigue behavior. We report here an extensive study of the fatigue behavior of La doped lead zirconate titanate(PLZT) ceramic system. The reason for choosing PLZT ceramic system is because of its relatively

low coercive field, large polarization and square shaped hysteresis loop. Moreover, hot pressed PLZT ceramics are transparent and are almost pore free, which can eliminate the structural complications in a regular ceramic, leading to some understanding on the fundamental aspects of fatigue. In this paper, the focus will be on the effect of surface contamination on the fatigue behavior. Inconsistencies reported in some previously experimental studies can be explained in terms of different surface conditions.

II. EXPERIMENT PROCEDURES

Lanthanum doped lead zirconate titanate ceramic specimens were fabricated from mixed oxides by hot pressing. The composition used in this study is $Pb_{0.93}La_{0.07}(Zr_{0.68}Ti_{0.32})_{0.9825}O_3$. Conventionally, this formula is simplified to a form 7/68/32 according to the mole ratio of La/Zr/Ti. The average grain size was about 5μm. At room temperature 7/68/32 is in rhombohedral phase. Samples were first cut into platelets with the areas of about 10 mm^2 and thicknesses in the range of 150-300μm, then annealed at 600 °C for 2 hours to release the mechanical stress generated during cutting, grinding and polishing processes.

Three different surface conditions were prepared: a) ground by 3μm abrasive, b) polished by 1μm diamond paste, c) etched in H_3PO_4 acid for 2 minutes at 140°C. In the conventional cleaning procedure, organic solvents (alcohol or acetone) were used to rinse the samples and then the samples were dried in air at room temperature. An improved cleaning method used in our experiments is described as follows: first the samples were cleaned by conventional procedure, then th·⁰ were further cleaned ultrasonically in alcohol solvent, and finally the samples were heated in a furnace for 1 hour at 500-600 °C to burn off the organic solvent. Gold electrodes were sputtered onto the sample surfaces.

The properties studied here are the remnant polarization P_r, the maximum polarization P_m, coercive field E_c, and the dielectric constant ε of depoled state. High voltage sine wave AC field was used to switch the polarization, and the hysteresis loops were measured

through a conventional Sawyer-Tower circuit and a Nicolet 214 digital oscilloscope. The temperature dependence of dielectric constant was measured by Hewlett Pacakard 4274A LRC meter, and the temperature was measured using a Fluke 8502A digital multimeter. The heating rate was set at 3 °C/min.

III. RESULTS AND DISCUSSION

3.1 Fatigue in PLZT Specimens Cleaned by Conventional Procedure.

In order to compare the results from different specimens and to emphasize the changes of the measured properties, relative polarization and coercive field are used in this paper, they represent the percentages of the polarization and coercive field with respect to the initial polarization and coercive field obtained at 10^2 or 10^3 switching cycles. Fig.1 shows the typical results obtained from specimen cleaned by conventional procedure. One can see that fatigue started at about 10^3 switching cycles, and proceeded very rapidly between 10^5 -10^6 cycles. The remnant polarization P_r dropped to 30% of the initial values after 10^6 switching cycles. The changes of the saturated polarizations, which are not shown here, exhibit a similar behavior as the remnant polarization P_r. Fig.2 shows typical hysteresis loops before and after the fatigue test, observed from a sample with ground surfaces. The coercive fields E_c also increased with switching cycles. There is a direct correlation between the changes of E_c and P_r, i.e., while the polarization decreases, the coercive field E_c increases, which is consistent with the results obtained by other researchers.[4][6][11] We found that the ground sample fatigued earlier and faster than the samples with polished and etched surfaces. The same experiments were also carried out using sine wave field at other frequencies, no apparent changes were observed for frequencies less than 600 Hz. Curves (a) and (e) in Fig.3 are the weak field dielectric constant as a function of temperature for a sample with polished surfaces before and after the fatigue test respectively. One can see a substantial decrease of the dielectric constant in

the fatigued sample. Samples with the other two types of surfaces exhibit similar results which are not shown here.

3.2 Fatigue in PLZT Specimens Cleaned by Improved Procedure.

Fig.4 shows the changes in the polarization and coercive field with switching cycles for samples cleaned by improved procedure described in Section II. The experiments were carried out at a frequency of 100 Hz. Samples with all the three types of surfaces did not show fatigue even after 10^8 switching cycles. We found that the hysteresis loops recorded at 10^3 and 2×10^8 switching cycles are almost identical. These experimental results tell us that the fatigue shown in Fig.1 is purely extrinsic, i.e., resulted from improper cleaning method. The actual lifetime of PLZT 7/68/32 ceramics with grain size of 5 μm is much longer than that shown in Fig.1 and are not affected by the surface roughness.

3.3 Fatigue Originated from Surface Contamination.

A. Deterioration of the ferroelectric-electrode interface under high AC field

In fatigue experiments the possible sources of contaminants are: abrasive residue from grinding process; residue of solvents(water, alcohol or acetone); water in the air; residue of the bonding glue; skin grease from finger touch. Without further cleaning these residues are left on the surfaces of specimens, being sandwiched between the sample surface and the electrode, producing a poor interface contact. The effects of solvents and skin grease were further examined in the following experiments. First, the samples were etched by H_3PO_4 acid to remove a thin layer from the surface which might contain abrasive residue and skin grease. Then the following surface treatments were given to three different samples:

a) sample 1 was washed in water and acetone, then both surfaces were rubbed with fingers;

b) sample 2 was washed in water and acetone, then dried in air at room temperature;

c) sample 3 was washed in water and acetone, then heat treated in a furnace at 500 °C for 1 hour.

Fig.5 shows the results from fatigue tests on these three samples using a 100 Hz sine wave AC field. The remnant polarization of sample 3 did not decrease at all after 10^8 switching cycles, only E_c increased slightly (we note that in all etched samples, E_c shows a slight increase at the beginning and then becomes stable.). P_r of sample 2 fatigued to 85% of its initial value after 10^7 switching cycles and E_c increased about 18%. Sample 1 was the worst among the three samples; its P_r reduced to 30% of the initial value and E_c increased 50% after only 2 x10^6 cycles. Heating PLZT ceramic samples to 500 °C after washing have two effects: (1) burn off the organics residues on the surface, and (2) release bulk and surface stresses. Since these three samples were already heat treated at 600 °C for 2 hours to release stresses before the surface preparation described above, heating sample 3 to 500 °C for 1 hour after washing should not change its properties except burning off solvent residues on the sample surfaces. Since the three samples with the same etched surfaces differ only in surface treatments, the discrepancies in fatigue results could only be explained in terms of the different degree of surface contamination.

Experiments also indicate that the fatigue is initiated at the ceramic-electrode interface. Possible explanations for what might have happened at the interface are:[12][13] (1) electrochemical reaction, such as ionization of contaminants and field induced chemical decomposition near the sample surface; (2) corona, high voltage can ionize water and organics, causing partial discharge which leads to a time related continuous degradation of the dielectric property; (3) contact deterioration effect, residue of solvents and skin grease prohibit a direct contact of the metal electrode with the sample surface, resulting in a poor contact. Partial failure of the electrode were directly observed under SEM on the electroded surface of fatigued samples as shown in Fig.6.

B. The nature of the fatigue

Fatigue caused by surface contamination started at the sample surfaces where high field concentrations occur. In order to see if the fatigue damage has extended into the interior of the ceramic with a prolonged switching time, we have measured the bulk dielectric constant as a function of temperature. The sample thickness is 200 μm and the measurements were done at 1 kHz frequency. The maximum temperature in the measurement was 190 °C which is above the Curie temperature (130 °C for PLZT 7/68/32). The results are given in Fig.3. One can see a drastic decrease of the dielectric constant in the fatigued sample (after 2×10^6 cycles), especially close to the Curie temperature region [curve (a) in Fig.3].

Different heat treatments were applied to this fatigued sample to see if the fatigued physical properties could be recovered. Curve (b) in Fig.3 is the temperature dependence of the dielectric constant measured after the fatigued sample went through a heat treatment at 300 °C for 3 hours. Only partial recovery was achieved. The sample then experienced further heat treatment at 600 °C for 1 hour and further improvement was observed as shown in curve (c) of Fig.3. However, the dielectric constant still did not recover to its initial value, which means that part of the damage is permanent. In order to investigate the depth of the damage from surface initiated fatigue, 15 μm at the sample surfaces was ground off and the sample was re-electroded using the sputtering technique. The measured results are shown in Fig.3 curve (d). No further improvement was achieved. The high field properties, i.e., the remnant polarization P_r and the coercive field E_c, were also measured after each heating, re-electroding, and thinning (Table I). One can reach the same conclusion from the results in Table I as from the results of weak field dielectric measurements. The dielectric and polarization measurements were also performed in a sample with a thickness of 700 μm, fatigue was observed after 2×10^6 cycles. However, it is found that the dielectric constant and the polarization can almost restore to its initial value after 150 μm layer were ground off from the sample surfaces. The experimental results

indicate that fatigue damage had propagated fairly deep into the interior of the sample after more than 10^6 swiching cycles (note the damage was only at the surface within 10^5 cycles).

Previously, fatigue in ferroelectrics was explained as due to the stabilization of domain walls,[1][5][8] which can be recovered by heating the fatigued sample into the paraelectric phase.[5][8] In our experiments, total recovery did not occur even after the fatigued sample being heated to as high as 600 °C, 470 °C higher than the Curie temperature. Hence, the fatigue we have observed can not be due to domain wall pinning; instead, we believe that intergranular microcracking is responsible for the non-recoverable fatigue initiated by surface contamination. Scanning Electron Microscopy was performed on a fatigued sample (Fig.7 a) and non-fatigued sample (Fig.7 b) with ground surfaces (the samples were etched using H_3PO_4 acid to remove gold electrodes). On the micrographs in Fig.7 (b), we can see some grinding damage and etch-pits for the non-fatigued sample, while for the fatigued sample (Fig. 7a) the majority of the grains do not have grinding damage or etch-pits. This means that a whole layer over these grains was pulled off during etching, which indicates that the bonding between grains was weakened in the fatigued sample near the surface. In addition, some minor cracks around grain boundaries were visible in Fig.7 (a), but large cracks were neither observed on the surfaces nor on the cross section of the fatigued sample.

Because ferroelectrics are both piezoelectric and electrostrictive, large strain can be generated during switching. In PLZT ceramics the field induced strain can be as large as 0.1% or more.[14] When the deterioration of the interface occurs during the fatigue experiment, the regions under good contact electrode are under larger field, while the regions under deteriorated interface effectively experience much smaller field. Hence, these two regions can not be switched simultaneously under a constant voltage across the two electrodes. This generates stress concentrations at the boundaries between the switched regions and the non-switched regions. If the grain boundaries have weaker mechanical strength than that of the grains, intergranular microcracking could be produced by these

stress concentrations. An optical micrograph of a fatigued sample shows that this is indeed the case (see Fig.8). The micrograph was taken from a fatigued sample under a transmitted light after the electrodes were carefully removed. It was found that some of the regions were changed from transparent to opaque, but some regions still remain transparent. The degree of opacity represents the degree of mechanical damage in the sample. In general, the worse the fatigue the less the total area of the transparent regions.

IV. SUMMARY AND CONCLUSIONS

A systematic study has been carried out to determine the influence of surface conditions on the fatigue behavior of hot pressed PLZT 7/68/32 ceramics with grain size of $5\mu m$. It is found that the observed fatigue occurred within 10^5 switching cycles is caused by surface contamination. We suggest that the fatigue initiated by surface contamination in hot pressed PLZT 7/68/32 ceramics is though microcracking at the boundaries of the switched and non-switched regions near the ceramic-electrode interface, which progressively extends into the interior of the ceramic with prolonged switching.

The conventional cleaning method is proved to be inappropriate for specimens used under high AC field. An improved cleaning procedure described here can eliminate fatigue for at least 10^8 switching cycles, which is a very encouraging result for some potential applications based on the polarization reversals.

Contrary to some reported results,[5][8] we found that the fatigue damage is permanent although it is only limited at the surface region at the beginning. Some physical properties of the fatigued sample can be partially recovered though thermal treatment, however, complete recovery is not possible.

ACKNOWLEDGEMENT

REFERENCES

1. Malcolm McQuarrie. "Time Effects in the Hysteresis Loop of Polycrystalline Barium Titanate", J. Appl. Phys., **24**, 1334-1335 (1953).

2. W. J. Merz and J. R. Anderson. "Ferroelectric Storage Device", Bell Lab. Record, **33**, 335-342(1955).

3. J. R. Anderson, G. W. Brady, W. J. Merz and J. P. Remeika. "Effects of Ambient Atmosphere on the Stability of Barium Titanate", J. Appl. Phys., **26**, 1387-1388 (1955).

4. G. W. Taylor. "Electric Properties of Niobium-doped Ferroelectric $Pb(Zr,Sn,Ti)O_3$ Ceramics", J. Appl. Phys., **38**, 4697-4706(1967).

5 W. C. Stewart and L. S. Cosentino. "Some Optical and Electrical Switching Characteristics of a Lead Zirconate Titanate Ferroelectric Ceramics", Ferroelectrics, **1**, 149-167(1970).

6. D. B. Fraser and J. R. Maldonado. "Improved Aging and Switching of Lead Zircanate-lead Titanate Ceramics with Indium Electrodes", J. Appl. Phys., **41**, 2172-2176(1970).

7. K. Carl. "Ferroelectric Properties and Fatigue Effects of Modified $PbTiO_3$ Ceramics", Ferroelectrics, **9**, 23-32(1975).

8. Ennio Fatuzzio and W. J. Merz, pp102-104 in Ferroelectricity, North-Holland Publishing Company, INC New York, 1967.

9. Richard Williams. "Surface Layer and Decay of the Switching Properties of Barium Titanate", J. Phys. Chem. Solids, **26**, 399-405(1965).

10. A. Yu. Kudzin and T. V. Panchenko. "Stabilization of Spontaneous Polarization of $BaTiO_3$ Single Crystals", Sov. Phys. Sol. State, **14**, 1599-1600(1972).

11. W. R. Salaneck. "Some Fatigue Effects in 8/65/35 PLZT Fine Grained Ferroelectric Ceramics", Ferroelectrics, **4**, 97-101(1972).

12. Carl J. Tautscher, pp4-5 in Contamination Effects on Electronic Products, Marcel Dekker, INC., New York. Basel. Hong Kong, 1991.

13. K. L. Mittal, Morton Antler," Effect of Surface Contamination on Electric Contact Performance"; pp179-182 in Treatise on Clean Surface Technology, Vol 1, Edited by K.L.Mittal. Plenum Press, New York and London, 1987.

14. W. Y. Pan, Q. M. Zhang, Q.Y. Jiang And L. E. Cross. "Electric Field Induced Strain in $(Pb,La)(Zr,Ti)O_3$ Ferroelectric Ceramics under the Tetragonal-Rhombohedral Morphotropic Phase Boundary", Ferroelectrics, **88**, 1-15(1988).

Figure Captions

Fig.1 (a) and (b) are the changes of the relative remnant polarization P_r and the relative coercive field E_c respectively with switching cycles for a conventionally cleaned PLZT 7/68/32 specimen. Test frequency is 10 Hz .

Fig.2 The typical hysteresis loops after 10^3 (a) and 3×10^6 (b) switching cycles for a conventionally cleaned PLZT 7/68/32 sample with ground surfaces. Test frequency is 10 Hz.

Fig.3 Temperature dependence of the dielectric constant in depoled state for a conventionally cleaned sample with polished surfaces. (a) Fatigued sample; (b) fatigued sample after heat treatment at 300 °C for 3 hours. (c) fatigued sample after heat treatment at 600 °C for 1 hour. (d) a 15 µm thick layer was ground off from each side of the sample. (e) results from a virgin non-fatigued sample.

Fig.4 (a) and (b) are the relative polarization and the relative coercive field versus switching cycles, respectively, for a specimen cleaned by improved procedure. Test frequency is 100 Hz.

Fig.5 Effects of contaminations on the fatigue behavior. Sample 1 was contaminated by solvent and skin grease; sample 2 was contaminated by solvent; sample 3 was cleaned by improved procedure.

Fig.6 SEM photograph taken from the electroded surface of a fatigued sample. Part of the electrode was peeled off from the sample surface during switching process.

Fig.7 SEM micrograph taken from a fatigued sample (a) and a non-fatigued sample (b) after chemical etching. Etch-pits were not found on the surface of the fatiqued sample because a loosened layer was etched off.

Fig.8 Optical micrograph taken from a fatigued sample with transmission light. The opacity indicates the degree of mechanical damage or stress concentrations. The transparent regions are non-fatigued portions left in the sample.

Table I. Comparison of the remnant polarization and the coercive field
for a PLZT 7/68/32 sample under different treatments

	Remnant Polarization ($\mu c/cm^2$)	Coercive Field (kv/cm)
Before fatigue	27.0	5.0
After fatigue	6.0	6.8
After 190 °C heating	11.5	8.0
After 300°C heating	19.2	10.4
After 600 °C heating	22.4	7.3
After removal of 15μm from each side	22.5	7.2

INTEGRATION ISSUES

APPENDIX 33

Theoretical study on the static performance of piezoelectric ceramic-polymer composites with 1-3 connectivity

Wenwu Cao, Q. M. Zhang, and L. E. Cross

Materials Research Laboratory, The Pennsylvania State University, University Park, Pennsylvania 16802

Inhomogeneous displacement profiles have been derived for a single-rod composite and a single-tube 1-3 ceramic-polymer composite under both uniaxial and hydrostatic stress. The effective piezoelectric constants for the composites have been derived in terms of the ceramic content, the piezoelectric and elastic constants of each component, and the aspect ratio of the ceramic rod. The stress concentration inside both phases is derived from the calculated inhomogeneous displacement profiles. It is found that only a finite portion of the polymer in the vicinity of the ceramic-polymer interface actually contributes to the stress transfer, and the induced additional stress on the ceramic also has a higher magnitude near the interface. The theoretical results quantitatively predict the performance of a given 1-3 structure, and can be used to optimize the design parameters, such as ceramic content, aspect ratio of the ceramic rods, rod geometry and rod arrangement, resin hardness, etc., for 1-3 structures designed for specific purposes.

I. INTRODUCTION

With the increasing application of piezoelectric composite structures, quantitative description of their physical properties has become a necessity for proper structural design. The most frequently encountered piezocomposites are 2-2- and 1-3-type ceramic-polymer composites. The names of these composites are defined according to their connectivities.[1] In the past, theoretical studies on this subject have been limited to the isostrain models.[2-4] Although the isostrain models can provide some general guidelines, their theoretical predictions are often larger than the experimental values.[5] In addition, the effect of the aspect ratio, which is proven experimentally to be a critical parameter in the 1-3 composite structure, is not included in the isostrain models. After analyzing the essential characteristics of the problem we have presented in a previous paper a theoretical model for the 2-2 composites.[6] This model can quantitatively describe the effective piezoelectric properties of the 2-2-type composites. In this paper we extend the model to address the 1-3-type composites which are more attractive and have much wider applications than the 2-2 structures from a practical point of view.

The fundamental physics in the 1-3 composites is the same as that in the 2-2-type composites. We expect the displacement profile in a 1-3 composite to be inhomogeneous under a prescribed stress field or an electric field because the two components have different elastic and piezoelectric properties. The difference between the 2-2 and 1-3 problems is the dimensionality, i.e., one-dimensional for the 2-2 type and two dimensional for the 1-3 type. Besides the dimensionality difference, there are two more complications in the 1-3-type composites: one is the geometry of the cross section of the ceramic rod, which is commonly chosen to be square or circular due to manufacturing convenience; the other is the rod arrangement in the composite, which usually is made into square or triangular configurations. Because the rod geometry and the rod arrangement define the boundary conditions for the problem, each case must be treated separately. Here we only solve two simple cases for which analytic solutions exist; using these two examples we wish to derive the essential features of the 1-3 structure and demonstrate the general procedure for dealing with the 1-3 composites. Solutions for an arbitrary rod geometry and rod arrangement may be calculated numerically.

The two cases to be treated are composites made of a single cylindrical ceramic rod and a single ceramic cylinder with a polymer matrix of finite dimension as shown in Figs. 1 and 2, respectively. One can think of them as the "unit cells" of a 1-3 composite. For simplicity, the outer boundary of the composite is also defined to be circular. Obviously, such a unit cell cannot be used to fill the whole space. However, it is a reasonable approximation to the composite with triangularly arranged ceramic rods (for which the unit cell has hexagonal symmetry) and, as will be proven later, at low ceramic content the results for the single-rod composite can even be used for composites with other rod arrangements.

II. DISPLACEMENT PROFILE IN A SINGLE-ROD COMPOSITE UNDER UNIAXIAL AND HYDROSTATIC STRESSES

The basic idea for constructing the static equilibrium condition is to single out the effective component of the displacement field. For the single-rod (tube) system as shown in Fig. 1 (Fig. 2), we choose a cylindrical coordinate system (r, ϕ, z) with the z and r directions along the axis of the ceramic rod (tube) and the radial direction, respectively, and ϕ as the angular variable. When the ce-
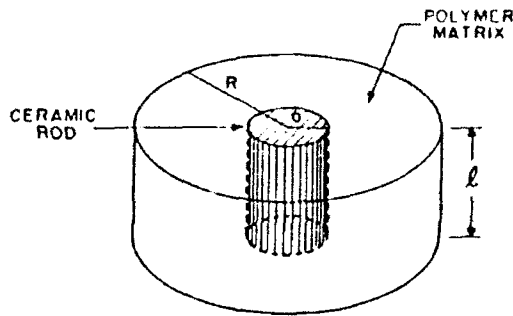
FIG. 1. A single ceramic rod composite of length l. The radius of the composite is R and a is the radius of the ceramic rod.

ramic rods are poled in the axial direction (the z direction in our calculations), the stress transfer in the 1-3 structure only enhances the piezoelectric response of the ceramic rods in the z direction. Therefore, to a good approximation, we only need to derive the z component of the displacement field. Following the procedure described in Ref. 6, we use the ansatz $u(r,z) = (2z/l)u(r,l/2)$, for the z component of the displacement field; then, under a uniaxial stress T_3 the static equilibrium condition for the polymer and ceramic phases can be written in the following form in a cylindrical coordinate system:

$$\frac{\mu^p l}{4}\left(\frac{\partial^2 u(r,l/2)}{\partial r^2}+\frac{1}{r}\frac{\partial u(r,l/2)}{\partial r}+\frac{1}{r^2}\frac{\partial^2 u(r,l/2)}{\partial \phi^2}\right)$$

$$=\frac{2Y^p}{l}u(r,l/2)-T_3, \quad r>a, \tag{1a}$$

$$\frac{c_{44}l}{4}\left(\frac{\partial^2 v(r,l/2)}{\partial r^2}+\frac{1}{r}\frac{\partial v(r,l/2)}{\partial r}+\frac{1}{r^2}\frac{\partial^2 v(r,l/2)}{\partial \phi^2}\right)$$

$$=\frac{2}{ls_{33}}v(r,l/2)-T_3, \quad r<a, \tag{1b}$$

where $u(r,l/2)$ and $v(r,l/2)$ are the z components of the displacement for the polymer and the ceramic, respectively, at the top surface of the composite. μ^p and Y^p denote the shear and Young's moduli of the polymer phase, and
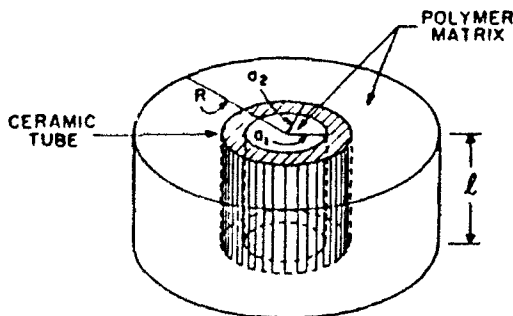

FIG. 2. A single ceramic tube composite of length l. The radius of the composite is R, while a_1 and a_2 are the inner and outer radii of the ceramic tube.

c_{44} and s_{33} are the shear elastic stiffness and the normal elastic compliance of the ceramic, respectively.

Considering the composite shown in Fig. 1, the solution must be independent of ϕ because of the symmetry, which means that the second derivative with respect to ϕ vanishes. By making the following substitution

$$\bar{u}=u(r,l/2)-(lT_3/2Y^p), \tag{2a}$$

$$\rho=r/\xi^p, \quad \xi^p=(l/2)\sqrt{\mu^p/2Y^p}, \tag{2b}$$

Eq. (1a) can be recast to the following zeroth-order Bessel equation of imaginary argument:

$$\rho^2\frac{\partial^2\bar{u}}{\partial\rho^2}+\rho\frac{\partial\bar{u}}{\partial\rho}-\rho^2\bar{u}=0. \tag{3}$$

Standard solutions exist for Eq. (3) so that the surface displacement of the polymer phase, $u(r,l/2)$, can be obtained using Eqs. (2a) and (2b),

$$u\left(r,\frac{l}{2}\right)=AK_0\left(\frac{r}{\xi^p}\right)+BI_0\left(\frac{r}{\xi^p}\right)+\frac{l}{2Y^p}T_3 \quad (r>a) \tag{4}$$

where $K_0(\rho)$ and $I_0(\rho)$ are the zeroth-order modified Bessel functions, and A and B are the constants of integration.

Similarly we can obtain the surface displacement profile for the ceramic rod by solving Eq. (1b) using the same technique,

$$v(r,l/2)=CI_0(r/\xi^c)+(1/2)s_{33}T_3 \quad (r<a), \tag{5}$$

where $\xi^c=1/2\sqrt{s_{33}c_{44}/2}$. Note that in Eq. (5) we have used the boundary condition that $v(r,l/2)$ is finite at $r=0$, so that only one integration constant C remains.

In order to determine the integration constants in the solutions Eqs. (4) and (5), three boundary conditions are needed. The first one can be obtained from the nonslip interface condition at $r=a$, viz.

$$u(a,l/2)=v(a,l/2). \tag{6}$$

The second one is the free-boundary condition at $r=R$ for the polymer phase,

$$\left.\frac{\partial u(r,l/2)}{\partial r}\right|_{r=R}=0 \tag{7}$$

[the derivative of $u(r,z)$ along the direction normal to the unit-cell boundary must always vanish in the composite structure due to symmetry]. For the single-rod composite in Fig. 1 we can use Newton's third law to derive the other condition needed to determine the constants as described

TABLE I. Elastic, piezoelectric, and dielectric constants of PZT5H[a] and epoxy[b] used in our calculations. ϵ_0 is the dielectric constant of vacuum.

PZT5H: $s_{11}=0.0208$ (10^{-9} m²/N), $c_{44}=20.0$ (10^9 N/m²), $\sigma^c=0.31$, $d_{33}=593$ (10^{-12} C/N), $d_{31}=-274$ (10^{-12} C/N), $\epsilon^c=3400\epsilon_0$
Epoxy: $Y^p=3.1$ (10^9 N/m²), $\mu^p=1.148$ (10^9 N/m²), $\sigma=0.35$, $\epsilon^p=3.5\epsilon_0$

[a]See Ref. 7.
[b]See Ref. 8.

in Ref. 6, but for later convenience, we use the following equivalent but more general boundary condition:

$$\mu^p \frac{\partial u(r,l/2)}{\partial r}\bigg|_{r=a} = c_{44} \frac{\partial v(r,l/2)}{\partial r}\bigg|_{r=a}. \tag{8}$$

Equation (8) states that the shear stress is a continuous function of r across the interface in the nonslip interface composite structures.

Now the three integration constants A, B, and C can be determined from Eqs. (6), (7), and (8); they are

$$A = \frac{-(1/2)I_1(\rho_R^p)I_1(\rho_a^c)(1/Y^p - s_{33})T_3}{\sqrt{(Y^p s_{33}\mu^p/c_{44})}I_0(\rho_a^c)[I_1(\rho_R^p)K_1(\rho_a^p) - I_1(\rho_a^p)K_1(\rho_R^p)] + I_1(\rho_a^c)[I_1(\rho_R^p)K_0(\rho_a^p) + K_1(\rho_R^p)I_0(\rho_a^p)]}, \tag{9a}$$

$$B = \frac{(1/2)K_1(\rho_R^p)I_1(\rho_a^c)(1/Y^p - s_{33})T_3}{\sqrt{(Y^p s_{33}\mu^p/c_{44})}I_0(\rho_a^c)[I_1(\rho_R^p)K_1(\rho_a^p) - I_1(\rho_a^p)K_1(\rho_R^p)] + I_1(\rho_a^c)[I_1(\rho_R^p)K_0(\rho_a^p) + K_1(\rho_R^p)I_0(\rho_a^p)]}, \tag{9b}$$

$$C = \frac{(1/2)[I_1(\rho_R^p)K_1(\rho_a^p) - I_1(\rho_a^p)K_1(\rho_R^p)](1/Y^p - s_{33})T_3}{I_0(\rho_a^c)[I_1(\rho_R^p)K_1(\rho_a^p) - I_1(\rho_a^p)K_1(\rho_R^p)] + \sqrt{(c_{44}/Y^p s_{33}\mu^p)}I_1(\rho_a^c)[I_1(\rho_R^p)K_0(\rho_a^p) + K_1(\rho_R^p)I_0(\rho_a^p)]}, \tag{9c}$$

where

$$\rho_a^p = a/\xi^p, \quad \rho_R^p = R/\xi^p, \quad \rho_a^c = a/\xi^c,$$

and $K_0(\rho)$, $I_0(\rho)$, $K_1(\rho)$, and $I_1(\rho)$ are the zeroth- and first-order modified Bessel functions.

Because of the coupling between the two components at the interface in the 1-3 structure, the total effective stress on the ceramic becomes larger but inhomogeneous. The magnitude of the effective total stress is the largest at the interface and becomes smaller away from the interface. The effective induced electric displacement in the ceramic now becomes

$$D(r) = d_{33}T_3^{\text{eff}} = \frac{d_{33}}{s_{33}}\frac{v(r,l/2)}{l/2}, \quad r < a. \tag{10}$$

From Eq. (10) we can calculate the total bound charge Q produced at the top surface of the ceramic rod,

$$Q = 2\pi \int_0^a D(r)r\,dr = \gamma d_{33}T_{33}\pi a^2, \tag{11}$$

where

$$\gamma = 1 + \frac{(l/a)I_1(\rho_a^c)[I_1(\rho_R^p)K_1(\rho_a^p) - I_1(\rho_a^p)K_1(\rho_R^p)](1/Y^p - s_{33})}{\sqrt{(2s_{33}/c_{44})}I_0(\rho_a^c)[I_1(\rho_R^p)K_1(\rho_a^p) - I_1(\rho_a^p)K_1(\rho_R^p)] + \sqrt{(2/Y^p\mu^p)}I_1(\rho_a^c)[I_1(\rho_R^p)K_0(\rho_a^p) + K_1(\rho_R^p)I_0(\rho_a^p)]} \tag{12}$$

is the stress amplification factor.

We can see that the amplification factor depends on the elastic properties of both phases, the ceramic content $V_c = a^2/R^2$, and more important, the aspect ratio a/l. In order to visualize this aspect ratio dependence, we have calculated the numerical values of Eq. (12) for a PZT5H-epoxy composite using the input data in Table I. (PZT5H is a trademark of Vernitron Corp. for its lanthanum-doped PZT product.) The results are shown in Fig. 3. Two important conclusions can be drawn from the results in Fig. 3 as follows.

(i) There is a saturation value for the enhancement effect for any given aspect ratio a/l. This is because the stress transfer effect is limited only to the portion near the ceramic-polymer interface; in other words, only the polymer portion near the interface actually contributes to the enhancement effect. This point will be elaborated below. This saturation value of γ can be derived from Eq. (12) by taking the limit $R \to \infty$,

$$\lim_{R\to\infty}\gamma = 1 + \frac{(l/a)K_1(\rho_a^p)I_1(\rho_a^c)(1/Y^p - s_{33})}{\sqrt{(2s_{33}/c_{44})}I_0(\rho_a^c)K_1(\rho_a^p) + \sqrt{(2/Y^p\mu^p)}I_1(\rho_a^c)K_0(\rho_a^p)}. \tag{13}$$

This limiting value depends very strongly on the aspect ratio of the ceramic rod a/l, which may be visualized from the results shown in Fig. 3 at $V_c = 0$; it decreases rapidly with the increase of the ratio a/l. The inclusion of the aspect ratio is one of the novel features of the current model.

(ii) The γ value obtained from the current model is always smaller than the isostrain result but larger than the two-phase decoupling result ($\gamma = 1$, which can be obtained by taking the limit $a \to \infty$ for a finite l), depending on the aspect ratio a/l of the structure. In general, for a fixed ceramic content, thin and long rods should be used in order to get larger γ. The isostrain models actually give the upper limit for the enhancement factor, which can be derived from Eq. (12) for a finite R by taking the limit $l \to \infty$,

$$\lim_{l \to \infty} \gamma = \frac{1}{V_c + V_p Y^p s_{33}} , \qquad (14)$$

where V_c and V_p are the volume fractions of the ceramic and polymer respectively. Equation (14) is just the isostrain result.[9]

In order to see how the stress transfer actually takes place, the generated additional stress T_{add} inside both the ceramic and the polymer phases for a single-rod composite

is calculated using the parameters from Table I. For clarity and simplicity, we assume $R \to \infty$ (corresponding to $V_c \to 0$); then the solutions for the z component of the displacement field inside the composite become

$$u(r,z) = \frac{z}{l/2}\left(A K_0(\rho^r) + \frac{l/2}{Y^p} T_3\right), \quad r > a, \qquad (15a)$$

$$v(r,z) = \frac{z}{l/2}\left(C I_0(\rho^c) + \frac{l}{2} s_{33} T_3\right), \quad r < a, \qquad (15b)$$

where

$$A = \frac{(l/2) I_1(\rho_a^c)(s_{33} - 1/Y^p) T_3}{\sqrt{(Y^T s_{33}\mu^p/c_{44})} I_0(\rho_a^c) K_1(\rho_a^p) + I_1(\rho_a^c) K_0(\rho_a^p)} , \qquad (16a)$$

$$C = \frac{(l/2) K_1(\rho_a^p)(1/Y^p - s_{33}) T_3}{I_0(\rho_a^c) K_1(\rho_a^p) + \sqrt{(c_{44}/Y^T s_{33}\mu^p)} I_1(\rho_a^c) K_0(\rho_a^p)} . \qquad (16b)$$

In this case the generated additional stress T_{add} is

$$T_{add} = T_3^{eff} - T_3 = \begin{cases} \dfrac{I_1(\rho_a^c)(s_{33} Y^p - 1) T_3 K_0(\rho^p)}{\sqrt{(Y^T s_{33}\mu^p/c_{44})} I_0(\rho_a^c) K_1(\rho_a^p) + I_1(\rho_a^c) K_0(\rho_a^p)} , \quad r > a, & (17a) \\[3ex] \dfrac{K_1(\rho_a^p)(1/Y^p s_{33} - 1) T_3 I_0(\rho^c)}{I_0(\rho_a^c) K_1(\rho_a^p) + \sqrt{(c_{44}/Y^p s_{33}\mu^p)} I_1(\rho_a^c) K_0(\rho_a^p)} , \quad r < a. & (17b) \end{cases}$$

T_{add} is plotted in Fig. 4 for a single-rod PZT5H-epoxy composite with $a = 0.5$, $l = 2.5$ and 5, respectively. We can see that T_{add} has opposite signs in the ceramic ($r < 0.5$) and in the polymer ($r > 0.5$), and the magnitude is the largest at the interface. There is a substantial increase of the effective stress in the ceramic at the expense of the stress reduction in the polymer phase. Because of the difference between the elastic properties in the two phases, T_{add} subsides very fast away from the interface in the polymer but changes relatively slowly in the ceramic phase. Also, we note in Fig. 4 that T_{add} depends very strongly on

the ratio a/l. With the increase of l, more polymer will participate in the stress transfer process. Although the maximum stress magnitude at the interface $a = 0.5$ becomes slightly smaller, the total force transferred to the ceramic rod, which is the product of the stress and the surface area of the participating polymer, becomes larger. We found that the inhomogeneity of the additional stress becomes stronger as the a/l ratio increases.

It is clear from the stress analysis that the most effective portion of the 1-3 structure is near the ceramic-polymer interface, especially for relatively large a/l ratio. Therefore, one of the fundamental guidelines for the structural design of 1-3 composite is to increase the ceramic-polymer interface area.

We now proceed to calculate the hydrostatic piezoelectric constant for the single-rod 1-3 composite shown in Fig. 1. The boundary condition for this problem should be constant stress on all surfaces of the composite. However, this boundary condition is not satisfied in the previous theoretical models which assumed isostrain boundary condition in the axial direction of the rods. Therefore, the effective hydrostatic piezoelectric constant of the 1-3 structure calculated from the previous models is often much larger than the experimental values.[5,9] The simple parallel model and series model could not give the right result because the conditions of isostrain in the z direction and equal stress in the x and y directions are self-contradictory. When stresses are applied in the x and y directions, the induced displacement in the z direction will be quite different in the ceramic and polymer phases, due to the difference in elastic com-
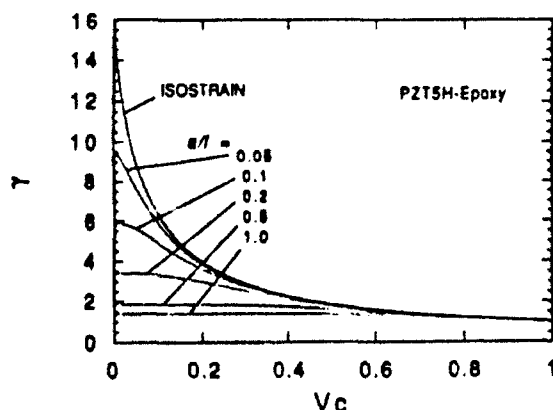

FIG. 3. Calculated dependence of the amplification factor γ on the ceramic content for a PZT5H-epoxy composite with the following aspect ratio: $a/l = 0.05, 0.1, 0.2, 0.5$, and 1.0. The uppermost line is the isostrain result.
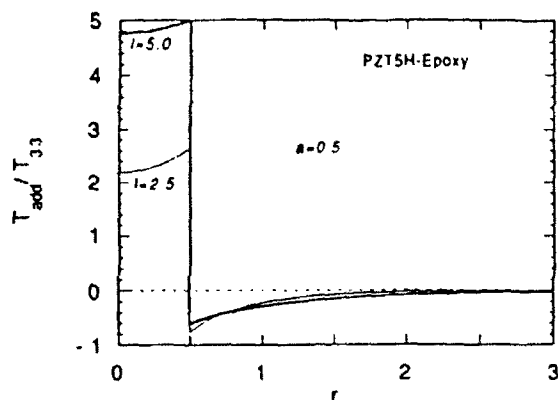
FIG. 4. Concentration of the generated additional stress T_{add} as a function of r for a single-rod PZT5H-epoxy 1-3 composite under a uniaxial stress T_3. The radius of the ceramic rod is 0.5. The thick line is for $l=5$ and the thin line for $l=2.5$. The maximum value of the additional stress appears at the interface $r=0.5$, and the signs of the stresses in the two phases are opposite.

pliance. Although the series model may be used in the x and y direction, the equal strain model must not be used in the z direction unless infinitely stiff plates are placed on the two surfaces of the composite. In order to adequately calculate the hydrostatic piezoelectric constant for the 1-3 composite, one must consider all three dimensions simultaneously and the solution should satisfy equal stress boundary conditions in all three dimensions.

Before we calculate the effective hydrostatic piezoelectric constant of the composite structure, let us discuss briefly the physics involved in the 1-3 structure. Equation (1) may be rewritten in the following form:

$$\frac{2}{l}u\left(r,\frac{l}{2}\right)=s^{p}_{33}\left[T_3+\frac{\mu^{p}l}{4}\left(\frac{\partial^2 u(r,l/2)}{\partial r^2}+\frac{1}{r}\frac{\partial u(r,l/2)}{\partial r}\right.\right.$$
$$\left.\left.+\frac{1}{r^2}\frac{\partial^2 u(r,l/2)}{\partial\phi^2}\right)\right], \quad (18)$$

where $s^{p}_{33}=1/Y^{p}$ is the normal elastic compliance of the polymer. Equation (18) tells us that, in the composite, the effective T^{eff}_3 [in the square bracket of Eq. (18)] is inhomogeneous due to the additional stress generated by the nonslip ceramic-polymer interface, although the applied stress T_3 is homogeneous. While in the other two dimen-

sions, there is no interface enhancement effect, the stress will still be homogeneous, but the stresses applied in the directions perpendicular to the z direction can generate additional stress in the z direction due to the Poisson's ratio effect and the difference of elastic compliance in the two phases. When normal stresses are applied in all three dimensions, the local strain-stress relation in the z direction inside the polymer may be written as

$$\frac{2}{l}u\left(r,\frac{l}{2}\right)=s^{p}_{33}\left[T_3+\frac{\mu^{p}l}{4}\left(\frac{\partial^2 u(r,l/2)}{\partial r^2}+\frac{1}{r}\frac{\partial u(r,l/2)}{\partial r}\right.\right.$$
$$\left.\left.+\frac{1}{r^2}\frac{\partial^2 u(r,l/2)}{\partial\phi^2}\right)\right]+s^{p}_{31}T_1+s^{p}_{31}T_2. \quad (19)$$

For the case of hydrostatic pressure, $T_1=T_2=T_3=-P$, Eq. (19) becomes

$$\frac{\mu^{p}l}{4}\left(\frac{\partial^2 u(r,l/2)}{\partial r^2}+\frac{1}{r}\frac{\partial u(r,l/2)}{\partial r}+\frac{1}{r^2}\frac{\partial^2 u(r,l/2)}{\partial\phi^2}\right)$$
$$=\frac{2Y^{p}}{l}u\left(r,\frac{l}{2}\right)+(1-2\sigma)P, \quad (20)$$

where $\sigma=s^{p}_{31}/s^{p}_{33}$ is the Poisson's ratio for the polymer. Equation (20) is identical to Eq. (1a) if we replace T_3 with $-(1-2\sigma)P$. Similarly one can reach the same conclusion for the ceramic phase, except in this case we must replace T_3 by $-(1-2\sigma^{c})P$, with $\sigma^{c}=s^{c}_{31}/s^{c}_{33}$.

Now the electric displacement in the ceramic under a hydrostatic pressure can be written as

$$D(r)=d_{33}\left[T_3+\frac{c_{44}l}{4}\left(\frac{\partial^2 v(r,l/2)}{\partial r^2}+\frac{1}{r}\frac{\partial v(r,l/2)}{\partial r}\right.\right.$$
$$\left.\left.+\frac{1}{r^2}\frac{\partial^2 v(r,l/2)}{\partial\phi^2}\right)\right]+d_{31}T_1+d_{32}T_2$$
$$=d_{33}\left(\frac{2v(r,l/2)}{ls^{c}_{33}}-2\sigma^{c}P\right)-2d_{31}P. \quad (21)$$

Equation (21) includes both the Poisson's ratio effect and the interface enhancement.

From Eq. (11) the total charge Q produced by the hydrostatic pressure P can be obtained by integrating Eq. (21) over the end surface of the ceramic rod,

$$Q=-\pi a^2(\gamma_h d_{33}+2d_{31})P, \quad (22)$$

where

$$\gamma_h=1+\frac{(l/a)I_1(\rho^{c}_{a})[I_1(\rho^{p}_{R})K_1(\rho^{p}_{a})-I_1(\rho^{p}_{a})K_1(\rho^{p}_{R})][(1-2\sigma)/Y^{p}-(1-2\sigma^{c})s_{33}]}{\sqrt{(2s_{33}/c_{44})}I_0(\rho^{c}_{a})[I_1(\rho^{p}_{R})K_1(\rho^{p}_{a})-I_1(\rho^{p}_{a})K_1(\rho^{p}_{R})]+\sqrt{(2/Y^{p}\mu^{p})}I_1(\rho^{c}_{a})[I_1(\rho^{p}_{R})K_0(\rho^{p}_{a})+K_1(\rho^{p}_{R})I_0(\rho^{p}_{a})]} \quad (23)$$

is the amplification factor in the hydrostatic situation. Compared to Eq. (12), the only difference is the inclusion of the Poisson's ratio effect, i.e., the two factors $(1-2\sigma)$ and $(1-2\sigma^{c})$.

From Eq. (22) the effective hydrostatic piezoelectric

constant $\overline{d_h}$ of the composite is therefore given by

$$\overline{d_h}=(\gamma_h d_{33}+2d_{31})(a^2/R^2)=V_c(\gamma_h d_{33}+2d_{31}), \quad (24)$$

where V_c is the volume fraction of the ceramic. Equation (24) is plotted in Fig. 5 for several different aspect ratios
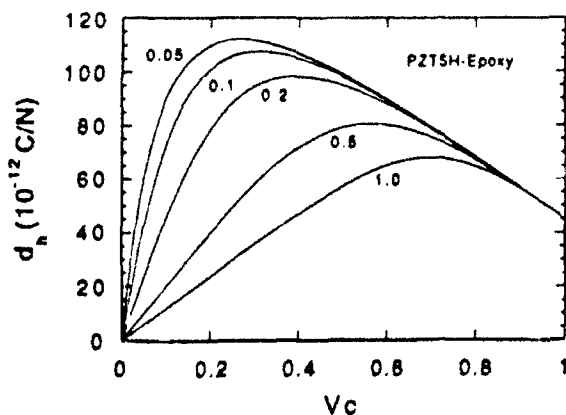
FIG. 5. The hydrostatic piezoelectric constant $\bar{d}_h$ as a function of the ceramic content at a/l ratios of 0.05, 0.1, 0.2, 0.5, and 1.0 for a single-rod PZT5H-epoxy 1-3 composite.

for a PZT5H-epoxy composite using the input data from Table I. $\bar{d}_h$ shows a peak value for each value of a/l; this peak value appears at about 25% for $a/l = 0.05$ and shifts to higher ceramic content with the increase of a/l. The peak value increases with the decrease of the ratio a/l; however, there is a saturation of the aspect ratio effect as one can see from Fig. 5. We found that the curve for $a/l = 0.05$ is already very close to the saturated value; very little improvement is obtained when the ratio is further decreased to $a/l = 0.02$. The curves for $a/l = 0.02$ and 0.01 are practically the same.

The 1-3 structure also increases the effective piezoelectric charge constant $\bar{g}_h$ because the effective dielectric constant of the composite is reduced. For hydrostatic applications the conventional criterion for the 1-3 composites is the hydrostatic figure of merit which is defined as $\bar{g}_h \bar{d}_h$. For the 1-3 structure, it can be written as follows:

$$\bar{g}_h \bar{d}_h = \frac{\bar{d}_h^2}{(\epsilon^c - \epsilon^p)V_c + \epsilon^p} \quad (25)$$
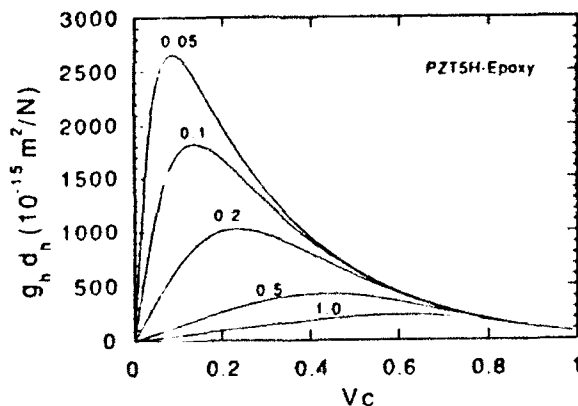

FIG. 6. The figure of merit, $\bar{d}_{33}\bar{g}_{33}$, as a function of the ceramic content with the a/l ratios of 0.05, 0.1, 0.2, 0.5, and 1.0, respectively, for a single-rod PZT5H-epoxy 1-3 composite.

Figure 6 is the plot of Eq. (25) as a function of the ceramic content at four different aspect ratios for the PZT5H-epoxy composite using the input data from Table I. One can see that the figure of merit also strongly depends on the ratio a/l. In the commonly used range of the aspect ratio, the hydrostatic figure of merit can be well over 2000×10^{-15} m^2/N for the optimized structure, which is much larger than the conventional piezoelectric ceramics.

III. SOLUTIONS FOR A SINGLE CERAMIC TUBE COMPOSITE

The stress distribution in Fig. 4 tells us that the most useful parts for the stress transfer are those near the ceramic-polymer interface, which suggests that the shape of the ceramic component should be designed to have larger interface area with the polymer. An immediate design possibility would be to replace the ceramic rods with tubes, since for thin wall tubes the interface area can be substantially increased as compared to the solid rods for the same ceramic content. Clearly, from the principle of stress transfer, the structure will be more effective if the interior of the tube is filled with polymer assuming no surface capping. The unit cell for this case is plotted in Fig. 2. In what follows we only give the results for the filled interior tube composite. One can easily derive the solutions for the case of empty interior tube composite following the same procedure.

As shown in the previous section, the hydrostatic case may be treated the same way as the uniaxial case for the 1-3 composite systems. Therefore, we only need to consider the situation of the composite under a uniaxial stress T_3. For the tube composite the unit cell contains three different regions: $r < a_1$; $a_1 < r < a_2$; and $a_2 < r < R$ as shown in Fig. 2. The surface displacement profiles of the composite in the three regions are, respectively, given by

$$u\left(r, \frac{l}{2}\right) = \begin{cases} A_1 I_0\left(\dfrac{r}{\xi^p}\right) + \dfrac{lT_3}{2Y^p}, & r < a_1, \\ B_1 K_0\left(\dfrac{r}{\xi^p}\right) + B_2 I_0\left(\dfrac{r}{\xi^p}\right) + \dfrac{lT_3}{2Y^p}, & a_2 < r < R, \end{cases} \quad (26)$$

$$v\left(r, \frac{l}{2}\right) = C_1 K_0\left(\frac{r}{\xi^c}\right) + C_2 I_0\left(\frac{r}{\xi^c}\right) + \frac{l}{2}s_{33}T_3, \quad a_1 < r < a_2. \quad (27)$$

The five integration constants in Eqs. (26) and (27) can be obtained using the same boundary conditions as given in Eqs. (6)-(8) at $r = a_1$, a_2, and R, respectively. Because the expressions for these constants are lengthy, we define the following quantities:

$I_{01} = I_0(a_1/\xi^p)$, $I_{02} = I_0(a_2/\xi^p)$, $I_{11} = I_1(a_1/\xi^p)$,

$K_{0\bar1} = K_0(a_1/\xi^c)$, $I_{0\bar1} = I_0(a_1/\xi^c)$, $I_{0\bar2} = I_0(a_2/\xi^c)$,

$I_{1\bar1} = I_1(a_1/\xi^c)$, $K_{0\bar2} = K_0(a_2/\xi^c)$, $I_{12} = I_1(a_2/\xi^p)$,

$I_{1\bar2} = I_1(a_2/\xi^c)$, $K_{02} = K_0(a_2/\xi^p)$, $K_{12} = K_1(a_2/\xi^p)$

$K_{1\bar1} = K_1(a_1/\xi^c)$, $K_{1\bar2} = K_1(a_2/\xi^c)$,

$I_{1R} = I_1(R/\xi^p)$, $K_{1R} = K_1(R/\xi^p)$.

In terms of these abbreviations the integration constants in Eqs. (25) and (26) can be written as

$$A_1 = \beta [I_{1\bar1}(K_{0\bar1} - K_{0\bar2} - \lambda K_{1\bar2}) + K_{1\bar1}(I_{0\bar1} + I_{0\bar2} - \lambda I_{1\bar2})] T_3, \tag{28}$$

$$B_1 = \frac{\beta I_{1R}[R^E I_{01}(I_{1\bar2}K_{1\bar1} - I_{1\bar1}K_{1\bar2}) + I_{11}I_{1\bar2}(K_{0\bar1} - I_{0\bar2}) + I_{11}K_{1\bar2}(I_{0\bar1} + I_{0\bar2})] T_3}{I_{12}K_{1R} - I_{1R}K_{12}}, \tag{29}$$

$$B_2 = \frac{\beta K_{1R}[R^E I_{01}(I_{1\bar2}K_{1\bar1} - I_{1\bar1}K_{1\bar2}) + I_{11}I_{1\bar2}(K_{0\bar1} - I_{0\bar2}) + I_{11}K_{1\bar2}(I_{0\bar1} + I_{0\bar2})] T_3}{I_{12}K_{1R} - I_{1R}K_{12}}, \tag{30}$$

$$C_1 = \beta [R^E I_{01}I_{1\bar1} - I_{11}(I_{0\bar1} + I_{0\bar2} + \lambda I_{1\bar2})] T_3, \tag{31}$$

$$C_2 = \beta [R^E I_{01}K_{1\bar1} + I_{11}(K_{0\bar1} - K_{0\bar2} - \lambda K_{1\bar2})] T_3, \tag{32}$$

where

$$R^E = \sqrt{c_{44}/s_{33}\mu^p Y^p}, \quad \lambda = R^E(I_{1R}K_{02} + I_{02}K_{1R})/(I_{12}K_{1R} - I_{1R}K_{12}),$$

and

$$\beta = \frac{(1/Y^p - s_{33})l/2}{R^E I_{01}(I_{1\bar1}K_{0\bar2} + \lambda I_{1\bar1}K_{1\bar2} - \lambda I_{1\bar2}K_{1\bar1} + K_{1\bar1}I_{0\bar2}) - I_{11}(I_{0\bar1}K_{0\bar2} + \lambda I_{0\bar1}K_{1\bar2} + \lambda I_{1\bar2}K_{0\bar1} - I_{0\bar2}K_{0\bar1})}.$$

Similar to the previous section, one can find the total charge Q produced at the top surface of the ceramic tube under a uniaxial stress T_3,

$$Q = 2\pi \int_{a_1}^{a_2} \frac{2d_{3}}{ls_{33}} v\left(r, \frac{l}{2}\right) r \, dr = \gamma d_{33} T_3 \pi (a_2^2 - a_1^2). \tag{33}$$

where

$$\gamma = 1 + \frac{\sqrt{2c_{44}/s_{33}}}{T_3(a_2^2 - a_1^2)} [C_1(a_1 K_{1\bar1} - a_2 K_{1\bar2})$$

$$+ C_2(a_2 I_{1\bar2} - a_1 I_{1\bar1})] \tag{34}$$

is the stress amplification factor for the tube composite under uniaxial stress. One can verify that Eq. (34) recovers the result of Eq. (12) in the limit of $a_1 \to 0$.

In Fig. 7 we have plotted Eq. (34) for a single-tube composite of $l = 5$ and $R = 5$. The ceramic fractions are 0.01, 0.02, 0.05, 0.1, 0.2, and 0.5, respectively, as labeled in the figure. One can see that for each specified ceramic volume percentage the γ value increases with the increase of the inner radius of the tube a_1 at the beginning, then decreases slightly after reaching a peak value. For the 1% ceramic composite, the γ value can be increased by as much as a factor of 2 compared to the ceramic rod composite ($a_1 = 0$, and for the corresponding 1% ceramic single-rod composite the a/l ratio is 0.1). The slight decrease of γ for large a_1 is caused by the gradual disappearance of the outer interface in the structure, as one can see

that the ceramic tube becomes the outer shell for the structure when a_1 is sufficiently large, i.e., $a_2 = R$.

Due to the increase of the interface area in the tube ceramic configuration, the effective volume of the polymer that participates in the stress transfer becomes larger. As a result, more charges are produced for the same ceramic content compared with the solid rod composite. In other words, the ceramic tubes are more effective for stress transfer than the solid ceramic rods in the 1-3 composite structure. In principle, other ceramic geometries can also be analyzed in the same manner. However, the displacement field will also depend on the angular variable ϕ for noncylindrical symmetries, which may defy an analytic solution.

IV. SUMMARY AND CONCLUSIONS

A theoretical study has been carried out for the 1-3-type composites based on the model developed in Ref. 6. As examples, a single-rod and single-tube composite have been treated for cylindrical symmetry. Analytic solutions are obtained for the inhomogeneous surface displacements in the z direction under both uniaxial and hydrostatic stress. From these inhomogeneous displacement solutions, the effective piezoelectric constants of 1-3 composites can be calculated.
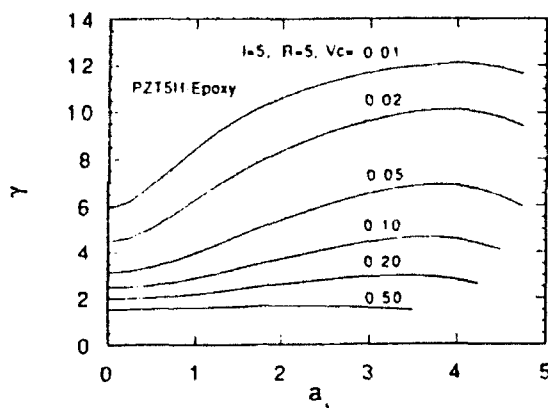
5820   J. Appl. Phys., Vol. 72, No. 12, 15 December 1992

Cao, Zhang, and Cross   5820

FIG. 7. The change of the amplification factor γ for a single-tube composite with the inner radius of the ceramic tube a_1 for the following volume fractions of ceramic: 0.01, 0.02, 0.05, 0.1, 0.2, and 0.5.

The stress transfer in the 1-3 composites is accomplished through shear coupling at the interface between the two components. Because of the difference in elastic compliance, the two phases cannot have isostrain under uniaxial or hydrostatic stress without surface capping. The effectiveness of the stress transfer can be characterized by a stress amplification factor γ defined in Eqs. (12), (23), and (34). This stress amplification factor is shown to depend on the elastic properties of both phases, the ceramic content, and, more important, the aspect ratio of the ceramic rods. It is shown that the stress transfer effect practically vanishes if the ratio $a/l > 1$. We have also demonstrated that the hydrostatic stress case can be treated in the same way as the uniaxial stress. However, because of the Poisson's ratio effect, the stresses applied in the directions perpendicular to the axial direction of the rod reduces the enhancement effect in the axial direction. Hence, under hydrostatic pressure the amplification factor γ_h is practically reduced by a factor of $(1 - 2\sigma)$ due to the Poisson's ratio effect, where σ is the Poisson's ratio.

Through the stress analyses, we have shown clearly that the most effective portion of the polymer for the stress transfer is in the vicinity of the ceramic-polymer interface. Therefore, the optimum design for the 1-3 composite structure should contain maximum interface area. If the ceramic volume content and the thickness of the 1-3 structure are fixed, the composite made of ceramic tubes is more effective than the composite made of solid rods due to larger interface area.

In a real 1-3 composite structure the outside boundary of the unit cell is not circular, and the cross section of the ceramic rods may have square or other geometries, for which one must solve each case according to the specified boundary conditions. In general, it may not be possible to obtain closed form expressions, one may have to resort to numerical methods. However, at very low ceramic content, i.e., if the rods are sufficiently far from each other, the single-rod solution obtained here is a very good first-order

approximation. Looking at the stress analyses in Fig. 4, we note that the polymer beyond $r = 2.5$ actually contributed very little in the stress transfer. This rod distance corresponds to a ceramic volume percentage of about 4%. Therefore, the solutions derived here should be accurate for any rod arrangement if the ceramic content is less than 4%. We have shown that the calculated piezoelectric constant is comparable to the experimental result even for up to 20% ceramic.[10]

Through this theoretical study we have gained substantial insight into the fundamental principles of the 1-3 piezoelectric composite structure, including the mechanism of stress transfer and the influence of the aspect ratio. Several design principles for the 1-3 structure can therefore be stated based on the current study as follows.

(i) The ratio a/l should be relatively small. However, one must note that the enhancement of the stress transfer through reducing the a/l ratio has an upper limit. In the PZT5H-epoxy system (see Fig. 3), if $a/l = 0.02$, the γ value essentially reaches the upper limit. Thus, there is no benefit in making the ratio a/l less than 0.02 for this system since the decrease of a/l ratio of the ceramic rods often increases the difficulties in manufacturing 1-3 composites. Using our theoretical results, one can select the design parameters to optimize the performance of 1-3 composites for a specific purpose and at the same time minimize the cost of manufacturing.

(ii) The interface area between the two phases should be maximized so that the effective region of the polymer participating in the stress transfer is maximized.

(iii) From Eq. (14) one may conclude that the passive phase should be chosen to have the smallest possible Young's modulus (depending on the requirement of mechanical strength for the composite) in order to obtain a large γ. In addition, a larger ratio of the shear modulus versus Young's modulus for the passive phase is preferred, which can reduce the self loading of the polymer phase and increase the stress transferred to the ceramic phase. This might be achieved through a surface capping technique.

ACKNOWLEDGMENT

[1] R. E. Newnham, D. P. Skinner, and L. E. Cross, Mater. Res. Bull. 13, 525 (1978).
[2] D. P. Skinner, R. E. Newnham, and L. E. Cross, Mater. Res. Bull. 13, 599 (1978).
[3] W. A. Smith, A. Shaulov, and B. A. Auld, in Proceedings of the 1985 IEEE Ultrasonics Symposium, pp. 642-647.
[4] H. L. W. Chan and J. Unsworth, IEEE Trans. Ultrasonics, Ferroelectrics and Frequency Control UFFC-36, 434 (1989).
[5] K. A. Klicker, Ph.D. thesis, The Pennsylvania State University, University Park, PA, 1980.
[6] W. Cao, Q. Zhang, and L. E. Cross, IEEE Trans. Ultrasonics, Ferroelectrics and Frequency Control (to be published).
[7] Guide to Modern Piezoelectric Ceramic, from Morgan Matroc, Inc., Vernitron Division.
[8] C. G. Oakley, Ph.D. thesis, The Pennsylvania State University, 1991.
[9] M. J. Haun and R. E. Newnham, Ferroelectrics, 68, 123 (1986).
[10] Q. Zhang, W. Cao, H. Wang, and L. E. Cross, J. Appl. Phys. (to be published).

5821   J. Appl. Phys., Vol. 72, No. 12, 15 December 1992

Cao, Zhang, and Cross   5821

APPENDIX 34

Characterization of the performance of 1-3 type piezocomposites for low-frequency applications

Q. M. Zhang, Wenwu Cao, H. Wang, and L. E. Cross

Materials Research Laboratory, The Pennsylvania State University, University Park, Pennsylvania 16802

In general, the piezoelectric ceramic and polymer in a 1-3 type composite will have different deformations when subjected to an external field. How each component deforms, to a large extent, determines the performance of the composite. Based on the force equilibrium condition, an elastic model is introduced to analyze the strain profiles of these composites, and the theoretical results are in quantitative agreement with the strain profiles measured on several composites using a double beam ultradilatometer. The results obtained provide quantitative information on how various parameters in a composite affect the performance of the composite. Furthermore, a scheme is proposed for evaluating the strain profile of a 1-3 type composite under a hydrostatic pressure using a double beam dilatometer.

I. INTRODUCTION

A variety of piezoelectric composite materials can be formed by combining a piezoelectric ceramic with a polymer phase. Among them, the piezoelectric 1-3 composite has attracted a great deal of attention and been used widely.[1-3] A typical configuration of 1-3 type composites is illustrated in Fig. 1. In the composites, piezoelectric ceramics, usually lead zirconia titanate (PZT) ceramics, play the active role of energy conversion between the mechanical energy and electric energy, while the polymer phase acts as a passive medium, which transfers the mechanical energy between the piezoelectric ceramic and the surrounding with which the composite interacts. The disparity in the physical properties between the two constituent phases and different roles they play in a composite make it possible to fine tailor the material properties of a composite to meet different requirements of specific application.[4-7]

There are two major areas where 1-3 composites have been widely used: underwater hydrophone application and ultrasonic actuators and sensors for medical diagnostic devices.[1-4] The former is operated at frequencies below 40 kHz while the latter are operated at a MHz frequency range. As can be seen from Fig. 1, in making a 1-3 composite, several parameters can be varied: the elastic properties of the polymer phase, the shape, and the aspect ratio of the PZT rods, the spacing between the rods, the volume content, and the arrangement of the PZT rods in the composite. The intention of this paper is to provide some understanding of how these design parameters affect the performance of the composites for low-frequency applications. To achieve that, a new model is introduced that treats the composites beyond the earlier equal-strain model.[2,8,9]

When a 1-3 composite is subjected to an electric field or a stress field, a strain field will be induced in the sample. Due to the large difference in the elastic and piezoelectric properties, in general, the two components will have different strain levels and the strain in each component will not be uniform. This strain profile is determined by the parameters listed in the preceding paragraph and determines how effectively the two components in a composite

couple to each other. The strain profile of a composite under an electric field can be mapped out using a double beam ultradilatometer, as will be shown in this paper.[10] However, it may not be measured easily when the composite is subjected to a stress field. In this paper, we will show that the strain profile measured on a composite under an electric field can be used to describe the deformation of the composite under a uniaxial or a hydrostatic stress.

The basic elastic coupling mechanism between the two components in the 2-2 piezoelectric composite is similar to that of the 1-3 composite. Although this structure is not widely used, the mathematical analysis on the performance of the composite is much simpler and the results obtained can also be applied to the 1-3 composite. Hence, in this paper, we will first discuss the performance of 2-2 composites (Sec. II). In Sec. III, 1-3 composites will be analyzed in the dilute limit. In Sec. IV, the results obtained in Sec. III will be applied to 1-3 composites beyond the dilute limit.

II. 2-2 COMPOSITE

In a 2-2 composite, the PZT plates and polymer are arranged in a parallel manner, as schematically drawn in Fig. 2(a). Assuming the sample dimension in the y direction is much larger than the sample thickness L and the spacing d between the neighboring PZT plates, a 2-2 composite can be modeled as a one-dimensional system. When there is a strain change S_1 in PZT plates, for example, due to an electric field on the composite, there will be a corresponding change in the strain profile of the polymer phase. Denoting $u(x)$ the surface displacement of the polymer phase in the z direction, the longitudinal strain S_1 in the z direction of the polymer phase is $2u(x)/L$, where L is the sample thickness. As a result of the strain gradient $u(x)$, a shear force $\mu L\, \partial^2 u(x)/4\, \partial x^2$ will be induced in the z direction, where μ is the shear modulus of the polymer. Under the static condition, this shear force will be balanced by the restoring force $2Yu(x)/L$ in the polymer, that is
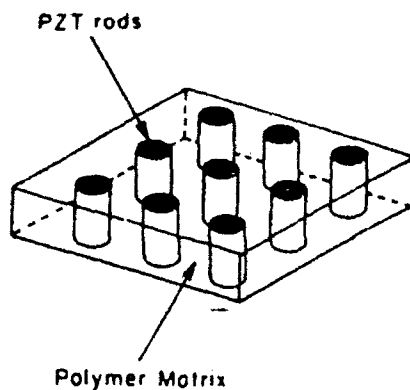
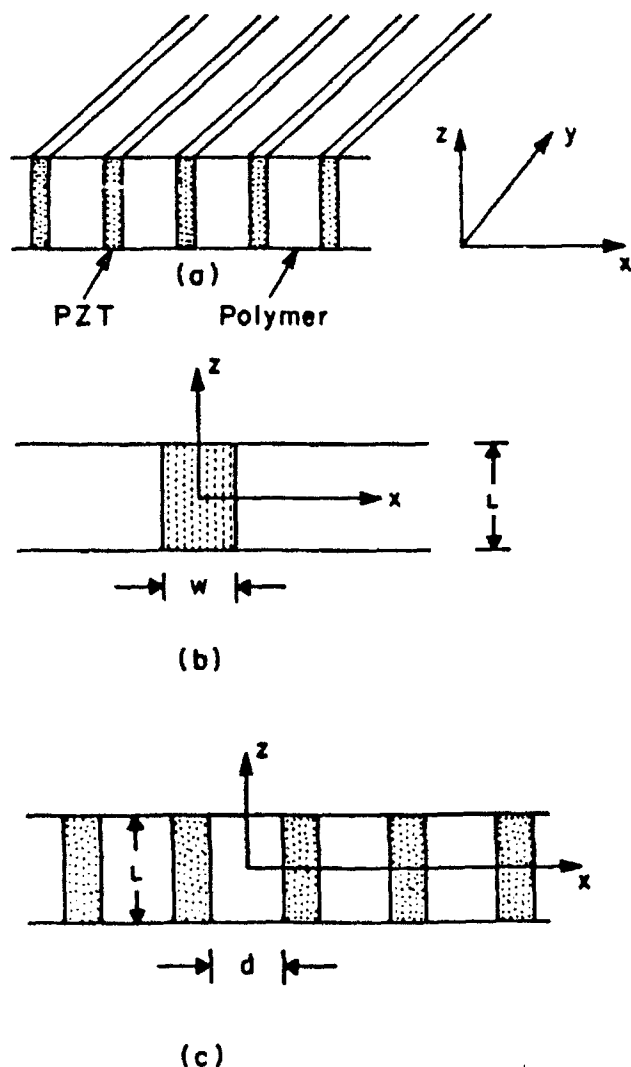FIG. 1 Schematical drawing of a 1-3 PZT-polymer composite, where PZT rods are embedded in a polymer matrix.

FIG. 2 (a) A schematical drawing of a 2-2 composite, where the hatched plates are PZT; (b) the coordinate system for a 2-2 composite with a single PZT plate; and (c) the coordinate system for Eq. (1.3).
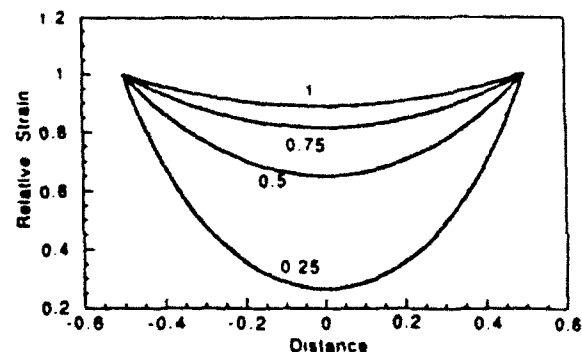

FIG. 3. The strain profile for the polymer between two PZT plates [from Eq. (1.3)]. The parameter shown in the figure for each curve is $\zeta = L/(2\sqrt{2Y/\mu})$. In the figure, the gap width d is 1 mm.

$$\frac{\mu L}{4} \frac{\partial^2 u(x)}{\partial x^2} = \frac{2Y}{L} u(x), \qquad (1.1)$$

where Y is the Young's modulus of the polymer. The details of the derivation of Eq. (1.1) will be presented in a separate paper.[11] The solution to Eq. (1.1) is

$$2u(x)/L = A \exp(2x\sqrt{2Y/\mu}/L) + B,$$

where A and B are integration constants. For the case when there is only one PZT plate in the composite, as shown in Fig. 2(b), the longitudinal strain S_3 of the polymer phase is

$$\left(\frac{2u}{L}\right) = \left(\frac{2u}{L}\right)_0 \exp\left[-\left(x-\frac{w}{2}\right)\frac{2\sqrt{2Y/\mu}}{L}\right] \quad \left(x > \frac{w}{2}\right)$$
(1.2)

and

$$\left(\frac{2u}{L}\right) = \left(\frac{2u}{L}\right)_0 \exp\left[\left(x+\frac{w}{2}\right)\frac{2\sqrt{2Y/\mu}}{L}\right] \quad (x < -w/2),$$

where w is the PZT plate width and $2(u/L)_0$ is the strain at the PZT-polymer interface. Equation (1.2) shows that the strain in the polymer phase decays exponentially with a characteristic length $\xi = L/(2\sqrt{2Y/\mu})$ as the polymer phase moves away from the PZT plate.

For a 2-2 composite as depicted in Fig. 2(c), the solution to Eq. (1.1) is

$$\left(\frac{2u}{L}\right) = \left(\frac{2u}{L}\right)_0 \cosh\left(\frac{2x\sqrt{2Y/\mu}}{L}\right)\mathrm{sech}\left(\frac{d\sqrt{2Y/\mu}}{L}\right),$$
(1.3)

where d is the gap width between the two PZT plates. Equation (1.3) describes the strain profile in the polymer between the two neighboring PZT plates. In Fig. 3, we plot the strain profile of the polymer phase calculated from Eq. (1.3) for $L = 4.7$ mm ($\xi = 1$), 3.5 mm ($\xi = 0.75$), 2.3 mm ($\xi = 0.5$), and 1.2 mm ($\xi = 0.25$) for the gap width $d = 1$ mm. In the calculation, $Y = 4.7 \times 10^9$ N/m^2 and $\mu = 1.7 \times 10^9$ N/m^2, the elastic constants for spurs epoxy were used. The figure shows a strong dependence of induced strain profile in the polymer phase on the sample thickness
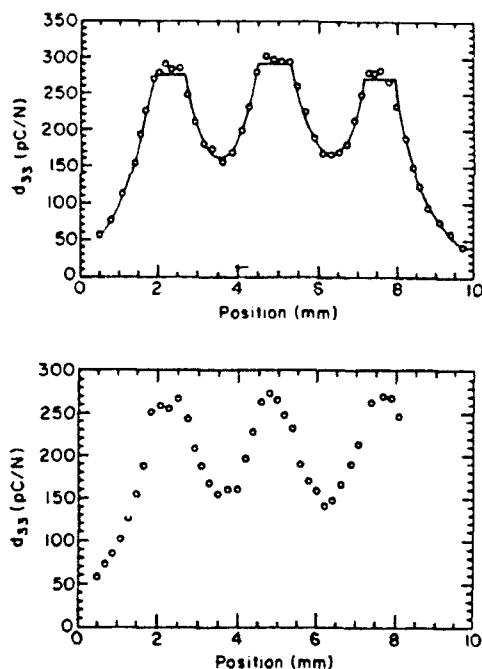
FIG. 4. (a) Strain profile for the 2-2 composite made of PZT-5A and spurs epoxy with thickness $L = 4.5$ mm. The sample is driven electrically at 200 Hz, circles are the data points and the solid lines are the fitting. (b) Strain profile for the 2-2 composite measured at 40 kHz.

From the figure, one can make the following observations: in this one-dimensional structure, as the sample thickness approaches that of the gap width, induced strain in the gap center of the polymer phase approaches zero; On the other hand, for $L/d = 5$, the strain nonuniformity in the polymer phase is less than 10% and the equal-strain model can be used to calculate the effective material properties without introducing significant errors. Equations (1.2) and (1.3) also reveal that the elastic properties of the polymer phase have a significant effect on the strain profile. By reducing Y or increasing μ, one can greatly increase the elastic coupling between the two components.

To compare with the theoretical results, several 2-2 composites were made using PZT-5A (PZT-5A and PZT-5H are trademarks of Vernitro Corp. for their PZT products) plates and spurs epoxy. The strain profile of the sample was measured along a path parallel to the x axis using the double beam laser interferometer when the sample was driven electrically. Shown in Fig. 4(a) is the result of one of the scans thus obtained. The solid line in the figure is the theoretical fitting using Eq. (1.3) for the polymer regions between the PZT plates and Eq. (1.2) for the polymer regions at the two edges of the sample. Clearly, the theoretical curve describes the data quite well. The fitting yields the ratio of $Y/\mu = 3.35$ for spurs epoxy, which is larger than the true value of $Y/\mu (= 2.76)$. We believe that this is due to the fact that in Eq. (1.1), the effect of the stress in the x and y directions is not included. Further

work will be conducted to incorporate the lateral stress effect in the constitutive equations.

Equation (1.1) can be modified to account for the situation when a composite is subjected to a low-frequency driving field (either a stress field or an electric field). By low frequency, we mean that the frequency is at least five times smaller than the first thickness resonance frequency. Under this circumstance, the longitudinal strain in the sample can be approximated as uniform and Eq. (1.1) can be rewritten as

$$\frac{\mu L}{4} \frac{\partial^2 u}{\partial x^2} = \frac{2Y}{L} u + \frac{\rho L}{4} \frac{\partial^2 u}{\partial t^2}, \tag{1.4}$$

to include the time-dependent effect. In Eq. (1.4), ρ is the polymer density. For a sinusoidal strain $u = u(x) \exp(i\omega t)$, where ω is the angular frequency of the driving field, Eq. (1.4) becomes

$$\frac{\mu L}{4} \frac{\partial^2 u}{\partial x^2} = \left(\frac{2Y}{L} - \frac{\rho L \omega^2}{4}\right) u. \tag{1.5}$$

It is easy to realize that as long as the quantity $(2Y/L^2 - \rho\omega^2/4) > 0$, the solution to Eq. (1.5) is the same as that of Eq. (1.1). The strain profile in the polymer region is still described by Eqs. (1.2) and (1.3), except the characteristic decay length ξ becomes $\xi = L/[2\sqrt{2(Y - \rho\omega^2 L^2/8)/\mu}]$. In all the practical cases, the change in ξ is very small. For instance, the change of ξ is about 2% when ω varies from 0 to 40 kHz for the 2-2 composite used here. To verify this, the strain profile of the 2-2 composite was measured at higher frequency (40 kHz) using the laser dilatometer. The data is shown in Fig. 4(b) and the strain profile is almost identical to that measured at 200 Hz [Fig. 4(a)]. The experimental as well as theoretical results both indicate that the polymer strain profile will not change significantly in this low-frequency region.

We now discuss the situation when the composite is subjected to a uniaxial stress T in the z direction. The force balance condition yields

$$T + \left(\frac{\mu L}{4}\right) \frac{\partial^2 u}{\partial x^2} = \frac{2Yu}{L}. \tag{1.6}$$

By making the variable substitution, $v = u - LT/(2Y)$, Eq. (1.6) becomes identical to Eq. (1.1). Hence the solution to Eq. (1.6) for the polymer strain profile between two PZT plates is

$$\left(\frac{2u}{L}\right) = A \cosh\left(\frac{-2x\sqrt{2Y/\mu}}{L}\right) + \frac{T}{Y}, \tag{1.7}$$

where $A = [(2u/L)_0 - T/Y]\text{sech}(- d\sqrt{2Y/\mu}/L)$. $(2u/L)_0$ is the strain at the PZT-polymer interface, and d is the gap width of the polymer phase between the two PZT plates.

Comparison of Eq. (1.3), which is the polymer strain profile induced by the PZT plates when the composite is driven electrically, with Eq. (1.7), which is the strain profile of the polymer phase when a uniaxial stress is applied on the composite, yields that except for the prefactor and a constant term, the functional forms of the two cases are the
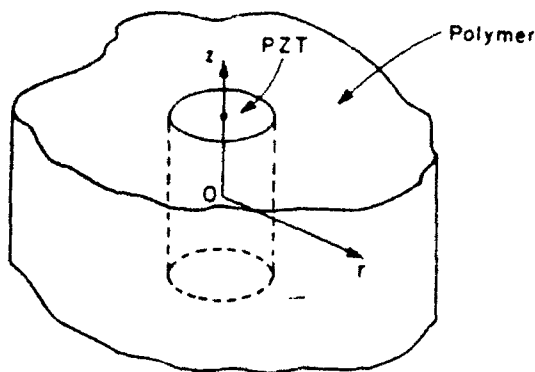
FIG. 5. 1-3 composite in the dilute limit.

FIG. 6. (a) Decay of the strain in the polymer phase for (from the top to the bottom) a 2-2 composite [Eq. (1.2)] with $\xi = 1$, a single rod 1-3 composite with $\xi = 1$, $\xi = 0.5$, and $\xi = 0.25$, where $\xi = L/(2\sqrt{2Y/\mu})$. In the 1-3 composite, the PZT rod radius is 0.3 mm. The strain S_3 in the polymer phase is normalized to that of PZT rod S_{30}. The abscissa is the distance from the polymer-PZT interface. (b) The dependence of the strain in the polymer phase on the radius of a PZT rod in a 1-3 composite in the dilute limit. From the top to the bottom $a = 0.1, 0.2, 0.3, 0.5$ mm. In all the curves, $\xi = 1$. r is distance defined in Fig. 5.

III. 1-3 COMPOSITE IN THE DILUTE LIMIT

In the dilute limit, the performance of a 1-3 composite can be modeled as that of a single PZT rod embeded in an infinitely extended polymer matrix, as schematically drawn in Fig. 5. From the symmetry of the problem, a cylindrical coordinate system is chosen with the z and r directions along the axis of the PZT rod and the radial direction, respectively. Similar to the situation for Eq. (1.1), the equation that describes the equilibrium condition of the polymer phase when the composite is driven electrically is

$$\frac{\mu L}{4}\left(\frac{\partial^2 u}{\partial r^2}+\frac{\partial u}{r\,\partial r}\right)=\frac{2Yu}{L}. \tag{2.1}$$

The meaning of each term in Eq. (2.1) is the same as that in Eq. (1.1). Equation (2.1) can be transformed to the zeroth-order Bessel equation of the imaginary argument. The solution that satisfies the boundary condition $r \to \infty$, $u/L \to 0$, is the imaginary argument zeroth-order Hankel function $K_0(\rho)$, where $\rho = 2r\sqrt{2Y/\mu}/L$. When the strain in the polymer phase is induced by the PZT rod, the solution to Eq. (2.1) is

$$(2u/L) = (2u/L)_0 K_0(\rho)/K_0(a/\xi), \tag{2.2}$$

where $(2u/L)_0$ is the strain at the PZT rod–polymer interface, a is the radius of the PZT rod, and $\xi = L/(2\sqrt{2Y/\mu})$.

It is interesting to compare the strain profile of the polymer phase in the 2-2 composite with that in the 1-3 composite. Shown in Fig. 6(a) are the strain profiles calculated from Eq. (2.2) (single PZT rod 1-3 composite) and from Eq. (1.2) (single PZT plate 2-2 composite). Apparently, the strain decay in the polymer phase in a 1-3 composite is much faster than that in a 2-2 composite. Besides that, there is an additional difference between the two cases: the decay in the polymer phase for a 1-3 composite also depends on the PZT rod diameter $2a$, while in
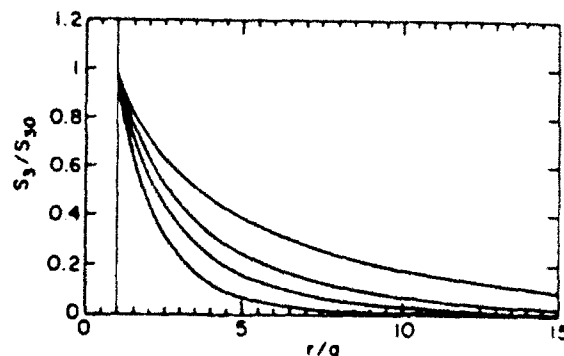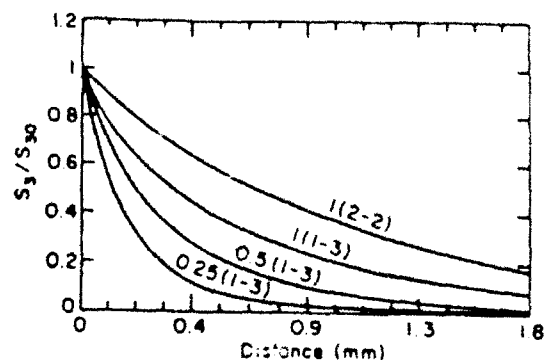
a 2-2 composite, it is independent of the PZT plate width. To illustrate this, in Fig. 6(b), the strain profiles in the polymer phase for PZT rod radius $a = 0.1, 0.2, 0.3, 0.5$ mm are plotted, where $\xi = 1$ and $(2u/L)_0 = 1$ are assumed for all the cases. Therefore, both the elastic properties of the polymer phase and the aspect ratio of the PZT rod are important parameters in determining the performance of 1-3 composites.[8,12]

Shown in Fig. 7 is the strain profile measured on a 1-3 composite made of a single PZT tube embeded in spurs epoxy matrix. The strain profile was mapped out using the double beam ultradilatometer when the sample was driven electrically at 200 Hz. The solid line in the figure is $K_0(r/\xi)$, the strain profile predicted theoretically. The only adjustable parameter in the fitting is ξ, and the theoretically calculated curve agrees with the experimental data quite well. The fitting yields the ratio of $Y/\mu = 3.35$ for the spurs epoxy used, which is the same as that measured in the 2-2 case. The consistency between the two measurements indicates that the model contains the essence of the elastic coupling between the two components in 1-3 type composites.

In what follows, the elastic coupling between the PZT rod and polymer will be analyzed using this model for the composite subjected to (a) an electric field E along the z
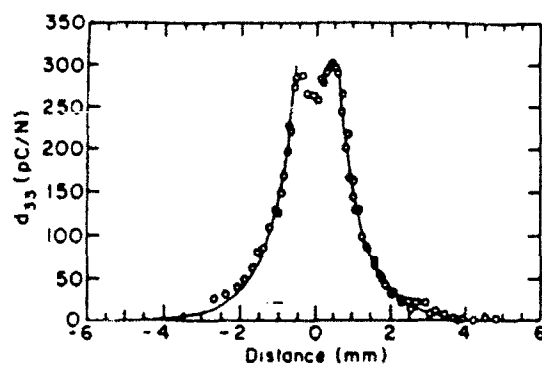
FIG 7. The strain profile of a single tube 1-3 composite (tube o d $=1.2$ mm) measured at 200 Hz using the double beam ultradilatometer. The composite is made of PZT-5H tube and spurs epoxy. Solid lines are the fittings using Eq. (2.2) with only one adjustable parameter ξ ($\xi = 1.15$ from the fitting). Sample thickness $L = 4.:$ mm.

TABLE I Stress amplification factor for 1-3 composites

$Y^s{}_{33}$	0.02	0.1
a(mm)	γ	γ
0.1	31.4	9.0
0.2	8.3	7.6
0.5	7.1	4.8
1.0	3.6	3.0

direction; (b) a uniaxial stress T along the z direction; and (c) a hydrostatic pressure. In all the cases, the poling direction of the PZT rod is in the z direction.

(a) when an electric field E is applied to the composite, from the constitutive equation, one can obtain the z component of the strain in the PZT rod $S_0 = d_{33} E$ if there is no elastic coupling between the PZT rod and polymer. The effect of the polymer on the PZT rod is to add a mechanical load to it. In this situation, the strain in the polymer phase is described by Eq. (2.2). The stress transferred from the polymer to the PZT rod due to this strain field is

$$T = -Y(2u/L)_0 F(a,\xi),\qquad (2.3)$$

where $(2u/L)_0$ is the strain in the PZT rod after the polymer loading and

$$F(a,\xi) = \frac{2\xi K_1(a/\xi)}{a},\qquad (2.4)$$

where $\xi = L/(2\sqrt{2Y/\mu})$, a is the radius of the PZT rod, and $K_1(x)$ is the first-order modified Bessel function. The strain of the PZT rod due to this additional polymer loading is

$$\left(\frac{2u}{L}\right)_0 = \frac{d_{33}E}{1 + {}^c s_{33} Y F(a,\xi)},\qquad (2.5)$$

where ${}^c s_{33}$ is the elastic compliance of PZT. Clearly, due to the polymer loading, the strain level of the PZT rod is smaller than $d_{33}E$. Using Eq. (2.5), one can calculate the strain reduction $(2u/L)_0/(d_{33}E)$ if ${}^c s_{33} Y$ and ξ are known. For a thin PZT rod (small a), even when the elastic compliance of the polymer is much larger than that of PZT, the reduction in the strain of the PZT rod can still be substantial.

In general cases, $d_{33}E$ can be replaced by S_0, the strain of the PZT rod without the polymer matrix. Hence the total stress on the PZT rod is

$$T = -\frac{Y S_0 F(a,\xi)}{1 + {}^c s_{33} Y F(J,\xi)}.\qquad (2.6)$$

A large stress would arise during the poling of a 1-3 composite since S_0 is relatively large as the PZT rods are poled, and this stress acts as a depoling field on the PZT rods in composites. For example, considering a composite made of a PZT-5H rod and spurs epoxy, taking $a = 0.2$ mm, $L = 5.2$ mm, $S_0 = 0.1\%$, $\xi = 1$, ${}^c s_{33} Y = 0.1$, and $Y = 4.7 \times 10^9$ N/m^2, the stress on the PZT rod is 3.4×10^7 N/m^2.

(b) From the result of the preceding section, the strain profile of the polymer phase under a uniaxial stress T in the z direction is

$$(2u/L) = A K_0(r/\xi) + T/Y,\qquad (2.7)$$

where $A = [(2u/L)_0 - T/Y]/K_0(a/\xi)$. $(2u/L)_0$ is the strain of the PZT rod. When a composite is used in this situation, one major concern is how much the stress on the polymer will be transferred to the PZT rod. To calculate this quantity, we notice that without the elastic coupling to the PZT rod the strain in the polymer under the stress T is T/Y. By subtracting out this quantity from Eq. (2.7), one can obtain the change in the strain profile of the polymer phase due to the elastic coupling to the PZT rod. From this consideration, T_{tr}, the stress transferred from the polymer to the PZT rod is

$$T_{tr} = T \left| \frac{1 + F(a,\xi)}{1 + ({}^c s_{33} Y) F(a,\xi)} - 1 \right|.\qquad (2.8)$$

or in a more familiar language, the stress amplification factor γ due to the composite

$$\gamma = T_{total}/T = [1 + F(a,\xi)]/[1 + ({}^c s_{33} Y) F(a,\xi)],\qquad (2.9)$$

where $T_{total} = T + T_{tr}$ is the total stress applied to the PZT rod. In Table I, γ is calculated for composites with a different radius of the PZT rod and different elastic properties of the constituent phases ($\xi = 1$). For a composite with a fixed volume percentage of PZT rods, the effective d_{33} of the composite is proportional to γ. Therefore, the result in Table I illustrates how the effective d_{33} of the composite changes as one varies the radius of PZT rods. Clearly, to increase the piezoelectric response of the composite, thin PZT rods should be used. The result in Table I also shows that the polymer self-loading (polymers with a large Young's modulus) will significantly reduce the amount of stress to be transferred to the PZT rod and result in a smaller γ.

In Eq. (2.9), as Y/μ approaches zero, $F(a,\xi)$ will approach the value of the equal-strain model and γ reaches its maximum value for a fixed ${}^c s_{33} Y$. Hence, to improve the

stress transfer in a composite, a polymer with a large μ and a small Y will be advantageous.

(c) In the hydrophone application, a 1-3 composite is subjected to a hydrostatic pressure. The stress on the composite will modify the equilibrium equation (2.1) of the polymer phase to

$$\left(\frac{2u}{L}\right) = s_{33}T_3 + s_{31}T_1 + s_{32}T_2 + s_{33}\mu \frac{L}{4}\left[\frac{\partial^2 u}{\partial r^2} + \left(\frac{1}{r}\right)\frac{\partial u}{\partial r}\right].$$
(2.10)

Making use of the relation $s_{31} = s_{32} = -\sigma s_{33}$, where σ is the Poisson's ratio of the polymer, $T_1 = T_2 = T_3 = T$ in the hydrostatic condition, and $Y = 1/s_{33}$, Eq. (2.10) can be rewritten as

$$Y\left(\frac{2u}{L}\right) = (1 - 2\sigma)T + \frac{\mu L}{4}\left[\frac{\partial^2 u}{\partial r^2} + \left(\frac{1}{r}\right)\frac{\partial u}{\partial r}\right].$$
(2.11)

The solution to this equation is

$$\left(\frac{2u}{L}\right) = (1 - 2\sigma)\frac{T}{Y} + \left[\left(\frac{2u}{L}\right)_0 - (1 - 2\sigma)\frac{T}{Y}\right]\frac{K_0(r/\xi)}{K_0(a/\xi)}.$$
(2.12)

The meaning of each quantity in Eq. (2.12) is the same as that in Eq. (2.7). Comparison between Eqs. (2.7) and (2.12) yields that the effect of hydrostatic pressure on a composite is to reduce the effective pressure on the polymer phase from T to $(1 - 2\sigma)T$. In the case of $\sigma = 0.5$, this effective pressure becomes zero, a situation where the polymer becomes incompressible. On the other hand, Eq. (2.12) shows that the strain profile in the polymer phase is still described by the elastic constant ratio $2Y/\mu$, which is the same as that in the uniaxial stress situation. Hence, it is more appropriate to describe the reduction of the polymer strain level in the hydrostatic case as related to the reduction of the effective stress on its surface, rather than the change in the elastic constants of the material.

To find the total stress T_{total} exerted on the PZT rod, one has to calculate the strain of the PZT rod $(2u/L)_0$ in the composite under the hydrostatic pressure T. Using the reciprocal relation that the total force of the polymer phase on the PZT rod is equal in magnitude and opposite in sign to the total force of the PZT rod on the polymer phase, one can find T_{total},

$$T_{total}$$

$$= T\frac{1 + (1 - 2\sigma)F(a,\xi) - Y[{}^cs_h + (1 - 2\sigma){}^cs_{33}F(a,\xi)]}{1 + {}^cs_{33}YF(a,\xi)}$$

$$\times F(a,\xi),$$
(2.13)

where ${}^cs_h = {}^cs_{33} + 2{}^cs_{11}$ is the hydrostatic elastic compliance of the PZT rod, and a is the PZT rod radius. Hence, in the dilute limit, the hydrostatic piezoelectric constant d_h in the composite is related to the piezoelectric constant ${}^cd_{ij}$ of the PZT rod by the equation

TABLE II Hydrostatic piezoelectric charge constant for 1-3 composites with a 5% PZT volume content In the calculation ${}^cd_{33} = 590$ pC/N and ${}^cd_h = 45$ pC/N are used

$Y{}^cs_{33}$	$a = 0.3$ mm		$a = 0.5$ mm	
	0.02	0.1	0.02	0.1
ξ	d_h (pC/N)			
1.0	106	55	60	39
0.5	51	34	24	19

$$d_h = \left[{}^cd_{33}\left(1 + (1 - 2\sigma)F(a,\xi)\right.\right.$$

$$\left.\left. - \frac{Y[{}^cs_h + (1 - 2\sigma){}^cs_{33}F(a,\xi)]F(a,\xi)}{1 + {}^cs_{33}YF(a,\xi)}\right) + 2{}^cd_{31}\right]v_0,$$
(2.14)

where v_0 is the volume fraction of PZT rods in the composite and ${}^cd_{33}$ and ${}^cd_{31}$ are the piezoelectric constants of PZT ceramics. Equation (2.14) is derived under the condition that the ceramic content in the composite is very low (dilute limit). Introducing Δ as the distance at which the polymer strain changes from $(2u/L)_0$ to $0.1(2u/L)_0$, we may define the criterion for the dilute limit in a 1-3 composite, that the distance between the two neighboring rods should be equal to or greater than $(2a + \Delta)$. For example, if the PZT rod radius is 0.25 mm, the dilute limit corresponds to about 5% or less PZT in a composite. Table II lists the d_h value calculated using Eq. (2.14) for composites with a 5% PZT rod of radius 0.3 mm and 0.5 mm. In the calculation, $\sigma = \frac{1}{3}$ is assumed for the polymer and $s_{31} = -\frac{1}{3}s_{33}$ is used for the PZT rod. The data indicate how d_h varies with PZT rod aspect ratio when the volume content of PZT is kept constant, and the effect of the polymer self-loading. The results are consistent with the existing experimental data.[8,12,13]

IV. 1-3 COMPOSITE BEYOND THE DILUTE LIMIT

When the volume content of PZT rods in a composite becomes higher, as in most practical cases, the dilute approximation is not adequate in calculating the stress transfer properties between the PZT rods and polymer matrix. For a 1-3 composite as schematically drawn in Fig. 1, to solve the exact solution for the strain profile in the composite under either an electric field or a stress field can be quite involved, albeit it is not impossible. To avoid this complication and as a first-order approximation, we assume the solution for a 1-3 composite is a linear superposition of the solution in the dilute limit. Normally, the radius of the PZT rod used in 1-3 composites ranges from 0.1 to 0.5 mm, and as has been shown in the preceding section, for thin PZT rods, the strain decays rapidly as the polymer phase moves away from the PZT rod. Hence, if the volume percentage of PZT in the composite is not very high ($< 20\%$), one only needs to consider the effect of the nearest neighbor PZT rods in calculating the strain profile
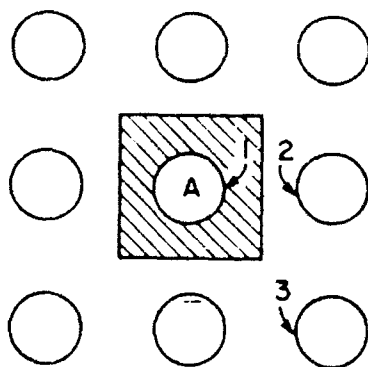
FIG. 8. Top view of a 1–3 composite. The area enclosed by the square is the unit cell and the circles are PZT rods. To calculate the polymer strain in the hatched area, only the nine PZT rods shown in the figure need to be considered if the ceramic content is less than 20%.

of the polymer phase in the hatched area of Fig. 8. Based on this consideration, the strain profile in the polymer phase of the unit cell can be approximated as

$$\left(\frac{2u}{L}\right) = A_0 \sum_{n=1}^{9} K_0\left(\frac{|\mathbf{r} - \mathbf{r}_n|}{\xi}\right), \tag{3.1}$$

where the summation is over the nine PZT rods shown in Fig. 8 and $\mathbf{r}_i$ is the center position of the ith rod. A_0 is the normalization factor, which will be determined from the boundary conditions that the strain at the polymer–PZT rod interface is equal to that of the PZT rod and all the PZT rods have the same strain level. It is clear that Eq. (3.1) cannot meet these conditions and A_0 determined from different boundary points will be different. However, it can be shown that even for a composite containing 20% PZT, the variation of A_0 calculated from different boundary points is less than 10%. Within this error, Eq. (3.1) can be used to describe the strain profile of the polymer phase in the unit cell containing the PZT rod A. To account for the variation of A_0 at a different boundary point, A_0 is calculated at points 1, 2, and 3 of the PZT–polymer boundary. This gives three different A_0 and the final value of A_0 is the averaged one over these three values,

$$A_0 = \left(\frac{1}{3}\right)\left(\frac{2u}{L}\right)_0\left(\frac{1}{L_1} + \frac{1}{L_2} + \frac{1}{L_3}\right), \tag{3.2}$$

where $(2u/L)_0$ is the strain of the PZT rod and $L_i = \sum_{n=1}^{9} K_0(|\mathbf{a}_i - \mathbf{r}_n|/\xi)$, $\mathbf{a}_i$ is the coordinate vector of the point labeled i in Fig. 8. From the results in Sec. III, d_{33} and d_h for the composite are, respectively,

$$d_{33} = v_0[1 + A(a,\xi)]/[(1 + {}^c s_{33}Y)A(a,\xi)]{}^c d_{33}, \tag{3.3}$$

$$d_h = \left\{ {}^c d_{33}\left(1 + (1 - 2\sigma)A(a,\xi) \right.\right.$$
$$\left.\left. - \frac{Y[{}^c s_h + (1 - 2\sigma){}^c s_{11}A(a,\xi)]A(a,\xi)}{1 + {}^c s_{33}YA(a,\xi)}\right) + 2{}^c d_{31}\right\}v_0. \tag{3.4}$$

the meaning of each quantity is the same as that in Eq. (2.14), except $A(a,\xi)$, which is defined as

$$A(a,\xi) = \frac{A_0}{\pi a^2} \sum_{n=1}^{9} \int_A K_0(|\mathbf{r}_n - \mathbf{r}|)dx\,dy, \tag{3.5}$$

where the integration is over the hatched area in Fig. 8. By assuming the strain in the polymer phase a constant, the above equations can be reduced to that derived earlier using the equal-strain approximation.[14]

Here d_h is calculated for 1–3 composites made of PZT-5A and spurs epoxy using Eq. (3.4). The parameters used in the calculation are obtained from the available literature.[15] For a 1–3 composite with 10% PZT volume content and the rod radius $a = 0.3$ mm, the d_h values calculated are 55, 35, and 20 pC/N, respectively, for a sample thickness of $L = 4$, 2, and 1 mm. These numbers are comparable with the experimental values: 61, 32, 17 pC/N measured by Klicker for composites with the corresponding material parameters.[8] For the composites with a higher volume fraction of PZT, the agreement between the theory and experiment becomes less satisfactory. This is what is expected from the assumption of this model.

V. CONCLUSIONS

In this paper, using the force equilibrium condition an elastic model is introduced to describe the deformation of 1–3 type composites under different driving conditions. Based on this, the effects of PZT rod aspect ratio, polymer shear and Young's moduli, as well as the spacing between PZT rods on the elastic coupling between the two components and the performance of composites are analyzed quantii tively. The theoretical results are in good agreement with experimental observations. Furthermore, using a double beam ultradilatometer, the strain profiles of several composites with simple structures were measured and the results can be described quite well by the theoretical predicted profiles. It is also shown that the strain profile measured in this manner can be used to describe the deformation of composites under a uniaxial or hydrostatic pressure.

[1] R. E. Newnham, D. P. Skinner, and L. E. Cross, Mat. Res. Bull. 13, 525 (1978).
[2] R. E. Newnham, L. J. Bowen, K. A. Klicker, and L. E. Cross, Mat. Eng. 2, 93 (1980).
[3] T. R. Gururaja, A. Safari, R. E. Newnham, and L. E. Cross, in Electronic Ceramics, edited by L. M. Levinson (Marcel Dekker, New York, 1987), Vol. 92.
[4] W. A. Smith and B. A. Auld, IEEE Trans. Ultrason. Ferroelectrics. Freq. Controls 38, 40 (1991).
[5] W. A. Smith and A. A. Shaulov, Ferroelectrics 87, 309 (1988).
[6] G. Hayward and J. A. Hossack, J. Acoust. Soc. Am. 88, 599 (1990).
[7] B. A. Auld, H. A. Kunkel, Y. A. Shui, and Y. Wang, Proc. 1983 IEEE Ultrason. Symp. 554 (1983).
[8] K. A. Klicker, Ph.D. thesis, The Pennsylvania State University, 1980.
[9] W. A. Smith, Proc. 1990 IEEE Ultrason. Symp. 145 (1990).

[10] Q. M. Zhang, S. J. Jang, and L. E. Cross, J. Appl. Phys. 65, 2808 (1989).

[11] W. Cao, Q. M. Zhang, and L. E. Cross, IEEE Trans Ultrason. Ferroelectrics., Freq. Controls (in press).

[12] T. R. Gururaja, Ph.D. thesis, The Pennsylvania State University, 1984.

[13] The d_h values measured on the samples provided by FMI, Maine

[14] M. J. Haun and R. E. Newnham, Ferroelectrics 68, 123 (1986)

[15] In the calculation, $\sigma = \frac{1}{3}$ for the polymer phase and $'s_{12} = \frac{1}{3} 's_{11}$ for PZT rods are assumed; other parameters used in the calculation are from the data sheet of Morgan Matroc Inc. and Refs 8 and 12

1410   J. Appl. Phys., Vol 73, No. 3, 1 February 1993

Zhang et al.   1410

APPENDIX 35

STRAIN PROFILE AND PIEZOELECTRIC PERFORMANCE OF PIEZOCOMPOSITES WITH 2-2 AND 1-3 CONNECTIVITIES

Q. M. Zhang, Wuewu Cao, H. Wang, and L. E. Cross
Materials Research Laboratory, The Pennsylvania State University
University Park, PA 16802

Abstract: The piezoelectric performance of 1-3 type composite depends critically on the stress transfer between the two constituents phases. This paper presents the results of our recent investigation on the elastic and piezoelectric behaviors of composites with 2-2 and 1-3 connectivities. By taking into account the nonuniform strain profiles in the constituent phases, the theoretical model presented can quantitatively predict the performance of these composites. Theoretical predictions agree quantitatively with the experimental results.

Introduction

The quantitative study of the performance of piezoceramic-polymer composites is an interesting and challenging problem. In the past, a great deal of studies have been devoted to this subject.[1-3] Nevertheless, most of these studies are based on the effective medium theory, where the material properties in each constituent phase are assumed to be uniform, and the effective material parameters of a composite are calculated using either the parallel model (Voigt averaging) or series model (Reuss averaging). Although these studies provided general guidelines in predicting the composite properties, the quantitative predictions of the effective material parameters deviate from the experimental observations in most cases.

In this paper, we will present the results of our recent study on piezoceramic-polymer composites with 2-2 and 1-3 type connectivity.[4-6] Since the most important factor of a composite structure is the stress transfer between the two constituent phases, the key to establish a working model for the composites is to understand how this stress transfer is realized. Illustrated in figure 1 is a 2-2 composite structure in which the ceramic plates and polymer are arranged parallel with each other. When subjected to a uniaxial stress, the composite will deform as illustrated by the dashed lines in figure 1(b). For comparison, we have also plotted in the same figure the deformation profile assuming no elastic coupling between the two constituent phases. The effectiveness of the stress transfer between the two phases depends on how much the strain in the polymer phase differs in the two situations [the area between the dash-dotted line and the dashed line in figure 1(b)]. This is determined by the elastic properties of the constituent phases and geometric factors of the composite. Clearly, the stress transfer in the composite is through the shear force and the strain in both phases is not uniform. When the strain is uniform in the composite, there is a maximum stress transfer between the two phases. This is the base for the isostrain model. However, to achieve that situation,

the shear modules of the polymer phase needs to be infinity, which is not practical. This explains why the theoretical calculations based on the isostrain model always overestimate the piezoelectric response of composites. Shown in figure 2 is the strain profile for a 1-3 composite manufactured by Fiber Materials, Inc.. The strain profile was measured by the double beam laser interferometer. Clearly, the strain in the polymer phase is much smaller than that expected from the isostrain model. The major advance of our model is to take into account this nonuniformity of the strain profile in the constituent phases explicitly. Therefore, this model can make quantitative predictions on the dependence of the effective material properties of a composite on the properties of its constituent phases and the sample geometric factors.
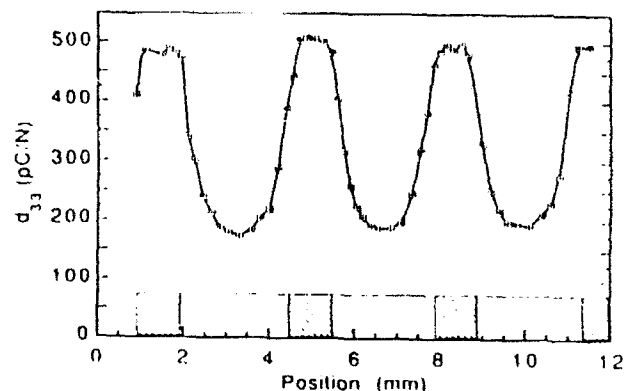
Figure 2: Strain profile for a 1-3 composite measured by the double beam laser interferometer. Hatched regions are PZT rods

The strain profile in 2-2 composites

The cross section of a 2-2 lamellar ceramic-polymer composite is shown in figure 3, where a and d are the dimensions of the ceramic plate and the polymer respectively in the x-direction, and L is the thickness of the composite in the z-direction. The dimension of the composite in the y-direction is much larger than L, a and d.

Under a uniaxial stress T_3, both the polymer and the ceramic are either stretched or compressed depending on the sign of T_3. From symmetry consideration, the z=0 plane (mirror plane) does not move at all in the z-direction. In the near static case, one can assume the strain to be uniform in the z-direction for any given x.

Taking a segment as shown in figure 3 with unit length in the y-direction (h=1), the total shear force in the z-direction fs is

$$fs = (1/4) \mu\, u_{xx}(x, L/2)\, dx$$

where u(x, L/2) is the displacement profile at the top surface of the polymer, μ is the shear modulus of the polymer. In the x-direction the composite can move freely and the stress component in this direction is therefore zero. In the y-direction, the polymer is bounded by the ceramic plates and the total stress in this direction is lumped into T_2 since we are not interested in the details of this stress component. From these conditions, one can write down the constitutive relations for this elastic body:

$$\frac{2\,u(x,L/2)}{L} = s_{33}(\frac{L}{4}\mu\, u_{xx}(x, L/2) + T_3) + s_{32} T_2 \qquad (1a)$$

$$S_2 = s_{22} T_2 + s_{32}(\frac{\mu L}{4} u_{xx}(x,L/2) + T_3) \qquad (1b)$$

where S_2 is the y component of the strain in the polymer phase, s_{ij} is the elastic compliance. For the polymer, one has the relations: $s_{22}=s_{33}$ and $s_{32}/s_{33}=-\sigma$, where σ is the Poisson's ratio. For a 2-2
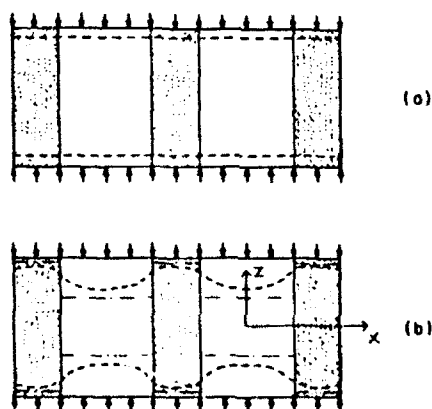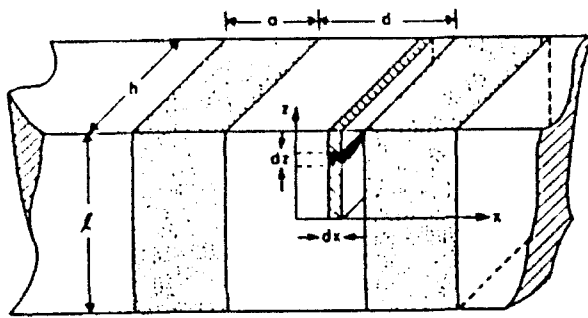

Figure 1: Schematic drawing of the 2-2 composite: (a) strain profile (dashed line) of the composite from the isostrain model when subjected to a uniaxial stress; (b) real strain profile (dashed line).

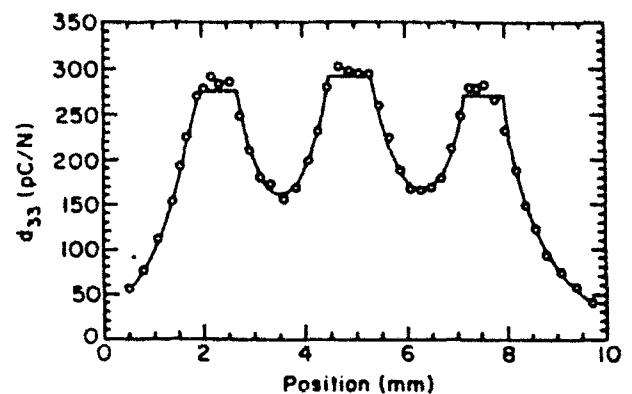Figure 3: A section of 2-2 composite for our analysis.

Figure 4: Comparison between the experimentally measured strain profile (dots in the figure) of a 2-2 composite and the theoretical curves (solid lines).

composite with its y-dimension much larger than L, a and d, S_2 is practically a constant and is independent of x. That is, the strain in this direction can be modelled by the isostrain approximation. Combining eqs (1a) and (1b) to eliminate T_2 yields

$$\frac{2u(x, L/2)}{L} = s_1(1-\sigma)\frac{1}{4}\mu u_{xx}(x, L/2) + s_{11}(1-\sigma)T_3 - \sigma S_2 \qquad (2)$$

If one neglect the stress effect in the y-direction, eq. (1) will be reduced to

$$\frac{2u(x,L/2)}{L} = s_{11}\frac{L}{4}\mu u_{xx}(x, L/2) + s_{11}T_3 \qquad (3)$$

Hence, the effect of the y-direction stress on the strain in the z-direction is to modify the elastic compliance s_{11} to $s_{33}(1-\sigma^2)$ and to add an additional constant term (Poisson's ratio effect) in the equation. It does not affect the functional form of the equation. Considering the fact that both T_3 and S_2 are constants, we can make variable substitution: $v=u+(L/2)(\sigma s_2 - s_{11}(1-\sigma^2)T_3)$ and equation (2) becomes

$$\frac{2v(x, L/2)}{L} = s_{33}(1-\sigma^2)\frac{L}{4}\mu v_{xx}(x, L/2) \qquad (4)$$

Therefore, the strain profile in the polymer phase between the two neighboring ceramic plates is

$$\frac{2u}{L} = A \cosh(2\frac{x}{L}\sqrt{2Y/(\mu(1-\sigma^2))}) + \frac{T_3}{Y} \cdot \sigma S_2 \qquad (5)$$

where A is the integration constant, $Y=1/s_{33}$ is the Young's modulus of the polymer phase. $x=0$ is at the center of the polymer filling. A can be determined from the boundary condition: $A=$

$(2u_0/L - T_3/Y + \sigma S_2)/\cosh(\frac{d}{L}\sqrt{2Y/(\mu(1-\sigma^2))})$, where $2u_0/L$ is the strain in the polymer-ceramic interface. For the situation when there is only one ceramic plate in the composite, the longitudinal strain of the polymer phase is

$$2u/L = B \exp(-\frac{(x-a/2)2}{L}\frac{d}{L}\sqrt{2Y/(\mu(1-\sigma^2))}) + \frac{T_3}{Y} \cdot \sigma S_2 \quad (x>a/2)$$

and $\qquad (6)$

$$2u/L = B \exp(\frac{(x-a/2)2}{L}\frac{d}{L}\sqrt{2Y/(\mu(1-\sigma^2))}) + \frac{T_3}{Y} \cdot \sigma S_2 \quad (x<-a/2)$$

where $x=0$ is set at the center of the ceramic plate.

To compare with the theory, several 2-2 composites were made using PZT-5A plates embeded in spurs epoxy matrix. The longitudinal strain $S_3=2u/L$ of the sample was mapped out along a path parallel to the x-axis (refer to figure 1) using the double beam laser interferometer. Presented in figure 4 is the profile taken from one of these scans. The solid line in the figure is the fitting using eq. (5) for the polymer regions between the PZT plates and eq. (6) at the two edges of the sample. Clearly, the theoretical curve describes the data quite well. From fitting the data, one can obtain the value of $Y/(\mu(1-\sigma^2))=3.35$. For an isotropic medium, we have the relationship $Y/\mu = 2(1-\sigma)$. Therefore, from the value of $Y/(\mu(1-\sigma^2))=3.35$, we can derive $\sigma=0.4$, which is a reasonable

value for the spurs epoxy used.

Single rod 1-3 composite

Although the basic stress transfer mechanism between the two constituent phases in a 1-3 type composite is similar to that in the 2-2 type, the problem of solving the strain profile in a regular 1-3 composite is more involved and may be calculated numerically. Here we will only treat one special case, a single rod 1-3 composite subjected to a hydrostatic pressure, to show quantitatively how various parameters affect the performance of a 1-3 composite. The single rod composite is schematically drawn in figure 5, where a cylindrical coordinate system is used. This configuration is a reasonable approximation to the composite with triangularly arranged ceramic rods (for which the unit cell has hexagonal symmetry) and at low ceramic content, the results here could even be used for composites with other rod arrangements.[6]
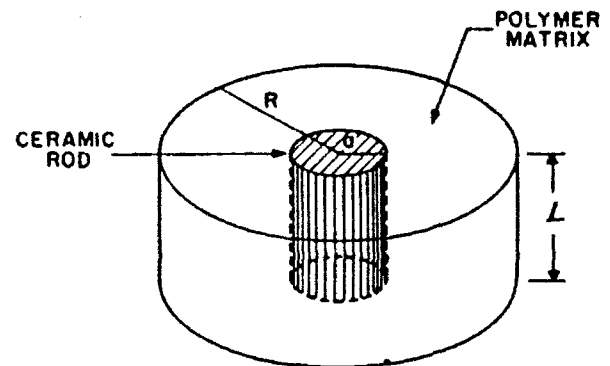
Figure 5: Schematic drawing of a single rod 1-3 composite.

Similar to the 2-2 composite situation, the force equilibrium condition for the polymer phase can be written in the following form[6]

$$\frac{\mu L}{4}(u_r(r, L/2) + \frac{u_r(r,L/2)}{r}) \cdot (1-2\sigma) p = \frac{2 Y u(r, L/2)}{L} \qquad (7)$$

where the meaning of each quantity is similar to that in the preceding section and p is the hydrostatic pressure. One can write down similar equation for the strain profile in the ceramic rod. The strain profile for the polymer phase is therefore given by

$$2u/L = A K_0(r/\xi) + B I_0(r/\xi) - (1-2\sigma) p/Y \qquad (8)$$

where $K_0(\rho)$ and $I_0(\rho)$ are zeroth order modified Bessel functions. A and B can be determined from the boundary conditions. From the

253

strain profile, one can calculate the stress transfer between the two constituent phases and hence the effective piezoelectric hydrostatic strain constant d_h:

$$d_h = V_c (\gamma_h d_{33}^c + 2 d_{31}^c)$$ (9)

where V_c is the volume content of the ceramic in the composite, d_{33}^c and d_{31}^c are the piezoelectric constants of the ceramic phase, and γ_h is the stress amplification factor:[6]

$$\gamma_h = 1 + \frac{\frac{L}{a} I_1(\rho_R) [I_1(\rho_R) K_1(\rho_a) - I_1(\rho_a) K_1(\rho_R)][(1-2\sigma)/Y - (1-2\sigma^c)s_{33}^c]}{\sqrt{\frac{2s_{33}}{c_{44}}} I_0(\rho_a)[I_1(\rho_R) K_1(\rho_a) - I_1(\rho_a) K_1(\rho_R)] + \sqrt{\frac{2}{Y\mu}} I_1(\rho_a)[I_1(\rho_R) K_0(\rho_a) + I_0(\rho_a) K_1(\rho_R)]}$$ (10)

where s_{33} and c_{44} are the elastic compliance and the shear constant of the ceramic, σ^c is the Poisson's ratio of the ceramic,

$$\rho_f = (2 \ r/L) \sqrt{\frac{2Y}{\mu}} \text{ and } \rho_r^c = (2 \ r/L) \sqrt{\frac{2}{s_{33}^c c_{44}}}$$ One can see that

the stress amplification factor depends on the elastic properties of the constituent phases and most importantly, on the aspect ratio of the ceramic rod. Plotted in figure 6 is the calculated results for d_h from eq. (9) for several different aspect ratios for a PZT5H-Spurs epoxy composite. The input data can be found in reference 6. Clearly, aspect ratio of the PZT rod is an important parameter in determining the piezoelectric performance of 1-3 composites.

Shown in figure 7 is the comparison between the experimentally measured d_h for a 1-3 composite with 1% PZT volume content in spurs epoxy matrix and that calculated from equation (9). The parameters used in the calculation are listed in reference 6, and d_{33} and d_{31} were treated as fitting parameters. The agreement between the experimental result and theoretical calculation is satisfactory.
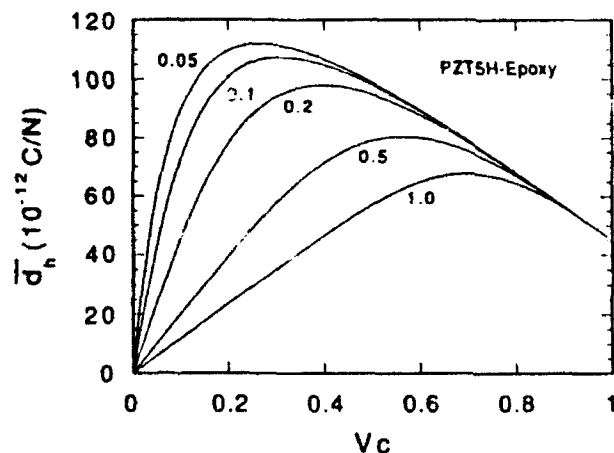
Figure 6: The hydrostatic piezoelectric constant d_h, as a function of the ceramic content at the aspect ratio of a/l =0.05, 0.1, 0.2, 0.5 and 1.0 for a single rod PZT5H-Epoxy 1-3 composite.

Conclusions

In general, the response of the constituent phases of a composite to an external field is not uniform spatially. By taking into account the nonuniform strain profiles in the constituent phases, the theoretical model presented in this paper can quantitatively predict the performance of these composites. Theoretical predictions agree quantitatively with the experimental results.
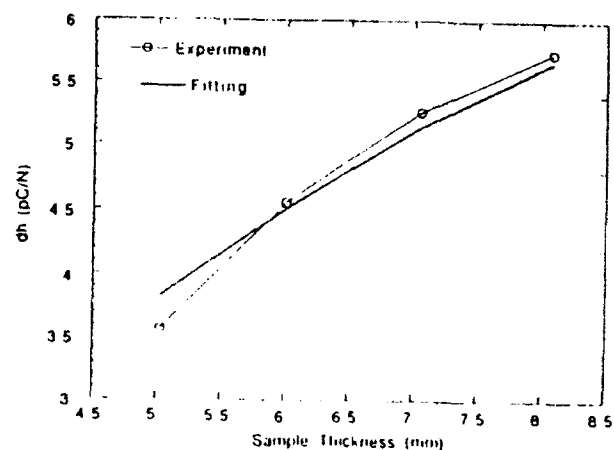
References

[1] Newnham, R. E., D. P. Skinner, and L. E. Cross, "Connectivity and Piezoelectric-Pyroelectric Composites," Materials Res. Bull, vol 13, pp. 525-536, 1978.

[2] Gururaja, T. R., A. Safari, R. E. Newnham, and L. E. Cross, "Piezoelectric Ceramic-Polymer Composites for Transducer Applications," in Electronic Ceramics, ed. L. M. Levinson, pp 92-128, New York: Marcel Dekker,1987.

[3] Smith, W. A., B. A. Auld, "Modeling 1-3 Composite Piezoelectrics: Thickness-Mode Oscillations," IEEE Trans on Ultrasonics, Ferro., and Freq. Control, vol 38, pp. 40-47, 1991.

[4] Wenwu Cao, Q.M. Zhang, and L. E. Cross, " Theoretical Study on the Static Performance of Piezoelectric Ceramic-Polymer Composites with 2-2 Connectivity," IEEE Trans. Ultrasonics, Ferro., and Freq. Control, in press, 1992

[5] Q. M. Zhang, Wenwu Cao, H. Wang, and L. E. Cross, "Characterization of the Performance of 1-3 Type Piezocomposites for Low Frequency Applications," submitted to J. Appl. Phys., 1992.

[6] Wenwu Cao, Q. M. Zhang, and L. E. Cross, "Theoretical Study on the Performance of Piezoelectric Ceramic-Polymer Composites with 1-3 Connectivity," accepted by J. Appl. Phys., 1992

APPENDIX 36

Piezoelectric tubes and 1-3 type tubular composites as tunable actuators and sensors

Q. M. Zhang, H. Wang, and L. E. Cross

Materials Research Laboratory, The Pennsylvania State University
University Park, PA 16802

ABSTRACT

The piezoelectric actuators and sensors made of tubular structure can provide a great agility of the effective response in the radial direction. For a radially poled piezoelectric tube, the effective piezoelectric constant in that direction can be tuned to be positive, zero, and negative by varying the ratio of the outer radius (R_0) to the inner radius (r_0) of the tube. For a suitable ratio of R_0/r_0, this effective constant can also be changed in sign or set to zero by adjusting the DC bias field level for tubes made of electrostrictive materials. Therefore, one can make a piezoelectric transducer with all the effective piezoelectric tensile constants having the same sign. The end capped thin wall tubes also exhibit exceptionally high hydrostatic response and the small size of the tubular structure makes it very suitable for integration into 1-3 composite which possesses low acoustic impedance and high hydrostatic response.

1. INTRODUCTION

The recent advance in the adaptive materials and structures has put increasing demands on new materials and material structures to broaden the range of material properties provided by the conventional materials. [1,2] By integration of several materials into a composite or by structure modification, one can greatly improve the performance of devices. In this paper, we will examine the effective piezoelectric properties of a tubular structure and its composites formed from arrays of such tube for both actuating and sensing applications. We will show that for a radially poled ceramic tube, the competition between the piezoelectric d_{33} effect and d_{31} effect in the radial direction provides a convenient way to adjust the effective piezoelectric properties in that direction by changes in the tube radii. The small thickness of a thin wall tube also makes it practical to use field biased electrostrictive materials for actuators and sensors since only a low terminal DC voltage is required to produce substantial piezoelectric activities in the materials in this geometry and by adjusting the DC bias field level, the effective piezoelectric constant in the radial direction can be tuned from positive to zero, and to negative.

2. PIEZOELECTRIC RESPONSE OF A TUBE UNDER AN ELECTRIC FIELD

When a radially poled tube is subjected to an electric field along the radial direction, on the average, the strain in the axial direction equals $d_{31} E_m$, where d_{31} is the linear piezoelectric constant and E_m is the average field in the material. The dimensional change in the radial direction, however, is complicated. In this section, the solution of the elastic equation for the tubular structure under an electric field will be presented. It will be shown that with the same applied electric field, the outer diameter (OD) of the tube can either expands or contracts depending on the ratio of the OD to ID of the tube. This phenomenon is the direct consequence of the competition between the piezoelectric d_{33} and d_{31} effects which have opposite sign in producing the change in the tube OD under electric field.

For a tubular structure, it is convenient to use the cylindrical polar coordinate system, as shown in figure 1, in the analysis of the strain response of the sample under an electric field. The symmetry of
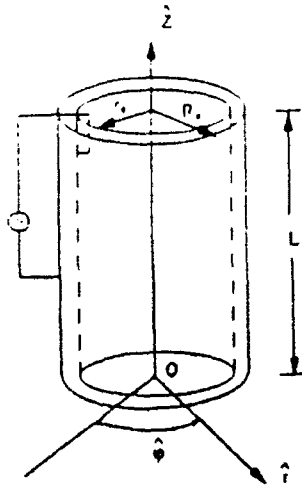
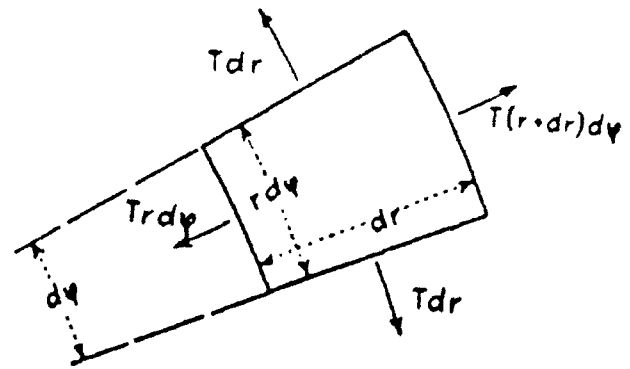Figure 1: Schematic drawing of a radially poled ceramic tube with the outer radius R_0 and inner radius r_0.

Figure 2: Forces on a segment of a tube in the plane perpendicular to the tube axis(z).

the problem requires that the ϕ-component of the displacement field $u_\phi=0$. For a thin wall tube, one can neglect the coupling terms containing both r and z in the displacement field $\vec{u}$ and assume $\vec{u}=u_r(r)\,\hat{r} + u_z(z)\,\hat{z}$ Under this approximation, the non-zero strain component are:

$u_{rr}=\dfrac{\partial u_r}{\partial r}$, $u_{\phi\phi}=\dfrac{u_r}{r}$, and $u_{zz}=\dfrac{\partial u_z}{\partial z}$. The constitutive relations for the tube, therefore, are

$$T_z= c_{11} u_{zz} +c_{12} u_{\phi\phi}+c_{12} u_{rr}-e_{31}E$$
$$T_r = c_{11} u_{rr} +c_{12} u_{\phi\phi}+c_{12} u_{zz}-e_{33}E \qquad (1)$$
$$T_\phi=c_{12} u_{zz} +c_{11} u_{\phi\phi}+c_{12} u_{rr}-e_{31}E$$

where T_z, T_r, and T_ϕ are the stress components in the three directions, c_{ij} is the elastic stiffness constant, e_{ij} is the piezoelectric stress constant, and E is the applied electric field on the tube wall along the r-direction. It is well known that the electric field is not a constant inside the tube wall and with a total voltage V applied on the tube, $E=\dfrac{V}{r\ln (R_0/r_0)}$ ($r_0 \leq r \leq R_0$). In writing down equation (1), we also made the approximation that the tube is isotropic elastically to simplify the analysis. The nonisotropic case will be addressed in the next section when we discuss the hydrostatic response of the end capped tubes. Both the experimental results which will be presented later in this section and the analysis in the next section show that the errors due to the isotropic approximation are not significant.

For a tube segment shown in figure 2, from the force balance consideration under the static condition, one can arrive at

$$\frac{\partial T_r}{\partial r} + \frac{T_r - T_\phi}{r} = 0 \qquad (2)$$

Making use of the constitutive equation (eq. (1)), the basic elastic equations for this problem are

$$\frac{\partial}{\partial r}(\frac{1}{r}\frac{\partial}{\partial r}ru) = -\frac{e_{31}E}{r}\frac{s_{11}(1+\sigma)(1-2\sigma)}{1-\sigma} \qquad (3)$$

$$\frac{\partial u_z}{\partial z} = \text{constant}$$

where σ is the Poisson's ratio and s_{11} is the elastic compliance. The solutions to eq. (3) are

$$u_r = ar + \frac{b}{r} + \frac{e_{31}V}{\ln\rho}\frac{s_{11}(1+\sigma)(1-2\sigma)}{1-\sigma} \qquad (4)$$

and $\qquad u_z = c\,z$

where $\rho = R_0/r_0$. a, b and c are the integration constants and can be determined from the boundary

conditions: $u_{zz} = d_{31}E_m$, where E_m is the average electric field in the tube ($E_m = \dfrac{2V}{(R_0+r_0)\ln(R_0/r_0)}$), and

at $r = R_0$ and r_0, there is no external stress on the tube wall which implies $T_r = 0$ at these two boundaries. Substituting eq. (4) into eq. (1) and using the boundary conditions, one can get

$$a = E_m ((1-2\sigma) d_{33} - \sigma d_{31})/(2(1-\sigma))$$
$$b = - R_0\, r_0\, E_m\, (d_{33} + \sigma\, d_{31})/(2(1-\sigma)) \qquad (5)$$
$$c = d_{31}\, E_m$$

In deriving eq. (5), we have used relation $e_{31} = c_{11}d_{31} + c_{12}(d_{31}+d_{33})$. All the strain components for the tube can be obtained from eqs. (4) and (5). Here we are more interested in finding out how the tube outer diameter changes with applied electric field as the ratio of R_0/r_0 varies since in most of the applications, this is the quantity of interests. Substituting a and b in equation (4) into the expression for u_r and setting $r = R_0$ yield the displacement of the tube outer wall $u_r(R_0)$

$$u_r(R_0) = Em\, ((R_0+r_0)\, d_{31} + (R_0 - r_0)\, d_{33})/2$$

This equation reveals that $u_r(R_0)$ can be changed from positive to zero, and to negative by varying the ratio of R_0/r_0.

To illustrate the advantage of using thin wall tube for actuator applications, one can compare the piezoelectric response of a tube discussed here with a rod of radius R_0 and length L subjected to the same applied voltage V. For the rod, the field is applied along the axial direction and $u_{zz} = d_{33}\, V/L$ and $u_{rr} = d_{31}\, V/L$. For the tube sample, one can equivalently introduce the quantity u_r/R_0 as the effective strain in the radial direction

$$u_r(R_0)/R_0 = Em\, ((1+r_0/R_0)\, d_{31} + (1 - r_0/R_0)\, d_{33})/2 \qquad (6)$$

Similar to a rod sample, we introduce the effective piezoelectric constants for the tube as if it were a rod poled axially,

$$u_{zz} = d_{33}^{eff} V/L \quad \text{and} \quad \frac{u_r}{R_0} = d_{31}^{eff} V/L \quad (7)$$

where L is the axial length of the tube and V is the voltage applied on the tube wall. From $u_{zz} = d_{31} E_m$ and equation (6), the effective piezoelectric constants can be deduced

$$d_{33}^{eff} = d_{31} \frac{2L}{(R_0 + r_0) \ln(R_0/r_0)} \quad (8)$$

$$d_{31}^{eff} = \frac{L}{(R_0 + r_0) \ln(R_0/r_0)} [(1 + \frac{r_0}{R_0}) d_{31} + (1 - \frac{r_0}{R_0}) d_{33}]$$

For thin wall tubes with L much larger than R_0, which is the case in most of the applications, both d_{33}^{eff} and d_{31}^{eff} can be exceptionally large. This demonstrates that the tubular structure has great advantage over the regular ceramic rod for actuator application. Besides that, by choosing $(1 + r_0/R_0) |d_{31}| > (1 - r_0/R_0) |d_{33}|$, the effective d_{33} and d_{31} of the tube will have the same sign. By adjusting the ratio R_0/r_0, one can also continuously vary d_{31}^{eff} of the tube from positive to zero and to negative.

To compare with the theoretical prediction, the displacement field $u_r(R_0)$ and u_{zz} of a radially poled PZT-5 tube were measured using a double beam laser dilatometer.[3] The ceramic tubes used were manufactured by Morgon Matroc, Inc., Vernitron Div. with $R_0 = 0.635$ mm and $r_0 = 0.381$ mm. From the data acquired and using eqs (4), (5) and (6), we get $d_{33} = 289$ pC/N and $d_{31} = -141.3$ pC/N for the tube material. For most of commercially available PZT materials, the ratio of d_{33}/d_{31} ranges from 2.15 to 2.3.[4] The measured ratio here ($d_{33}/d_{31} = 2.05$) is slightly below that range which we believe is the result of the approximations used in the derivation. The effective piezoelectric constants defined in eq. (7) for the tube, therefore, are $d_{33}^{eff} = -8180$ pC/N and $d_{31}^{eff} = -3220.5$ pC/N, the two coefficients have the same sign as predicted by eq. (8) and they are exceptionally large.

The small thickness of the tube wall also makes it possible to use electric field biased electrostrictive materials for the actuator application since only a small bias voltage is required here to induce substantial piezoelectric responses in the materials. Shown in figure 3 is the DC field induced piezoelectric constants of lead magnesium niobate (PMN)-lead titanate (PT) with a composition of 0.9PMN-0.1PT (the data is taken from ref. 5). Clearly, the ratio of the piezoelectric constants d_{33}/d_{31} for this material is bias field dependent. At the bias field level 1 kV/cm, $d_{33} = 400$ pC/cm and $d_{31} = -200$ pC/cm, while at the bias field 3 kV/cm, $d_{33} = 1000$ pC/cm and $d_{31} = -400$ pC/cm. In figures 4(a) and 4(b), we show how d_{33}^{eff} and d_{31}^{eff} of a tube made of this material will vary as the ratio of r_0/R_0 changes for these two cases. It can be seen that the cross-over points where d_{31}^{eff} changes sign are different for the two cases. Hence, for a suitable ratio of r_0/R_0, by tuning the DC bias field level, both sign and magnitude of d_{31}^{eff} of the tube can be varied. In figure 5, the dependence of $-d_{31}^{eff}/d_{31}$ on the ratio of d_{31}/d_{33} is shown explicitly for a tube with $r_0/R_0 = 0.4$.

3. THE HYDROSTATIC RESPONSE OF END CAPPED TUBES AND 1-3 TYPE TUBULAR COMPOSITES

The availability of small size ceramic tubes makes it attractive to integrate them into 1-3 type piezoceramic-polymer composites for large area applications and to provide more flexibility for further material property modification. Before the discussion on the composite properties, we will briefly derive the expression for the hydrostatic response of end capped tubes first since this is the most commonly used mode of piezo-tubes as hydrostatic sensor.[6]
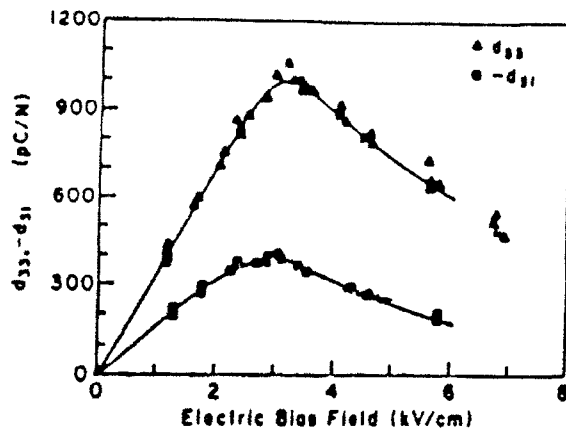
Figure 3: DC bias field induced piezoelectric constants of 0.9 PMN-0.1 PT at room temperature
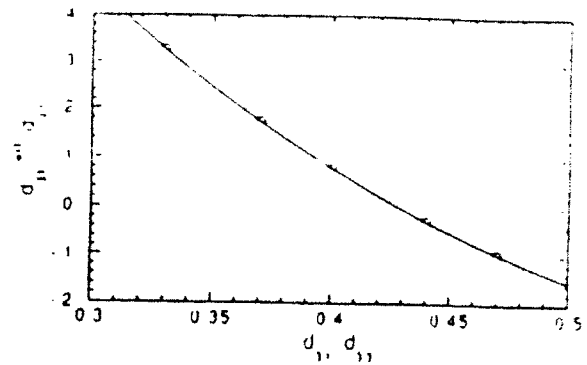
Figure 5: Dependence of d_{33}^{eff} on the ratio d_{31}/d_{33} for a tube with $r_o/R_o = 0.4$.
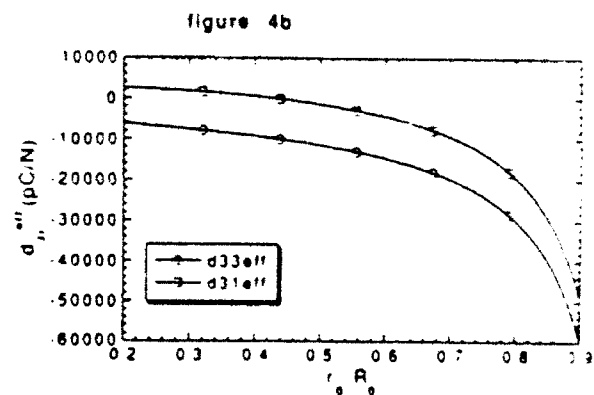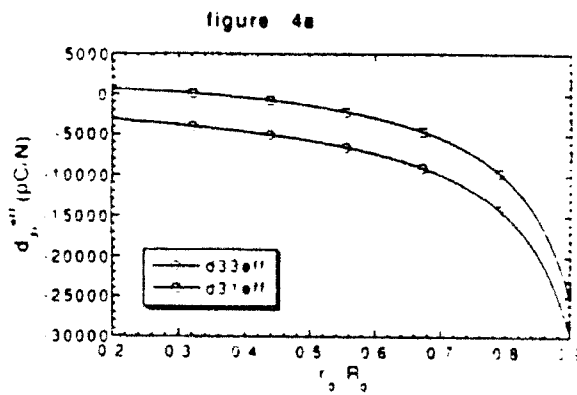
figure 4a

figure 4b

Figure 4: (a) Dependence of d_{3i}^{eff} on r_o/R_o for tubes with $d_{33} = 400$, $d_{31} = -200$ and $L/R_o = 15$; (b) with $d_{33} = 1000$, $d_{31} = -400$, $L/R_o = 0.4$.

Similar to the derivations presented in the preceding section, the displacement field of a tube under hydrostatic pressure, when expressed in the cylindrical coordinate system, is $u_\phi = 0$ and $\vec{u} = u_r(r)\,\hat{r} + u_z(z)\,\hat{z}$ (for an isotropic material, this is the exact form of the displacement field and for a poled ceramic tube, the error in using this form of the displacement field, as will be shown later, is less than 10%.) Since all the external forces are applied on the surfaces of the tube, there is no internal body force in the tube wall, eq (3) becomes:

$$\frac{\partial\, r\, u_r}{r \partial\, r} = \text{const.} \qquad \text{and} \qquad \frac{\partial\, u_z}{\partial\, z} = \text{const.} \qquad (9)$$

The solutions to the equations are:

$$u_r = a\, r + b/r \quad \text{and} \quad u_z = c\, z \qquad (10)$$

The non-zero strain components are:

$$u_{rr} = a - b/r^2, \quad u_{\phi\phi} = a + b/r^2, \quad \text{and } u_{zz} = c \qquad (11)$$

where a, b, and c are the integration constants. The boundary conditions which will be used to determine them are: since the two ends of the tube are sealed, there is no pressure inside the tube, at $r=r_0$, $T_r = 0$; at $r=R_0$, $T_r = - p$; and at $z=0$ and $z=l$, the stress in the axial direction is $T_z = - p\, R_0^2/(R_0^2 - r_0^2)$, where $- p$ is the applied hydrostatic pressure. For an anisotropic tube, the constitutive relations are:

$$\begin{aligned}
T_z &= c_{11}\, u_{zz} + c_{12}\, u_{\phi\phi} + c_{13}\, u_{rr} \\
T_r &= c_{33}\, u_{rr} + c_{13}\, u_{\phi\phi} + c_{13}\, u_{zz} \qquad (12) \\
T_\phi &= c_{12}\, u_{zz} + c_{11}\, u_{\phi\phi} + c_{13}\, u_{rr}
\end{aligned}$$

where c_{ij} are the elastic stiffness coefficients of the poled ceramics. Substituting the strain components in eq. (11) into eq. (12) and omitting the term in T_z having r dependence, one can obtain a, b, c:

$$a = \frac{- p\, R_0^2}{R_0^2 - r_0^2} \left[\frac{c_{13} - c_{11}}{c_{13}(c_{12} + c_{13}) - c_{11}(c_{13} + c_{33})} \right] \qquad (13a)$$

$$b = \frac{- r_0^2 R_0^2}{R_0^2 - r_0^2} \frac{p}{c_{33} - c_{13}} \qquad (13b)$$

$$c = \frac{- p\, R_0^2}{R_0^2 - r_0^2} \left[\frac{c_{12} - c_{33}}{c_{13}(c_{12} + c_{13}) - c_{11}(c_{13} + c_{33})} \right] \qquad (13c)$$

From eqs. (11), (12) and (13), the hydrostatic response of the tube can be calculated from the relation

$$D_3 = d_{31}\, T_z + d_{31}\, T_\phi + d_{33}\, T_r \qquad (14)$$

where D_3 is the electric displacement in the poling direction. The value of d_h can be found by taking the average charge produced in the inner and outer surfaces of the tube wall and divided it by the outer surface area of the tube. This yields from eq. (14):

$$d_h = \frac{1}{2} \left\{ d_{33} + \frac{R_0}{R_0 - r_0} \left[1 + \left(\frac{c_{13}^2 + c_{12}^2 - c_{11}^2 - c_{12} c_{33}}{c_{13}(c_{13} + c_{12}) - c_{11}(c_{13} + c_{33})} \right) + \frac{c_{11} - c_{13}}{c_{33} - c_{13}} \frac{r_0}{R_0} \right] d_{31} \right\} \qquad (15)$$

Using the elastic stiffness coefficients for PZT-5H,[4] for a tube with $R_0=0.635$ mm and $r_0=0.381$ mm, eq. (15) predicts $d_h = -657$ pC/N or 2.4 d_{31}. If the tube R_0 is doubled while keeping the wall thickness the same, the d_h value can reach -1786 pC/N. Hence, for thin wall tubes, an exceptionally large hydrostatic response can be achieved.

For an elastically isotropic tube d_h can be found by simplifying eq. (15) using the isotropic conditions $c_{11} = c_{33}$, $c_{12} = c_{13}$:

$$d_h = \frac{1}{2} \left\{ d_{33} + \frac{R_0}{R_0 - r_0} \left[2 + \frac{r_0}{R_0} \right] d_{31} \right\} \qquad (16)$$

For the PZT-5H tube just calculated, the calculated d_h value is -594 pC/N (2.17 d_{31}) when eq. (16) is

Experimental measurements were performance on several PZT-5 tubes ($R_0=0.635$ mm and $r_0=0.381$ mm) with two ends sealed and radially poled (the dielectric constant ϵ for this group of sample is around 1700 at the atmospheric pressure). d_h was measured through the direct piezoelectric effect where the charge induced on the electrodes of a sample is measured when the sample is subjected to a hydrostatic pressure. d_{31} and d_{33} were measured using the double beam laser interferometer.[3] For this group of samples, the d_h was in the range from -330 pC/N to -400 pC/N and d_{31} from -140 pC/N to -160 pC/N. The ratio between experimentally measured d_h and d_{31} (on average) is 2.45 which is very close to that predicted from eq. (15). Clearly, to make a quantitative prediction about the hydrostatic response of a tubular structure, one may be required to include the elastic anisotropy in the calculation.

In analogy to the situation discussed in the preceding section, one can also manipulate the piezoelectric response of a tube to the stress field in the radial direction by changing the ratio of r_0/R_0 for tubes made of piezoelectric materials or the DC bias field for tubes made of electrostrictive materials. Here, we will use the result just derived for the hydrostatic response of a tube as an example. In eq. (14), the hydrostatic response of a tube comes from three terms, one is from the pressure in the axial direction and the other two from the pressure in the radial direction. The electric displacement D_3^r due to the pressure in the radial direction is

$$D_3^r = d_{31} T_\phi + d_{33} T_r$$

Hence, the partial piezoelectric response d^r of the tube to the pressure in the radial direction is

$$d^r = \frac{1}{2} \{ d_{33} + \frac{R_0}{R_0 - r_0} [(\frac{c_{13}^2 + c_{12}^2 - c_{11}^2 - c_{12}c_{33}}{c_{13}(c_{13} + c_{12}) - c_{11}(c_{13} + c_{33})}) + \frac{c_{11} - c_{13}}{c_{33} - c_{13}} \frac{r_0}{R_0}] d_{31} \} \qquad (17)$$

Obviously, the opposite sign of d_{33} and d_{31} provides a convenient way to change d^r in eq. (17). One can easily verify that by varying the ratio of R_0/r_0, d^r changes continuously from positive to zero, and to negative. Similar to the actuator case, for suitable ratio of r_0/R_0, one can also change the sign of the effective radial response here by using electrostrictive materials with different DC bias field level. Furthermore, for a tube made of electrostrictive material, its piezoelectric response can be turned off by setting the DC bias field zero. This result as well as the result in the preceding section indicate that the range of the effective piezoelectric properties of the materials can be considerably broadened by using the tubular structures.

To calculate the hydrostatic figure of merit for this tubular sensor, we notice that in practice, the quantity $d_h g_h$ is a measure of the product of the charge and voltage produced in a unit volume material. For a tubular material, its effective volume is $\pi R_0^2 L$, where L is the tube length when the end capped tube is regarded as a rod with its radius equal to R_0. Hence, the effective figure of merit for the tube is

$$d_h g_h = \frac{1}{2\epsilon\epsilon_0} \ln(\frac{R_0}{r_0})(d_{33} + d_{31}(\frac{R_0}{R_0 r_0})(2 + \frac{r_0}{R_0}))^2 \qquad (18)$$

Here, we have used d_h result for an isotropic tube (eq (16)). One can easily expand the result to elastically anisotropic materials. Clearly, for a thin wall tube a large figure of merit can be obtained.

We now discuss the properties of 1-3 tubular composites. A typical 1-3 tubular composite is schematically drawn in figure 6. For the composite discussed here, the tubes are radially poled and the composite is electroded on the two end faces. Hence, special arrangement is required to ensure a proper electric connections between the electrodes at the tube walls and the composite end faces. This kind of composite can be used for large area actuator and sensor applications, as well as smart materials where both sensor and actuator are integrated into one structure. Here, we only discuss the properties associated with the sensor applications.
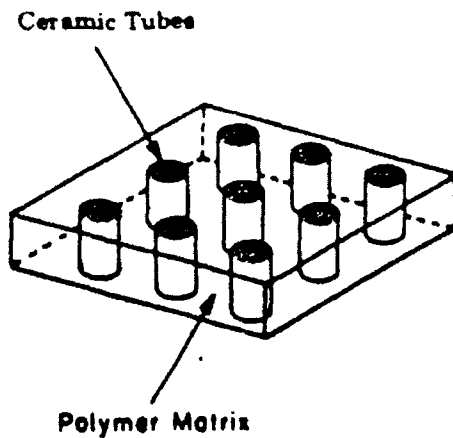
Figure 6: Schematic drawing of a
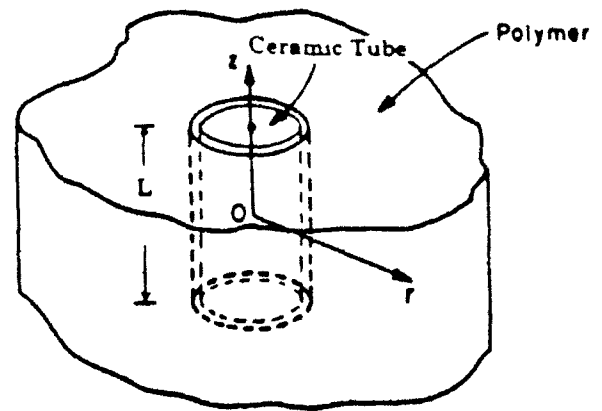1-3 tubular composite.

Figure 7: Schematic drawing of 1-3 tubular
composite with only one tube embedded in an
infinite extended polymer matrix.

When tubes are integrated into a 1-3 type ceramic-polymer composite, as has been demonstrated in our earlier publications, there is a stress transfer between the polymer matrix and the ceramic tubes in the z-direction.[7,8] This stress transfer is the result of the difference in the elastic constants between the two constituent phases and is through the shear force in the two phases. Due to this stress transfer, the piezoelectric response of the tube in the axial direction is enhanced. To provide a physical picture of how the hydrostatic response of a tubular 1-3 composite changes as the elastic properties of the two constituent phases and their geometric parameters are varied, we will treat quantitatively the composite schematically drawn in figure 7. This composite corresponds to the tubular composite in the dilute limit. However, since only the polymer matrix close to the ceramic-polymer interface participates the stress transfer, the result can also be applied to the composite with finite ceramic content.

The procedure of calculating how much stress is transferred from the polymer phase to the ceramic rod is similar to that outlined in the earlier publications.[7,8] Under hydrostatic pressure p, the surface displacement field u_z of the polymer phase in the z-direction should satisfy the following equation

$$\frac{2u_z}{L} = -(s_{11} + 2 s_{12}) p + \frac{s_1 \mu L}{4} \left(\frac{\partial^2 u_z}{\partial r^2} + \frac{\partial u_z}{r \partial r} \right) \quad (19)$$

where p is the hydrostatic pressure, s_{ij} is the elastic compliance of the polymer phase, μ is the shear modules of the polymer phase, and L is the thickness of the composite in the z-direction. The solution to eq. (19) is the zeroth-order Hankel function $K_0(\rho)$ and

$$\frac{2u_z}{L} = \frac{(1-2\sigma) p}{Y} + A K_0(r/\xi) \quad (20)$$

where A is an integration constant and $\xi = L/(2 \sqrt{2Y/\mu})$, the strain decay length in the polymer phase. In eq. (20), we have made use of the relations $s_{12} = -\sigma s_{11}$ and $Y = 1/s_{11}$, where Y and σ are the Young's modules and the Poisson's ratio of the polymer, respectively. The total force f transferred from the

polymer phase to the ceramic tube is, therefore

$$f = Y \int_{R_0}^{\infty} 2\pi \, r \, A \, K_0(r/\xi) \, dr$$

Two boundary conditions are needed to determine f. The first one is the condition that at the ceramic tube-polymer interface, the z-component of the strain in the two phases should be equal, and the second is the relation between the z-component of the strain in the ceramic tube and the stress field

$$u_{zz} = -\frac{pR_0^2(1-\sigma^c)s_{11}^c}{R_0^2 - r_0^2} + \frac{f\,s_{11}^c}{\pi\,(R_0^2 - r_0^2)} \quad (21)$$

where s_{11}^c and σ^c are the elastic compliance and the Poisson's ratio of the ceramic tube, respectively. Hence, the total stress in the axial direction of the tube is

$$T_z = -\frac{pR_0^2}{A_0}(1 + \frac{A_0(1-2\sigma)/(R_0^2 Y s_{11}^c) - (1-2\sigma^c)}{1 + K_0(\rho_0)A_0/(2K_1(\rho_0)Y s_{11}^c R_0\xi)})$$

$$= -\frac{pR_0^2}{A_0}\gamma \quad (22)$$

where γ is introduced as the stress amplification factor, $A_0 = (R_0^2 - r_0^2)$, $\rho_0 = R_0/\xi$, and $K_1(\rho)$ is the first order Hankel function. In figure 8, we plot γ as a function of the aspect ratio R_0/L for a 1-3 tubular composite made of PZT-5H tube with $R_0 = 0.635$ mm and $r_0 = 0.381$ mm and spurs epoxy.[9] Apparently, for thin and long tubes, the stress amplification factor is large. This is similar to that obtained earlier for 1-3 composites made of ceramic rods.[7,8]

Using the results from the single tube and equation (22), one can write down the effective hydrostatic piezoelectric strain coefficient for 1-3 tubular composites

$$d_h^{eff} = \frac{L}{R_0}\,v_c\,(d_{33} + \frac{R_0}{R_0 - r_0}(1 + \gamma + \frac{r_0}{R_0})d_{31}) \quad (23)$$

where v_c is the volume content of the ceramic tubes in the composite which is defined as $v_c = \pi R_0^2/a$, and a is the unit cell area of the composite. For a composite in the low ceramic volume content, γ in eq. (22) is equal to that in eq. (23). With increased volume content, the dependence γ on the material properties of the constituent phases will become more complicated and one may not be able to derive the analytical expression for γ except in some special cases. In this paper, we will not pursue this further and only point out that in the composite, there is always a stress transfer between the two phases ($\gamma > 1$), the general rule to increase this stress transfer is basically the same as that for the dilute composite case.

The effective hydrostatic figure of merit for 1-3 tubular composites is

$$d_h^{eff} g_h^{eff} = \frac{v_c}{2\varepsilon\varepsilon_0}\,\ln(\frac{R_0}{r_0})\{d_{33} + \frac{R_0}{R_0 - r_0}(1 + \frac{r_0}{R_0} + \gamma))d_{31}\}^2 \quad (24)$$

For the comparison, in table I, we present the experimental values of the hydrostatic response of an end-capped ceramic tube, a 1-3 composite with tube inside air backing, and a 1-3 composite with tube inside epoxy backing. All 1-3 composites had the volume content of 23.3 % ceramic tube and the dimensions of the tubes are: $R_0 = 0.635$ mm, $r_0 = 0.381$ mm, and $L = 9$ mm. The polymer matrix was made of spurs epoxy. In the composite with epoxy backing, the tube inside was filled with spurs epoxy. d_{31} listed in

the table was calculated using the single tube result where the ratio $d_{33}/d_{31}=2.2$ was used. From this d_{31}, γ was calculated from eq. (24). Clearly, the γ value here is much smaller than that shown in figure 8 ($R_0/L=0.07$ here). One of the reasons for this is that figure 8 is for the composite in the dilute limit, the γ value for composites with finite ceramic content should be smaller than that in figure 8. The imperfect stress transfer between the two phases and the depoling effect of the tubes during the epoxy curing may also be responsible for this reduction of γ. Although the data in table I show that the hydrostatic responses of the composites tested are not as high as that of the single tube, the different is not very large. As the volume content of the ceramic tube and other parameters in a composite are varied, the effective hydrostatic figure of merit for 1-3 tubular composites will change. In the optimum condition, one would expect that $d_h^{eff}g_h^{eff}$ for a tubular 1-3 composite may exceed that of a single tube. Apparently, further experimental and theoretical work is required to address this issue. Further more, the figure of merit of 1-3 tubular composites is much higher than that of 1-3 composites made of ceramic rods.[8]

4. SUMMARIES AND ACKNOWLEDGEMENT

In this paper, the effective piezoelectric responses of the tubular structure and its composites were evaluated both theoretically and experimentally. When used as actuators, the effective piezoelectric constant in the radial direction of a tube can be changed from positive to zero and to negative by adjusting the ratio of R_0/r_0 for piezoelectric materials or the DC bias field for electrostrictive materials. Therefore, the effective piezoelectric constants along the axial direction and the radial direction can both have the same sign. For the sensor applications, the two ends sealed tube exhibits exceptionally high hydrostatic response and analogues to the situation of actuators, the pressure response in the radial direction can be adjusted by the ratio of R_0/r_0 for piezoelectric materials or the DC bias field for the
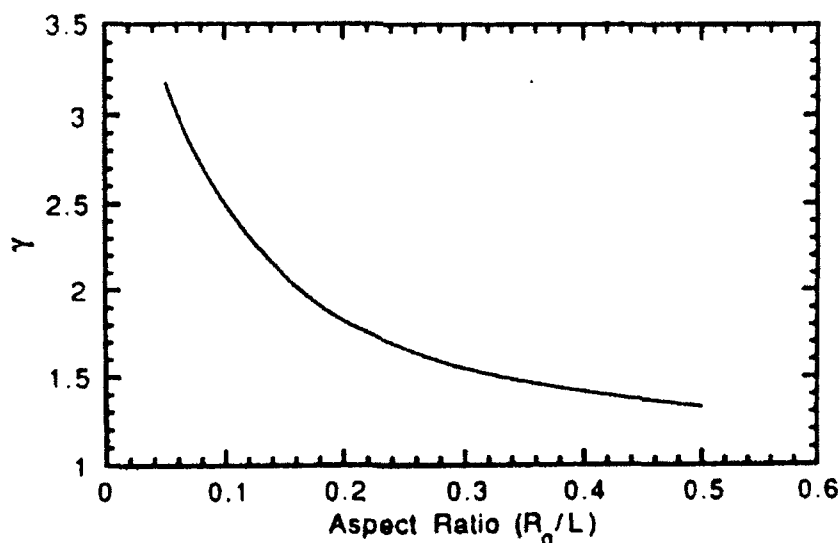

Figure 8: The stress amplification factor r as a function of the aspect ratio R_0/L of the ceramic tube for the composite drawn in figure 7 with PZT-5H ceramic tube and spurs epoxy

electrostrictive materials. For large area applications, these tubes can be readily integrated into 1-3 composite structure which provides low acoustic density and high piezoelectric activity. The effectiveness of the stress transfer between the polymer phase and the ceramic tube in 1-3 composite makes it possible to back fill the inside of the ceramic tube which increases the mechanical integrity of the tubular structure while keeps the piezoelectric response of the composite almost intact.

REFERENCES

1. R. E. Newnham and G. R. Ruschan, "Smart Electroceramics," J. Am. Ceram. Soc. 74, 463 (1991).
2. R. E. Newnham, Q. C. Xu, S. Kumar, and L. E. Cross, "Smart Ceramic," Ferro. 102, 259 (1990).
3. Q. M. Zhang, S. J. Jang, and L. E. Cross "High-frenquency strain response in ferroelectrics and its measurement using a modified Mach-Zehnder interferometer," J. Appl. Phys. 65, 2807 (1989).
4. See the data sheet of Morgon Matroc, Inc., Vernitron Div.
5. D. J. Taylor, D. Damjanovic, A. S. Bhalla, and L. E. Cross, "Large Hydrostratic Piezoelectric Coefficient in Lead Magnesium Niobate: Lead Titanate Ceramic," Annual Report of the Materialss Research
6. R. A. Langevin, "The Electro- Acoustic Sensitivity of Cylindrical Ceramic Tubes," J. Acoust. Soc. Am. 26, 421 (1954); "Handbook of Hydrophone Element Design Technoledgy", NUSC Technical Document 5813 (1978).
7. Q. M. Zhang, Wenwu Cao, H. Wang, and L. E. Cross, "Characterization of the performance of 1-3 type piezocomposites for low frenquency applications," J. Appl.- Phys. (Feb. 1993).
8. Wenwu Cao, Q. M. Zhang, and L. E. Cross, "Theoretical study on the static performance of piezoelectric ceramic-polymer composites with 1-3 connectivity," J. Appl. Phys. 72,5814 (1992).
9. The data used are: $Y=3.1$ (10^9 N/m^2), $\mu=1.148$ (10^9 N/m^2), and $\sigma=0.35$ for spurs epoxy (from C. G. Oakley, Ph. D. Thesis, The Pennsylvania State University, 1991); $s_{11}{}^c=1.64$ (10^{-11} m^2/N), and $\sigma=0.31$ (ref. 4).

Table I Hydrostatic properties of the end capped tube and 1-3 tubular composites

	ε	$d_h{}^{elf}$ (pC/N)	$d_b{}^{eff} g_b{}^{eff}(10^{-15}m^2/N)$	d_{31} (pC/N)	γ
End capped tube	2,945	-14,330	10,000	-235	1
Composite (air backing)	2,922	-5,502	6,389	-235	2.11
Composite (epoxy backing)	2,944	-4,970	5,172	-235	

APPENDIX   37

PIEZOELECTRIC TUBES AND TUBULAR COMPOSITES
FOR ACTUATOR AND SENSOR APPLICATIONS

Q. M. Zhang, H. Wang, and L. E. Cross

Materials Research Laboratory, The Pennsylvania State University

University Park, PA 16802

Abstract: The piezoelectric actuators and sensors made of tubular structure can provide a great agility of the effective response in the radial direction. For a radially poled piezoelectric tube, the effective piezoelectric constant in that direction can be tuned to be positive, zero, and negative by varying the ratio of the outer radius (R_0) to the inner radius (r_0) of the tube. For a suitable ratio of R_0/r_0, this effective constant can also be changed in sign or set to zero by adjusting the DC bias field level for tubes made of electrostrictive materials. Therefore, one can make a piezoelectric transducer with all the effective piezoelectric tensile constants having the same sign. The end capped thin wall tubes also exhibit exceptionally high hydrostatic response and the small size of the tubular structure makes it very suitable for integration into 1-3 composite which possesses low acoustic impedance and high hydrostatic response.

1

I. INTRODUCTION

The recent advance in the adaptive materials and structures has put increasing demands on new materials and material structures to broaden the range of material properties provided by the conventional materials. [1,2] The novel concept of piezocomposites is one such example which combines two or more materials with complementary properties to expand the effective properties of the composite beyond those of each individual component. [3,4] With the existing materials, by structure modifications, one can also greatly improve the performance of devices. In this paper, we will examine the effective piezoelectric properties of a tubular structure and its composites formed from arrays of such tube for both actuating and sensing applications. For a radially poled ceramic tube, the competition between the piezoelectric d_{33} effect and d_{31} effect in the radial direction provides a convenient way to adjust the effective piezoelectric properties in that direction by changes in the tube radii. The small thickness of a thin wall tube also makes it practical to use field biased electrostrictive materials for actuators and sensors since only a low terminal DC voltage is required to produce substantial piezoelectric activities in the materials in this geometry.

II. PIEZOELECTRIC RESPONSE OF A TUBE UNDER AN ELECTRIC FIELD

When a radially poled tube is subjected to an electric field along the radial direction, on the average, the strain in the axial direction equals $d_{31} E_m$, where d_{31} is the linear piezoelectric constant and E_m is the average field in the material. The response in the radial direction, however, is complicated. In this section, the solution of the elastic equation for the tubular structure under an electric field will be presented. It will be shown that with the same applied electric field, the outer diameter (OD) (or the inner diameter (ID)) of the tube can either expands or contracts depending on the ratio of the OD to ID of the tube. This

2

phenomenon is the direct consequence of the competition between the piezoelectric d_{33} and d_{31} effects, which have opposite sign in producing the change in the tube OD under electric field.

In analyzing the strain response of a tubular structure under an electric field, it is convenient to use the cylindrical polar coordinate system, as shown in figure 1. The symmetry of the problem requires that the ϕ-component of the displacement field $u_\phi = 0$. For a thin wall tube, one can neglect the coupling terms containing both r and z in the displacement field $\vec{u}$ and assume $\vec{u} = u_r(r)\, \hat{r} + u_z(z)\, \hat{z}$. Under this approximation, the non-zero strain component are: $u_{rr} = \dfrac{\partial u_r}{\partial r}$, $u_{\phi\phi} = \dfrac{u_r}{r}$, and $u_{zz} = \dfrac{\partial u_z}{\partial z}$. The constitutive relations for the tube, therefore, are

$$T_z = c_{11}\, u_{zz} + c_{12}\, u_{\phi\phi} + c_{12}\, u_{rr} - e_{31}E$$

$$T_r = c_{12}\, u_{rr} + c_{12}\, u_{\phi\phi} + c_{12}\, u_{zz} - e_{33}E \qquad (1)$$

$$T_\phi = c_{12}\, u_{zz} + c_{11}\, u_{\phi\phi} + c_{12}\, u_{rr} - e_{31}E$$

where T_z, T_r, and T_ϕ are the stress components in the three directions, the c_{ij} are the elastic stiffness constants, the e_{ij} are the piezoelectric stress constants, and E is the applied electric field within the tube wall in the r-direction. It is well known that the electric field is not a constant inside the tube wall and with a total voltage V applied to the tube, $E = \dfrac{V}{r \ln (R_0/r_0)}$ ($r_0 \le r \le R_0$). In equations (1), we made the approximation that the tube is isotropic elastically to simplify the analysis. The effect of anisotropy will be addressed in the next section in which we discuss the hydrostatic response of end capped tubes. Both experimental data, which will be presented later in this section, and the analysis in the next section show that the errors due to the isotropic approximation are not significant.

3

Making use of the constitutive equation (eq. (1)) and the static equilibrium condition, we can derive the basic elastic equations for this problem[5]

$$\frac{\partial}{\partial r}(\frac{1}{r}\frac{\partial}{\partial r}r u_r) = -\frac{e_{31}E}{r}\frac{s_{11}(1+\sigma)(1-2\sigma)}{1-\sigma} \qquad (2)$$

$$\frac{\partial u_z}{\partial z} = constant$$

where σ is the Poisson's ratio and s_{11} is the elastic compliance. The solutions to eq. (2) are

$$u_r = ar+\frac{b}{r} + \frac{e_{31}V}{ln\rho}\frac{s_{11}(1+\sigma)(1-2\sigma)}{1-\sigma} \qquad (3)$$

and $\qquad\qquad u_z = c\,z$

where $\rho=R_0/r_0$. a, b and c are the integration constants which can be determined from the boundary conditions: $u_{zz}=d_{31}E_m$, where E_m is the average radial electric field in the tube $(E_m=\frac{2V}{(R_0+r_0)\,ln(R_0/r_0)}$), and at $r=R_0$ and r_0, there is no external stress on the tube wall which implies $T_r=0$ at these two boundaries. Substituting eqs. (3) into eqs. (1) and using the boundary conditions, one can get

$$a= E_m ((1-2\,\sigma)\, d_{33}-\,\sigma\, d_{31})/(2(1-\,\sigma))$$

$$b= - R_0\, r_0\, E_m\, (d_{33} + \sigma\, d_{31})/(2(1-\,\sigma)) \qquad (4)$$

$$c= d_{31}\, E_m$$

The strain components for the tube can be obtained from eqs. (3) and (4). Here we are more interested in finding out how the tube outer diameter changes with applied electric field as the ratio of R_0/r_0 varies since in most of the applications, this is the quantity of interest. Substituting a and b from equation (4) into equation (3) for u_r and setting $r=R_0$ yield the displacement of the tube outer wall $u_r(R_0)$

$$u_r(R_0)=E_m ((R_0+r_0)\, d_{31} + (R_0- r_0)\, d_{33})/2$$

4

This equation reveals that $u_r(R_0)$ can be changed from positive to zero, and to negative by varying the ratio of R_0/r_0.

To illustrate the advantage of using thin wall tubes for actuator applications, one can compare the piezoelectric response of a tube with a rod of radius R_0, both of length L subjected to the same applied voltage V. For the rod, the field is applied along the axial direction and $u_{zz}=d_{33}$ V/L and $u_{rr}=d_{31}$ V/L. For the tube sample, one can equivalently introduce the quantity u_r/R_0 as the effective strain in the radial direction

$$u_r(R_0)/R_0 = E_m ((1+r_0/R_0) d_{31} + (1- r_0/R_0) d_{33})/2 \qquad (5)$$

Similar to a rod sample, we introduce the effective piezoelectric constants for the tube as if it were a rod poled axially,

$$u_{zz}=d_{33}^{eff} V/L \quad \text{and} \quad \frac{u_r}{R_0} = d_{31}^{eff} V/L \qquad (6)$$

where L is the axial length of the tube and V is the voltage applied on the tube wall. From $u_{zz}=d_{31} E_m$ and equation (5), the effective piezoelectric constants can be deduced

$$d_{33}^{eff} = d_{31} \frac{2L}{(R_0+r_0)\ln(R_0/r_0)} \qquad (7)$$

$$d_{31}^{eff} = \frac{L}{(R_0+r_0)\ln(R_0/r_0)}[(1+\frac{r_0}{R_0})d_{31}+(1-\frac{r_0}{R_0})d_{33}]$$

For thin walled tubes with L much larger than R_0, which is the case in most of the applications, both d_{33}^{eff} and d_{31}^{eff} can be exceptionally large. This demonstrates that the tubular structure has great advantage over the regular ceramic rod for actuator applications. Besides that, by choosing $(1+r_0/R_0) |d_{31}| > (1-r_0/R_0) |d_{33}|$, the effective d_{33} and d_{31} of the tube will have the same sign. By adjusting the ratio R_0/r_0, one can also continuously vary d_{31}^{eff} of the tube from positive to zero and to negative.

To compare with theory, the displacement field $u_r(R_0)$ and u_{zz} of a radially poled PZT-5 tube were measured using a double beam laser dilatometer.[6] The ceramic tubes used were manufactured by Morgon Matroc, Inc., Vernitron Div. with $R_0=0.635$ mm and

5

$r_0=0.381$ mm. From the data acquired and using eqs (3), (4) and (5), we got $d_{33}=289$ pC/N and $d_{31}=-141.3$ pC/N for the tube material. For most of commercially available PZT materials, the ratio of d_{33}/d_{31} ranges from 2.15 to 2.3.[7] The measured ratio here ($d_{33}/d_{31}=2.05$) is slightly below that range which we believe is the result of the approximations used in the derivation. The effective piezoelectric constants defined in eq. (6) for the tube, therefore, are $d_{33}^{eff}=-8180$ pC/N and $d_{31}^{eff}=-3220.5$ pC/N, the two coefficients have the same sign as predicted by eq. (7) and they are exceptionally large.

The small thickness of the tube wall also makes it possible to use electric field biased electrostrictive materials for the actuator application since only a small bias voltage is required here to induce substantial piezoelectric responses in the materials. In the field biased electrostrictive materials, it has been shown that the ratio of the piezoelectric constants d_{33}/d_{31} is bias field dependent.[8] Hence, for a suitable ratio of R_0/r_0, by tuning the DC bias field level, both sign and magnitude of d_{31}^{eff} of the tube can be varied.

III. THE HYDROSTATIC RESPONSE OF END CAPPED TUBES

The availability of small size ceramic tubes makes it attractive to integrate them into 1-: type piezoceramic-polymer composites for large area applications and to provide more flexibility for further material property modification. Before a detailed discussion of composite properties, we will derive the expression for the hydrostatic response of end capped tubes since they are commonly used as hydrostatic sensor.[9] As demonstrated in section II, the ratio of R_0/r_0 provides a convenient way to adjust the stress sensitivity of the sensor.

Similar to the derivations presented in the preceding section, the displacement field of a tube under hydrostatic pressure, when expressed in the cylindrical coordinate system, is $u_\phi=0$ and $\vec{u}=u_r(r)\,\hat{r} + u_z(z)\,\hat{z}$. (For an isotropic material, this is the exact form of the

6

displacement field equations. For a poled ceramic tube, the error in using this form of the displacement field, as will be shown later, is less than 10%.) Since the tube is capped on both ends, the pressure field is applied only to the outer surfaces of the tube, eq. (2) becomes:

$$\frac{\partial\, r\, u_r}{r \partial\, r} = const. \qquad and \qquad \frac{\partial\, u_z}{\partial\, z} = const. \qquad (8)$$

The solutions to the equations are:

$$u_r = a\, r + b/r \quad and \quad u_z = c\, z \qquad (9)$$

The non-zero strain components are:

$$u_{rr} = a - b/r^2, \quad u_{\phi\phi} = a + b/r^2, \quad and\ u_{zz} = c \qquad (10)$$

where a, b, and c are the integration constants which can be determined from the boundary conditions. The boundary conditions are: at $r=r_o$, $T_r = 0$; at $r=R_o$, $T_r = -p$; and at $z=0$ and $z=l$, the stress in the axial direction is $T_z = -p\, R_o^2/(R_o^2 - r_o^2)$, where $-p$ is the applied hydrostatic pressure. For the purpose of comparison, we will determine the integration constants a, b, and c in eq. (9) for both an elastically isotropic tube and a piezoelectric ceramic tube. For the later tube, the constitutive relations are:

$$T_z = c_{11}\, u_{zz} + c_{12}\, u_{\phi\phi} + c_{13}\, u_{rr}$$

$$T_r = c_{33}\, u_{rr} + c_{13}\, u_{\phi\phi} + c_{13}\, u_{zz} \qquad (11)$$

$$T_\phi = c_{12}\, u_{zz} + c_{11}\, u_{\phi\phi} + c_{13}\, u_{rr}$$

where c_{ij} are the elastic stiffness coefficients of the poled ceramics. Following the convention in the literature, in eq. (11), 3 reefers to the poling direction ($\hat{r}$ direction), 1 the $\hat{z}$ direction, and 2 the $\hat{\phi}$ direction. Substituting the strain components from eq. (10) into eq. (11) and omitting the term in T_z having r dependence, one can obtain a, b, c:

$$a = \frac{-p\, R_o^2}{R_o^2 - r_o^2} [\frac{c_{13} - c_{11}}{c_{13}(c_{12} + c_{13}) - c_{11}(c_{13} + c_{33})}] \qquad (12a)$$

7

$$b = \frac{- r_o^2 R_o^2}{R_o^2 - r_o^2} \frac{p}{c_{33} - c_{13}} \qquad (12b)$$

$$c = \frac{- p R_0^2}{R_o^2 - r_o^2} \left[\frac{c_{12} - c_{33}}{c_{13}(c_{12} + c_{13}) - c_{11}(c_{13} + c_{33})} \right] \qquad (12c)$$

Therefore, the stress distribution in the tube is given by:

$$T_r = \frac{- p R_o^2}{R_o^2 - r_o^2} [1 - \frac{r_o^2}{r^2}] \qquad (13a)$$

$$T_\phi = \frac{- p R_o^2}{R_o^2 - r_o^2} [\frac{c_{13}^2 + c_{12}^2 c_{11}^2 - c_{12} c_{33}}{c_{13}(c_{12} + c_{13}) - c_{11}(c_{13} + c_{33})} + \frac{c_{11} - c_{13}}{c_{33} - c_{13}} \frac{r_0^2}{r^2}] \qquad (13b)$$

$$T_z = \frac{- p R_o^2}{R_o^2 - r_o^2} \qquad (13c)$$

A term $((c_{12} - c_{13})b/r^2)$, which is less than 7% of the total T_z, was omitted from eq. (13c). Since T_z itself is one of the boundary condition used to derive the integration constants a, b, anc c and is equal to $- p R_o^2/(R_c^2 - r_n^2)$, the appearance of this extra-term in the expression for T_z derived using eqs. (11) and (12) is believed to be an error resulting from the approximation made for the displacement field for the tube under hydrostatic pressure. However, the small size of this error (less than 7%) indicates the approximation is ´ acceptable.

From the stress distribution equations, the hydrostatic response of the tube can be calculated from the relation

$$D_3 = d_{31} T_z + d_{31} T_\phi + d_{33} T_r \qquad (14)$$

where D_3 is the electric displacement in the poling direction. The value of d_h can be found by taking the average charge produced in the inner and outer surfaces of the tube wall and divided it by the outer surface area of the tube. From eq. (14):

$$d_h = \frac{1}{2} \{ d_{33} + \frac{R_o}{R_o - r_o} [1 + (\frac{c_{13}^2 + c_{12}^2 - c_{11}^2 - c_{12} c_{33}}{c_{13}(c_{13} + c_{12}) - c_{11}(c_{13} + c_{33})}) + \frac{c_{11} - c_{13}}{c_{33} - c_{13}} \frac{r_0}{R_0}] d_{31} \} \qquad (15)$$

In eq. (15), we have taken the tube outer surface as the total electroded area to calculate d_h. Using the elastic stiffness coefficients for PZT-5H,[7] for a tube with R_0=0.635 mm and r_0=0.381 mm, eq. (15) predicts d_h =-657 pC/N or 2.4 d_{31}. If the radius R_0 is doubled while keeping the wall thickness the same, d_h increases to -1786 pC/N. Hence, for thin walled tubes, an exceptionally large hydrostatic response can be achieved.

Eq. (13) can be reduced to the stress field of an elastically isotropic tube by using the isotropic conditions $c_{11}=c_{33}$, $c_{12}=c_{13}$. It can be shown that the result thus obtained is the exact solution to the tube stress field and similarly d_h can be found by simplifying eq. (15) using the isotropic condition:

$$d_h = \frac{1}{2} \{ d_{33} + \frac{R_o}{R_o - r_o} [2 + \frac{r_0}{R_0}] d_{31} \} \qquad (16)$$

Using the data above for the PZT-5H tube, the value of d_h calculated from eq. (16) is found to be -594 pC/N (2.17 d_{31}).

Experimental measurements were performed on several PZT-5 tubes (R_0=0.635 mm and r_0=0.381 mm) with two ends sealed and radially poled (the dielectric constant ϵ for this group of samples is around 1700 at the ambient pressure). d_h was determined by the direct piezoelectric effect, i.e. by measuring the charge induced on the electrodes of a sample which is subjected to a hydrostatic pressure. d_{31} and d_{33} were measured using a double beam laser interferometer.[6] For this group of samples, d_h ranged from -330 pC/N to -400 pC/N and d_{31} from -140 pC/N to -160 pC/N. The ratio between the experimental values of d_h and d_{31} (on average) is 2.45 which is very close to that predicted from eq. (15). Clearly, to make a quantitative prediction of the hydrostatic response of a tubular structure, one should include the elastic anisotropy in the calculation.

In analogy to the situation discussed in the preceding section, by varying the ratio of R_0/r_0, one can also manipulate the response of the tube to the stress field in the radial direction. Here, we will use the result just derived for the hydrostatic response of a tube as

9

an example. From eq. (14), the hydrostatic response of a tube comes from three terms, one is from the pressure in the axial direction and the other two from the pressure in the radial direction. The electric displacement $D_3{}^r$ due to the pressure in the radial direction is

$$D_3{}^r = d_{31} T_\phi + d_{33} T_r$$

Using the result of eq. (13) and taking the average charge produced at the tube inner wall and outer wall, one can obtain the piezoelectric response d^r of the tube to the pressure in the radial direction

$$d^r = \frac{1}{2} \{ d_{33} + \frac{R_o}{R_o - r_o} [(\frac{c_{13}^2 + c_{12}^2 - c_{11} - c_{12}c_{33}}{c_{13}(c_{13} + c_{12}) - c_{11}(c_{13} + c_{33})}) + \frac{c_{11} - c_{13}}{c_{33} - c_{13}} \frac{r_0}{R_0}] d_{31} \} \qquad (17)$$

Since d_{33} and d_{31} are opposite in sign, one can easily verify that by varying the ratio of R_0/r_0, d^r changes continuously from positive to zero, and to negative. Taking the elastically isotropic tube as an example and assuming $d_{33}/d_{31}=2.2$ in eq. (17), when $r_0/R_0=0.375$, d^r becomes zero. That is, the tube now becomes insensitive to the pressure wave in the radial direction. Similar to the actuator case, for suitable ratio of r_0/R_0, one can also change the sign of the effective radial response here by using electrostrictive materials with different DC bias field levels. This result as well as the result in the preceding section indicate that the range of the effective piezoelectric properties of the materials can be considerably broadened by using the tubular structures.

To calculate the hydrostatic figure of merit for this tubular sensor, we notice that in practice, the quantity $d_h g_h$ is a measure of the product of the charge and voltage produced in a unit volume material. For a tubular material, its effective volume is $\pi R_0^2 L$, where L is the tube length when the end capped tube is regarded as a rod with its radius equal to R_0. The capacitance of the tube is

$$C = \frac{2\pi L \varepsilon_0 \varepsilon}{\ln(R_0/r_0)}$$

10

where ε is the dielectric constant of the material. Since the total charge produced by the tube is equal to $2\pi R_0 L d_h$ and the voltage is equal to this charge divided by the capacitance of the tube, the effective figure of merit for the tube is

$$d_h g_h = \frac{1}{2\varepsilon\varepsilon_0} \ln(\frac{R_0}{r_0})(d_{33} + d_{31}(\frac{R_0}{R_0 - r_0})(2 + \frac{r_0}{R_0}))^2 \qquad (18)$$

Here, we have used d_h result for an isotropic tube (eq (17)). One can easily find the equivalent expression for a elastically anisotropic tubes. Clearly, a large figure of merit can be obtained for a thin walled tube.

IV. 1-3 TUBULAR COMPOSITES

A 1-3 composite consisting of piezoelectric ceramic tubes embeded in a polymer matrix is shown schematically in figure 2. For the composite discussed here, the tubes are radially poled and are electroded on the inner and outer cylindrical surfaces, the composite is electroded on the two end faces. Hence, special arrangements are required to ensure proper electric connections between the electrodes at the tube walls and the end faces of the composite. This kind of composite can be used for large area actuator and sensor applications, as well as smart materials in where both sensor and actuator are integrated into a single structure. In this section, we only discuss the properties of the composite associated with the sensor applications.

When tubes are integrated into a 1-3 type ceramic-polymer composite, as has been demonstrated in our earlier publications, there is a stress transfer between the polymer matrix and the ceramic tubes in the z-direction,[10,11] which is the result of the difference in the elastic constants between the two constituent phases and is through the shear force in the two phases. Due to this stress transfer, the piezoelectric response of the tube in the axial direction is enhanced. To provide a physical picture of how the hydrostatic response

11

of a tubular 1-3 composite changes as the elastic properties of the two constituent phases and their geometric parameters are varied, we will treat quantitatively the composite schematically drawn in figure 3. This composite corresponds to the tubular composite in the dilute limit. However, since only the polymer matrix close to the ceramic-polymer interface participates in the stress transfer, the result can also be applied to composites with finite ceramic content.

The procedure for calculating the stress transferred from the polymer phase to the ceramic rod is similar to that outlined the earlier publications.[10,11] Under hydrostatic pressure p, the surface displacement field u_z of the polymer phase in the z-direction should satisfy the following equation

$$\frac{2u_z}{L} = -(s_{11} + 2 s_{12}) p + \frac{s_{11}\mu L}{4}(\frac{\partial^2 u_z}{\partial r^2} + \frac{\partial u_z}{r \partial r}) \qquad (19)$$

where p is the hydrostatic pressure, s_{ij} is the elastic compliance of the polymer phase, μ is the shear modulus of the polymer phase, and L is the thickness of the composite in the z-direction. The solution to eq. (19) is the zeroth-order Hankel function $K_0(\rho)$ and

$$\frac{2u_z}{L} = -\frac{(1-2\sigma) p}{Y} + A K_0(r/\xi) \qquad (20)$$

where A is the integration constant and $\xi = L/(2 \sqrt{2Y/\mu})$, defines the strain decay length in the polymer phase. In eq. (20), we have made use of the relationships $s_{12} = -\sigma s_{11}$ and $Y = 1/s_{11}$, where Y and σ are the Young's modules and the Poisson's ratio of the polymer, respectively. The total force f transferred from the polymer phase to the ceramic tube is, therefore

$$f = Y \int_{R_o}^{-} 2\pi r A K_0(r/\xi) dr$$

Two boundary conditions are needed to determine f: the first is that at the ceramic tube-polymer interface, the z-component of the strain in the two phases should be equal, and the

12

second is the relationship between the z-component of the strain in the ceramic tube and the stress field

$$u_{zz} = -\frac{pR_0^2(1-\sigma^c)s_{11}^c}{R_0^2-r_0^2} + \frac{f\,s_{11}^c}{\pi\,(R_0^2-r_0^2)} \quad (21)$$

where s_{11}^c and σ^c are the elastic compliance and the Poisson's ratio of the ceramic tube, respectively. Eq. (21) can be derived following the procedure outlined in the preceding section. Hence, the amount of stress transferred from the polymer matrix to the ceramic tube is

$$\frac{f}{\pi A_0} = -\frac{pR_0^2}{A_0}\left(\frac{A_0(1-2\sigma)/(R_0^2 Y s_{11}^c) - (1-2\sigma^c)}{1+K_d(\rho_0)A_0/(2K_1(\rho_0)Y s_{11}^c R_0\xi)}\right) \quad (22)$$

where $A_0=(R_0^2-r_0^2)$, $\rho_0=R_0/\xi$, and $K_1(\rho)$ is the first order Hankel function. Since the polymer phase is subjected to a hydrostatic pressure, the Poisson's ratio effect causes the reduction of the effective pressure at the polymer faces from $-p$ to $-p(1-2\sigma)$. As shown in eq. (22), this reduces the stress transfer from the polymer phase to the ceramic tube. To increase the stress transfer, one should choose polymers with small Poisson's ratio. The total stress in the axial direction of the tube is

$$T_z = -\frac{pR_0^2}{A_0}\left(1+\frac{A_0(1-2\sigma)/(R_0^2 Y s_{11}^c) - (1-2\sigma^c)}{1+K_d(\rho_0)A_d/(2K_1(\rho_0)Y s_{11}^c R_0\xi)}\right)$$

$$= -\frac{pR_0^2}{A_0}\gamma \quad (23)$$

where γ is introduced as the stress amplification factor. In figure 4, we plot γ as a function of the aspect ratio R_0/L for a 1-3 tubular composite made of PZT-5H tube with $R_0=0.635$ mm and $r_0=0.381$ mm and spurs epoxy.[12] Apparently, for thin and long tubes, the stress amplification factor is large. This result is similar to that obtained earlier for 1-3 composites made from ceramic rods embedded in a polymer matrix.[10,11]

13

Using the results from section III and equation (23), one can write down the effective hydrostatic piezoelectric strain coefficient for 1-3 tubular composites

$$d_h^{ff}=\frac{L}{R_0}v_c(d_{33}+\frac{R_0}{R_0-r_0}(1+\gamma+\frac{r_0}{R_0})d_{31})$$ (24)

where v_c is the volume content of the ceramic tubes in the composite which is defined as $v_c=\pi R_0^2/a$, and a is the unit cell area of the composite. For a composite with low ceramic volume content, γ in eq. (22) is equal to that in eq. (24). With increased volume content, the dependence of γ on the material properties of the constituent phases will become more complicated and one may not be able to derive an analytical expression for γ except in some special cases. In this paper, we will not pursue this further and only point out that in the composite, there is always a stress transfer between the two phases ($\gamma > 1$). The general rule for increasing stress transfer is basically the same as that for the dilute composite case.

In the limit of $v_c \Rightarrow 1$, eq. (24) is reduced to that for a single tube when regarded as a rod with the similar dimensions

$$d_h^{ff}=\frac{L}{R_0}(d_{33}+\frac{R_0}{R_0-r_0}(2+\frac{r_0}{R_0})d_{31})$$ (25)

Eq. (16) can be converted to eq. (25) by using the area of the tube end (πR_0^2) as the effective electrode area instead of the area of the tube outer wall. Similarly, one can also derive the effective hydrostatic figure of merit for 1-3 tubular composites

$$d_h^{ff}g_h^{ff}=\frac{v_c}{2\varepsilon\varepsilon_0}\ln(\frac{R_0}{r_0})(d_{33}+\frac{R_0}{R_0-r_0}(1+\frac{r_0}{R_0}+\gamma))d_{31})^2$$ (26)

As $v_c \Rightarrow 1 (\gamma \Rightarrow 1)$, the result is reduced to that for a single tube sensor (eq. (18)).

For the comparison, in table I, we present the experimental values of the hydrostatic response of an end capped ceramic tube, a 1-3 composite with air filled capped ceramic tubes (air backing), and a 1-3 composite with epoxy backed ceramic tubes. The two 1-3 composites have ceramic tube volume content of 23.3 %. The dimensions of the tubes are: R_0=0.635 mm, r_0=0.381 mm, and L=9 mm. The polymer matrix was made of spurs

14

epoxy. For the data in the table, d_{31} was calculated using eq. (25) for a ratio $R_0/L=0.07$ where the ratio $d_{33}/d_{31}=2.2$ is used. From this d_{31}, γ was calculated from eq. (26). Clearly, the γ value here is much smaller than that shown in figure 4. One of the reasons is that figure 4 is for the composite in the dilute limit. The values of γ for composites with finite ceramic content should be smaller. The imperfect stress transfer between the two phases and the depoling effect of the tubes during the epoxy curing may also be responsible for this reduction of γ. Although the data in table I show that the hydrostatic responses of the composites tested are not as high as that of the single tube, the different is not very large. As the volume content of ceramic tubes and other parameters in a composite are varied, the effective hydrostatic figure of merit for 1-3 tubular composites will change. Under optimum conditions, one would expect that $d_h^{eff}g_h^{eff}$ for a tubular 1-3 composite will exceed that of a single tube. Further experimental and theoretical work is required to address this issue. It is significant that the figure of merit of 1-3 tubular composites is much higher than that of 1-3 composites using ceramic rods.[11]

If there were no stress transfer from the polymer phase to the ceramic tubes in these tubular composites, one would find for this 1-3 composite $d_h^{eff}= 3339$ pC/N and $d_h^{eff}g_h^{eff}= 2353 \times 10^{-15} m^2/N$, values much smaller than those listed in table I. That these values are much smaller clearly demonstrates the importance of the stress transfer between the two phases in a 1-3 composite.

One interesting feature from table I is that the hydrostatic response of the 1-3 tubular composite with ceramic tubes having epoxy backing does not differ significantly from that of the composite with tubes having air backing. That is, the presence of epoxy inside a tube does not change the stress distribution in the tube wall significantly except to transfer stress in the z direction. This can be understood because the elastic moduli of the ceramic tube are much higher than those of epoxy. As a result, the ceramic tube wall shields the epoxy

15

inside the tube from seeing the pressure in the radial direction. Conversely, the epoxy inside the tube does not exert significant amount of stress to the ceramic tube wall in the radial direction. Therefore, the epoxy filled inside of a tube provides an effective way of enhancing mechanical strength without reducing the hydrostatic response of the composite significantly.

V. SUMMARY AND ACKNOWLEDGEMENT

In this paper, the effective piezoelectric responses of the tubular structures and composites including them were evaluated both theoretically and experimentally. When used as actuators, the effective piezoelectric constant in the radial direction of a tube can be changed from positive to zero and to negative by adjusting the ratio of R_0/r_0 for piezoelectric materials or the DC bias field for electrostrictive materials. Therefore, the effective piezoelectric constants along the axial direction and the radial direction can both have the same sign. For the sensor applications, the two ends sealed tube exhibits exceptionally high hydrostatic response and analogues to the situation of actuators, the pressure response in the radial direction can be adjusted by the ratio R_0/r_0 for piezoelectric materials or the DC bias field for electrostrictive materials. For large area applications, these tubes can be readily integrated into 1-3 composite structures which provide low acoustic density and high piezoelectric activity. The effectiveness of the stress transfer between the polymer phase and the ceramic tube in 1-3 composite makes it possible to fill the inside of the ceramic tube with epoxy which increases the mechanical strength of the tubular structure without significantly reducing the piezoelectric response of the composite.

16

REFERENCES:

1. R. E. Newnham and G. R. Ruschan, J. Am. Ceram. Soc. **74**, 463 (1991).

2. R. E. Newnham, Q. C. Xu, S. Kumar, and L. E. Cross, Ferro. **102**, 259 (1990).

3. R. E. Newnham, D. P. Skinner, and L. E. Cross, Mat. Res. Bull. **13**, 525 (1978).

4. W. A. Smith, Proc. 1990 IEEE Ultrasonics Symposium, 145 (1990).

5. L. D. Landau and E. M. Lifshitz, "Theory of Elasticity" (Pergamon Press, 1986).

6. Q. M. Zhang, S. J. Jang, and L. E. Cross, J. Appl. Phys. **65**, 2807 (1989).

7. See the data sheet of Morgon Matroc, Inc., Vernitron Div.

8. D. J. Taylor, D. Damjanovic, A. S. F.alla, and L. E. Cross, Annual Report of the Materialss Research Laboratory, The Pennsylvania State University (1991).

9. R. A. Langevin, J. Acoust. Soc. Am. **26**, 421 (1954); "Handbook of Hydrophone Element Design Technoledgy", NUSC Technical Document 5813 (1978).

10. Q. M. Zhang, Wenwu Cao, H. Wang, and L. E. Cross, to be published in J. Appl. Phys. (Feb. 1993).

11. Wenwu Cao, Q. M. Zhang, and L. E. Cross, to be published in J. Appl. Phys. (Dec. 1992).

12. The data used are: $Y=3.1$ (10^9 N/m^2), $\mu=1.148$ (10^9 N/m^2), and $\sigma=0.35$ for spurs epoxy (from C. G. Oakley, Ph. D. Thesis, The Pennsylvania State University, 1991); $s_{11}^c=1.64$ (10^{-11} m^2/N), and $\sigma=0.31$ (ref. 7).

Table I Hydrostatic properties of the end capped tube and 1-3 tubular composites

	ε	d_h^{eff} (pC/N)	$d_h^{eff} g_h^{eff}(10^{-15} m^2/N)$	d_{31} (pC/N)	γ
End capped tube	2,945	-14,330	10,000	-235	1
Composite (air backing)	2,922	-5,502	6,389	-235	2.11
Composite (epoxy backing)	2,944	-4,970	5,172	-235	

18

Fig. 1

Ceramic Tubes

Polymer Matrix

Fig 2

Ceramic Tube

Polymer

z

L

O

r

Fig. 3

Fig. 4